Iowa Research Online
The University of Iowa's Institutional Repository

University of Iowa
Iowa Research Online

Theses and Dissertations

2011

Quark and lepton mass effects and the observational constraints on the high energy neutrino cross sections

Yu Seon Jeong
University of Iowa

Copyright 2011 Yu Seon Jeong

This dissertation is available at Iowa Research Online: http://ir.uiowa.edu/etd/1233

Recommended Citation
Jeong, Yu Seon. "Quark and lepton mass effects and the observational constraints on the high energy neutrino cross sections." PhD (Doctor of Philosophy) thesis, University of Iowa, 2011.
http://ir.uiowa.edu/etd/1233.

Follow this and additional works at: http://ir.uiowa.edu/etd

Part of the Physics Commons

QUARK AND LEPTON MASS EFFECTS AND THE OBSERVATIONAL CONSTRAINTS ON THE HIGH ENERGY NEUTRINO CROSS SECTIONS

by

Yu Seon Jeong

An Abstract

Of a thesis submitted in partial fulfillment of the
requirements for the Doctor of Philosophy
degree in Physics in the
Graduate College of The
University of Iowa

July 2011

Thesis Supervisor: Professor Mary Hall Reno

ABSTRACT

The cross sections of neutrino-nucleon scattering at high energies are evaluated with quark masses at next-to-leading order in strong interaction corrections. We compare the results with two kinds of schemes for treating the heavy quarks, the fixed flavor number scheme and the variable flavor number scheme for muon neutrino-nucleon interaction, and discuss which scheme is more relevant. The optimized parton distribution functions (PDF) for the flavor number schemes are also evaluated. The tau mass, much larger than the muon mass, suppresses the cross sections at low energies. We calculate the tau neutrino and antineutrino cross sections including the lepton mass corrections with low Q-extrapolated structure functions. Uncertainties due to the factorization scale, PDF choice, and the momentum transfer cutoff for the structure functions are also discussed with total theoretical errors. At ultra high energies (UHE), the same cross sections can be used for all flavors. We applied our evaluated cross sections to estimate the UHE neutrino event rates from lunar detection. The effective lunar aperture depends on the frequency and the minimum detectable electric field. We evaluate the effective aperture for a range of inputs. The event rates for both neutrino and cosmic rays are calculated in the standard model and compared with the enhanced neutrino-nucleon cross section for mini-black hole production. Lunar detection of UHE neutrino fluxes in the standard model will be challenging because low event rates are predicted.

Abstract Approved: _____
Thesis Supervisor

_____
Title and Department

_____
Date

QUARK AND LEPTON MASS EFFECTS AND THE OBSERVATIONAL CONSTRAINTS ON THE HIGH ENERGY NEUTRINO CROSS SECTIONS

by

Yu Seon Jeong

A thesis submitted in partial fulfillment of the
requirements for the Doctor of Philosophy
degree in Physics in the
Graduate College of The
University of Iowa

July 2011

Thesis Supervisor: Professor Mary Hall Reno

Graduate College
The University of Iowa
Iowa City, Iowa

CERTIFICATE OF APPROVAL

PH.D. THESIS

This is to certify that the Ph.D. thesis of

Yu Seon Jeong

has been approved by the Examining Committee for the thesis requirement for the Doctor of Philosophy degree in Physics at the July 2011 graduation.

Thesis Committee: _____
Mary Hall Reno, Thesis Supervisor

_____
Vincent Rodgers

_____
Kenneth Gayley

_____
Wayne Polyzou

_____
Palle Jorgensen

ACKNOWLEDGMENTS

There are many people to whom I would like to express my gratitude. Foremost, I am deeply indebted to my advisor Professor Mary Hall Reno, whose guidance and support over the years have enabled me to complete this work. I am also grateful to Professor Kenneth Gayley for his extremely helpful discussion and tutoring on neutrino observation. In addition, I would like to express my sincere gratitude to my former advisor Professor Sun Kun Oh who gave me the opportunity to study high energy physics. Many thanks also go to my colleagues and friends, even though I do not list them by name here, for helping me to solve the problems in both academic and daily life and for their mental and emotional support. Finally, my special thanks go to my family, who have encouraged and fully supported me.

ABSTRACT

The cross sections of neutrino-nucleon scattering at high energies are evaluated with quark masses at next-to-leading order in strong interaction corrections. We compare the results with two kinds of schemes for treating the heavy quarks, the fixed flavor number scheme and the variable flavor number scheme for muon neutrino-nucleon interaction, and discuss which scheme is more relevant. The optimized parton distribution functions (PDF) for the flavor number schemes are also evaluated. The tau mass, much larger than the muon mass, suppresses the cross sections at low energies. We calculate the tau neutrino and antineutrino cross sections including the lepton mass corrections with low Q-extrapolated structure functions. Uncertainties due to the factorization scale, PDF choice, and the momentum transfer cutoff for the structure functions are also discussed with total theoretical errors. At ultra high energies (UHE), the same cross sections can be used for all flavors. We applied our evaluated cross sections to estimate the UHE neutrino event rates from lunar detection. The effective lunar aperture depends on the frequency and the minimum detectable electric field. We evaluate the effective aperture for a range of inputs. The event rates for both neutrino and cosmic rays are calculated in the standard model and compared with the enhanced neutrino-nucleon cross section for mini-black hole production. Lunar detection of UHE neutrino fluxes in the standard model will be challenging because low event rates are predicted.

TABLE OF CONTENTS

LIST OF TABLES v

LIST OF FIGURES vi

CHAPTER

1 INTRODUCTION 1

2 FORMALISM 6

2.1 Differential Cross Section 6
2.2 Neutrino-Neucleon Charged Current Interaction 10
2.2.1 Quark Mass Correction at Leading Order 10
2.2.2 Next-to-leading Order Corrections 12
2.2.3 Small x Extrapolation 16
2.3 Tau Neutrino and Antineutrino Interaction with Nucleons 20
2.3.1 Target Mass Correction in the Structure Functions 20
2.3.2 Low Q^2 Extrapolations of the Structure Functions 22

3 QUARK MASS EFFECTS IN MUON NEUTRINO-NUCLEON SCATTERING 25

4 TAU NEUTRINO AND ANTINEUTRINO CROSS SECTIONS . . . 33

5 APPLICATION: RADIO CHERENKOV SIGNALS FROM THE MOON 41

5.1 Cosmogenic Neutrinos 41
5.2 Neutrino Cross Sections and Effective Angle 44
5.3 The Cherenkov Signals from Neutrinos 51
5.4 The Cherenkov Signals from Cosmic Rays 58
5.5 Radio Cherenkov Signals with Enhanced Neutrino Cross Sections 63

6 CONCLUSION 70

REFERENCES 74

A EFFECTIVE INTERACTION LENGTH 74

B EFFECTIVE PROBABILITY FOR COSMIC RAYS AND DOWNWARD NEUTRINOS 76

BIBLIOGRAPHY 79

LIST OF TABLES

2.1 The splitting functions for the quark to quark and the gluon to quark processes in the massless limit. 13

2.2 The λ values for the sea quarks and the gluon in the small x extrapolation equations. 19

2.3 The coefficients A^i_j of F_i^{TMC} 21

2.4 The coefficients B^i_j of F_i^{TMC} 22

2.5 The coefficients C_j of F_i^{TMC} 22

2.6 The parameters for R-function 23

2.7 The parameter values for CKMT parameterization 24

4.1 The ν_τ and $\bar{\nu}_\tau N$ charged current cross section 34

4.2 The ν_τ and $\bar{\nu}_\tau$ -proton charged current cross section 35

4.3 The estimated errors for ν_τN scattering 39

4.4 The estimated errors for $\bar{\nu}_\tau$N scattering 39

LIST OF FIGURES

2.1 The neutrino-nucleon scattering process. 7

2.2 The quark initiated process at (a) leading order and (b) next-to-leading order 12

2.3 The gluon initiated process at next-to-leading order. Gluon splitting produces a quark-antiquark pair. 13

2.4 The gluon distribution of the CTEQ6.6M PDF set for$x$ with $Q = M_W$. . 17

2.5 The λ values of the sea quarks and the gluon as a function of Q. These values are for the CTEQ6.6M PDF set. 18

3.1 The charged current cross section for $\nu_\mu N$ scattering as a function of the incident neutrino energy. The massless $\overline{\text{MS}}$ scheme is used with the CTEQ6.6M PDFs. 25

3.2 The ratio of the flavor contributions to the neutrino-nucleon charged current cross section. The cross section is evaluated using the VFNS with the CTEQ6.6M PDF. 26

3.3 The ratio of the NLO charged current σ_{VFNS} to σ_{FFNS} for CTEQ6.6M and GJR PDFs. 28

3.4 Comparison of GJR and CTEQ6.6M PDFs for the NLO charged current σ_{VFNS} and σ_{FFNS}. 28

3.5 K_{NLO}-factor, the ratio of the σ_{NLO} to σ_{LO} for the VFNS and FFNS. The LO cross section is evaluated using the same PDFs as the NLO cross section and the scaling variable χ is used. 29

3.6 K_{NLO}-factor: the ratio of the neutrino-nucleon charged current σ_{NLO} to σ_{LO} for $E_\nu = 10^2 - 10^{12}$ GeV. The LO cross section is evaluated using the same PDFs as the NLO cross section. The VFNS cross section is evaluated using the ACOT(χ) or S-ACOT(χ) scheme for $E_\nu \leq 10^9$ GeV. 31

3.7 K_{NLO}-factor: the ratio of the neutrino-nucleon charged current σ_{NLO} to σ_{LO} for $E_\nu = 10^2 - 10^{12}$ GeV. The CTEQ6.6M PDFs are used. The "mixed scheme" ratio uses 3 flavors of quark PDFs but makes a subtraction for 5 flavors from the gluon fusion term. 32

4.1 The tau neutrino- (upper curves) and antineutrino- (lower curves) isoscalar nucleon charged current cross section, for $W > 1.4$ GeV (blue, solid) and $W > M$ (red, dashed). Target mass corrections, NLO QCD and low Q extrapolations of the structure functions below $Q_c^2 = 2$ GeV^2 are included in the evaluation. 33

4.2 The ratio of $\sigma_{CC}(\nu_\tau N)/\sigma_{CC}(\nu_\mu N)$ neutrino- (solid) and antineutrino- (dashed) DIS cross sections. 36

4.3 The differential cross section $d\sigma/dy/E$ for DIS charged current scattering with an isoscalar nucleon target for (a) 10 GeV and (b) 50 GeV incident energies. 37

4.4 An estimate of the theoretical errors for ν_τ (triangles) and $\bar{\nu}_\tau$ (squares) deep-inelastic charged current cross sections. 40

5.1 The flux of cosmic rays (red, dashed) shown in Ref. [53] and the flux of cosmogenic neutrinos (blue) in Ref. [52]. The neutrino fluxes are estimated with the maximum proton energy in sources of $E_{p,max} = 10^{11}$ GeV (Low, dot-dashed), $10^{11.5}$ GeV (Middle, dotted) and $10^{12.5}$ GeV (High, solid). . 42

5.2 The neutrino interaction length (in centimeters water equivalent distance) as a function of energy. The diameters of the Earth and the Moon are also indicated. 45

5.3 upward neutrino and downward neutrino 46

5.4 Upward neutrino passing through a sphere. 48

5.5 The effective solid angle divided by 2π as a function of the ratio of the diameter to the attenuation distance ($2R/\lambda$). The dashed line shows the quantity of $\lambda/2R$. The diameter is in water equivalent distance. 49

5.6 The detector with incident neutrinos. The detector has the area of $\mathcal{A}$ and the depth of d. Neutrinos are incident to the surface with an angle of θ_ν from the normal. 50

5.7 The effective aperture for neutrinos as a function of incident neutrino energy for $\varepsilon_{min} = 10^{-8}$ V/m/MHz. The solid lines represent the total of the downward smooth (ds, dashed), the downward rough (dr, dotted) and the upward(u, dot-dashed) contributions. (a) is for $\nu = 150$ MHz and (b) is for $\nu = 1.5$ GHz. 54

5.8 The effective aperture for neutrinos as a function of incident neutrino energy for $\varepsilon_{min} = 10^{-11}$ V/m/MHz. The solid lines represent the total of the downward smooth (ds, dashed), the downward rough (dr, dotted) and the upward(u, dot-dashed) contributions. (a) is for $\nu = 150$ MHz and (b) is for $\nu = 1.5$ GHz. 55

5.9 The event number of neutrinos as function of scaling factor s for neutrino-nucleon cross section. These are evaluated for $\nu = 1.5$ GHz and $\varepsilon_{min} = 10^{-8}$ V/m/MHz the high cosmogenic neutrino flux from Fig. 5.1. The event number of each piece is indicated with total event number as in previous figures. 56

5.10 The event number of neutrinos as function of scaling factor s as Fig 5.9. These are for $\nu = 1.5$ GHz and $\varepsilon_{min} = 10^{-11}$ V/m/MHz with the high cosmogenic neutrino flux (red) and the low cosmogenic neutrino flux (blue) from Fig. 5.1. 57

5.11 The number of events as a function of radio frequency with the high flux of neutrinos for $\varepsilon_{min} = 10^{-11} - 10^{-8}$ V/m/MHz. 58

5.12 The effective aperture for cosmic rays as a function of cosmic ray energy for $\varepsilon_{min} = 10^{-8}$ V/m/MHz. The solid lines represent the total of the downward smooth (ds, dashed) and the downward rough (dr, dotted). (a) is for $\nu = 150$ MHz and (b) is for $\nu = 1.5$ GHz. 61

5.13 The effective aperture for cosmic rays as a function of cosmic ray energy for $\varepsilon_{min} = 10^{-11}$ V/m/MHz. The solid lines represent the total of the downward smooth (ds, dashed) and the downward rough (dr, dotted). (a) is for $\nu = 150$ MHz and (b) is for $\nu = 1.5$ GHz. 62

5.14 The number of events as a function of radio frequency with the high neutrino flux (red, solid) and with cosmic rays (blue, dashed) for $\varepsilon_{min} = 10^{-11} - 10^{-8}$ V/m/MHz. 63

5.15 The neutrino interaction length (in centimeters water equivalent distance) as a function of energy with the non-standard model neutrino-nucleon cross section for mini-black hole production for $n = 7$ and $M_D = 1$ TeV. The cross sections for black hole are taken from Connolly, Thorne, and Waters [87] (dashed) and Feng [88] (dotted), respectively. The interaction length with the standard model cross section is indicated with the solid line. 65

5.16 The probability as a function of the ratio of the photon interaction length to the neutrino interaction length. It is evaluated numerically for a minimum detectable field of $\varepsilon_{min} = 10^{-8}$ V/m/MHz and $\varepsilon_{min} = 10^{-11}$ V/m/MHz, and for the frequency of $\nu = 150$ MHz and $\nu = 1.5$ GHz. Numerical result is shown as the solid lines and analytical ones are indicated with the dashed lines for neutrinos and cosmic rays. 66

5.17 The event number as a function of radio frequency for $\varepsilon_{min} = 10^{-11}$ and $\varepsilon_{min} = 10^{-8}$ V/m/MHz. The results with the neutrino cross section for black hole production are shown as the red (Connolly [87]) and blue (Feng [88]) lines, while the one with the standard model cross section is shown as black line. Green line indicates the event number from cosmic ray flux. 67

5.18 The event number as a minimum detectable field ε_{min} for $\nu = 150$ MHz (dashed) and $\nu = 1.5$ GHz (solid). The color of each line indicates the same as Fig. 5.17. 68

B.1 The passage of the downward particle and the induced signal in the lunar regolith. 76

CHAPTER 1
INTRODUCTION

Neutrinos are elementary particles which are unique in some of their properties. Neutrinos are electrically neutral, so they are not affected by magnetic fields while they propagate. Neutrinos are weakly interacting particles and able to travel long distances, so they reach the Earth from distant astrophysical sources. In addition, they pass through regions of opaque matter which are not penetrated by photons. Due to these properties, neutrinos are useful probes of astrophysical sources [1].

Neutrinos are generally from the meson and muon decay. Protons create the mesons through the interactions with nucleons and photons,

$$PX \rightarrow \text{mesons} + \text{other particles} \ , \tag{1.1}$$

where X is the nucleon N and photon γ. In accelerators, X is the nucleon target. The meson from this interaction decays producing neutrinos, e.g., $\pi^- \rightarrow \mu^- \bar{\nu}_\mu$, and subsequently the muon decays creating the neutrinos, $\mu^- \rightarrow e^- + \bar{\nu_e} + \nu_\mu$. Also, neutrinos can be from the decays of neutrons, $n \rightarrow p + e^- + \bar{\nu}_e$.

One special feature of neutrinos is their oscillations [2, 3, 4, 5]. Oscillations have been observed through, e.g., muon neutrino disappearance [2]. Tau neutrino events are important appearance signals to verify the oscillation of muon neutrinos to tau neutrinos [6, 7]. Cosmic and atmospheric neutrinos are mainly from the subsequent decays of the pions and kaons produced by the interaction of protons with nucleons and photons. The flavor ratio of neutrinos following pion and muon decay is $\nu_e : \nu_\mu : \nu_\tau = 1 : 2 : 0$. However, the substantial fraction of muon neutrinos oscillate to tau neutrinos while they propagate through the Earth and over astronomical distances. Over large distances, the ratio is expected to be changed to $\nu_e : \nu_\mu : \nu_\tau = 1 : 1 : 1$ at the detection point [1].

The neutrino energy generated by the current accelerators is below 10^3 GeV [5]. Neutrinos produced in the atmosphere by cosmic rays have been measured at the highest energy of 400 TeV [8]. Astrophysical sources produce the highest energy neutrinos [1]. These ultra high energy neutrinos will carry the information from outer space. But, up to now, there is no observation of these astrophysical neutrinos.

The current experiments [9, 10, 11, 12, 13, 14, 15, 16, 17] rely on the theoretical neutrino-nucleon cross sections to interpret their data. The theoretical neutrino cross sections at ultra high energies have been developed in Ref. [18, 19, 20, 21, 22].

In this thesis, we discuss the results for the high energy neutrino nucleon cross section up to 10^{12} GeV [23], and the tau neutrino cross sections for $10 - 10^4$ GeV [24]. We calculate the deep inelastic scattering (DIS) charged current cross sections for the muon (anti-)neutrino, and the tau (anti-)neutrino scattering with isoscalar nucleons. The cross sections are evaluated at next-to-leading order in quantum chromodynamic (QCD) corrections with two different parameterizations of the nucleon structure in the parton distribution functions (PDF) [25, 26].

The formalism used in our evaluations of the cross sections is presented in Chapter 2. I indicate the general expression of the differential cross section for the charged current neutrino-nucleon interactions in terms of the structure functions, and the kinematic factors, with attention to the quark mass corrections. The flavor number schemes for including heavy quark masses in the structure functions are discussed. I describe our extrapolation of parton distribution functions for the momentum fraction x below the range provided by the PDF sets. For the tau neutrino scattering case, I review the target mass correction in the structure functions for the energies between 10 GeV and 10 TeV. Lastly, the parameterizations for the low Q^2 extrapolations of the structure functions are described.

The first topic we studied is quark mass effects in muon neutrino-nucleon scattering at high energies, $10^2 - 10^{12}$ GeV [23]. The heavy quark mass effects in the structure

functions and the parton distribution functions at next-to-leading order (NLO) have been investigated in Ref. [27, 28, 29, 30, 31, 32, 33, 34, 35, 36, 37, 38, 39, 40]. New in the work presented here is the use of two different flavor number schemes to investigate the heavy quark mass effects at ultra high energies. One of the flavor number schemes is the fixed flavor number scheme (FFNS) with the three light flavors, and the other is the variable flavor number scheme (VFNS) with the five flavors at high energies, where the charm and bottom quarks are effectively "light". We also evaluated the cross section using the modified minimal subtraction scheme ($\overline{\text{MS}}$) [41] with massless quarks to compare with the result of VFNS with general masses. The massless $\overline{\text{MS}}$ scheme at next-to-leading order for ultra high energy neutrinos also appears in Ref. [21]. As the incident neutrino energy increases, the momentum transfer Q also increases. Through this wide energy range, first the charm quark mass, and then the bottom quark mass m_Q become small compared to the momentum transfer. We investigate the numerical results according to the flavor schemes when $\log(Q^2/m_Q^2)$ becomes large. The results and the analysis of this investigation are summarized in Chapter 3.

In Chapter 4, the results of the second topic, the tau neutrino and anti-neutrino charged current cross section from 10 GeV to 10 TeV, are discussed. The tau neutrino cross sections have been studied in Ref. [42, 43]. We have updated the cross sections for new experiments, so they can use the best theoretical values [24]. New in this work is a presentation of the theoretical errors on the cross sections. Here, we include the charm quark only to look at the heavy quark effects, and the tau mass corrections, which are significant at low energies. The bottom quark corrections are small in these energies. We also include low-Q^2 extrapolations of the structure functions. The target mass correction to the structure functions were considered, which are important in the very low energies of this energy range. Finally, we calculated the theoretical errors for the cross sections due to the low-Q^2 extrapolation for the structure functions, the

scale dependence, the PDF errors, and the flavor number schemes.

As stated above, the tau neutrinos and anti-neutrinos are produced by the oscillation of muon neutrinos. The tau neutrinos are also produced at high energies in the pp interactions via the D_s meson decays even though it is greatly suppressed relative to the muon and the electron neutrinos [44, 45]. These tau neutrinos are expected to be measured by the DeepCore, sub-detector of IceCube. The ICARUS T600 detector [46] of CERN Neutrinos to Gran Sasso (CNGS) project [47] also aims to detect the tau neutrinos signals from the ν_μ beam.

Chapter 5 shows an application of the ultra high energy (UHE) neutrino cross section to the search for radio Cherenkov signals from the Moon. We present potential constraints on the cross section of ultra high energy neutrinos using the Moon as a target [17, 48]. The signal is the radio Cherenkov emission from neutrino interactions near the lunar surface. Non-detection of the neutrinos can limit either the neutrino flux or the neutrino cross sections. Most common researches are on the limit of the neutrino flux. Here, the new limit on the neutrino cross sections is investigated. Other discussions about the cross section constraints, in Ref [49, 50, 51], do not consider the case of lunar detection. We show that considering standard models of neutrino fluxes with the standard model cross sections do not give the observable radio Cherenkov signals from the Moon.

In this Chapter 5, I discuss potential sources of UHE neutrinos and their fluxes [52] along with the cosmic ray flux [53]. I also present the approximate formula from Ref. [48] and modification of this analytic formula to imply attenuation by the strong interaction as well. Using thees fluxes and the formula, we evaluate the event rates of neutrinos and cosmic rays, and their dependence on the frequency and the minimum detectable electric field, respectively. Finally, we calculate and compare the event rates of neutrinos and cosmic rays with the enhanced neutrino-nucleon cross section in the extension of the standard model. I indicate the results of these evaluations.

A summary of the conclusions of the thesis appears in Chapter 6, as well as a direction of future work.

CHAPTER 2
FORMALISM

2.1 Differential Cross Section

Charged current neutrino nucleon scattering proceeds via

$$\nu_l + N \rightarrow l + X \ , \tag{2.1}$$

for nuclear target N and final state hadrons X. Here, l represents lepton flavor, and $l = e$, μ, and τ for electron, muon, and tau, respectively. The total cross section of this interaction has contributions from quasi-elastic scattering, pion production, and deep inelastic scattering. Quasi-elastic scattering dominates at low incident neutrino energies ($E_\nu \sim 1$ GeV). Specifically, quasi-elastic muon neutrino scattering occurs with $\nu_\mu n \rightarrow \mu p$. In this energy range, pion production begins to contribute. An example of this process is $\nu_\mu n \rightarrow \mu^- p \pi^0$. Eventually, multiple hadrons are produced, so X consists of more than one or two hadrons. This is called deep inelastic scattering (DIS).

The lowest energy we examine in this thesis is 10 GeV. Above this energy, the DIS cross section dominates. Especially from the energy of 100 GeV, the total charged current cross section is almost the same as the DIS cross section [54]. Thus, we study the charged-current DIS process of neutrino scattering with isoscalar nucleons,

$$\nu_l(k) + N(p) \rightarrow l(k') + X \ , \tag{2.2}$$

where $N = (n + p)/2$. The quantities, k, p, and k', are the momenta of the incident neutrino, the nucleon target, and the outgoing lepton, respectively. Fig. 2.1 shows this process graphically. In the figure, W represents invariant mass of final hadronic state.

The differential cross section for neutrino-nucleon scattering, in terms of the

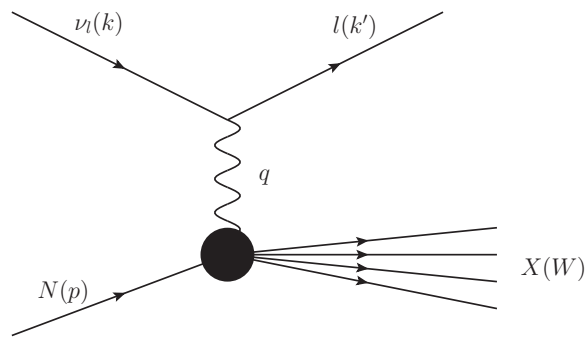

Figure 2.1: The neutrino-nucleon scattering process.

structure functions, is

$$\begin{aligned}\frac{d^2\sigma}{dx\ dy} &= \frac{G_F^2 M_N E_\nu}{\pi}\left(\frac{M_W^2}{Q^2+M_W^2}\right)^2\left[(xy^2+\frac{m_l^2 y}{2E_\nu M_N})F_1+(1-y-\frac{M_N xy}{2E_\nu}-\frac{m_l^2}{4E_\nu^2})F_2\right.\\ &\pm \left.\left(xy(1-\frac{y}{2})-\frac{m_l^2 y}{4E_\nu M_N}\right)F_3+\frac{m_l^2(m_l^2+Q^2)}{4E_\nu^2 M_N^2 x}F_4-\frac{m_l^2}{E_\nu M_N}F_5\right], \qquad (2.3)\end{aligned}$$

with the Fermi coupling constant $G_F = 1.16 \times 10^{-5}$ GeV^{-2}. Here, M_W is the mass of the W boson, M_N is the mass of the nucleon, and m_l of the outgoing lepton. The + sign of the F_3 term is for the neutrino scattering case, and the − sign is for the anti-neutrino scattering. The invariant quantities for this process are defined as below;

$$\begin{aligned}Q^2 &= -q^2 = -(k-k')^2\ ,\\ x &= Q^2/2p\cdot q = Q^2/2M_N\nu\ ,\\ y &= p\cdot q/p\cdot k = \nu/E\ ,\\ W^2 &= (p+q)^2 = M_N^2+2M_N\nu-Q^2\ ,\\ \nu &= q\cdot P/M_N = E-E'\ ,\\ k'^2 &= m_l^2\ , \quad \text{and} \quad p^2 = M_N^2\ . \qquad (2.4)\end{aligned}$$

The quantity x is the momentum fraction of the nucleon carried by struck quark and y is the fraction of lepton's energy lost in the nucleon rest frame. Here, ν is the energy loss of the lepton, where E and E' are the initial and final lepton energies.

The quantities W^2, k'^2, and p^2 are the mass squared of the system X, the outgoing lepton, and the target nucleon, respectively. The most general hadronic tensor with the proper Lorentz structure $W^{\mu\nu}$ is [34, 42],

$$\begin{aligned} W^{\mu\nu} &= -g^{\mu\nu}W_1 + \frac{1}{M^2}p^\mu p^\nu W_2 - i\epsilon^{\mu\nu\alpha\beta}\frac{1}{2M^2}p_\alpha q_\beta W_3 \\ &\quad + \frac{1}{M^2}q^\mu q^\nu W_4 + \frac{1}{2M^2}(p^\mu q^\nu + p^\nu q^\mu)W_5 + \frac{1}{2M^2}(p^\mu q^\nu - p^\nu q^\mu)W_6 \ . \end{aligned} \tag{2.5}$$

The structure functions, $F_1 - F_5$, are extracted from the relations,

$$\begin{aligned} F_1 &= W_1 \ , \\ F_i &= \frac{\nu}{M}W_i \ , \quad i = 2, 3, 4, 5 \ . \end{aligned} \tag{2.6}$$

The differential cross section is proportional to the product of the leptonic and hadronic tensors,

$$d\sigma \sim L_{\mu\nu}W^{\mu\nu} \ , \tag{2.7}$$

where the leptonic tensor $L_{\mu\nu}$ is [5]

$$L_{\mu\nu} = 2(k_\mu k'_\nu + k'_\mu k_\nu - g_{\mu\nu}k \cdot k' + i\epsilon_{\mu\nu\alpha\beta}k^\alpha k'^\beta) \ . \tag{2.8}$$

The terms with W_6 disappear by the algebra, so there is no F_6 in the differential cross section.

In the massless quark and massless target limit in the parton model, the leading order structure functions can be expressed in terms of the quark distribution functions. For example, including just up and down quarks,

$$\begin{aligned} F_1(x,\mu) &\cong (d(x,\mu) + \overline{u}(x,\mu)) \ , \\ F_2(x,\mu) &\cong 2x(d(x,\mu) + \overline{u}(x,\mu)) \ , \\ F_3(x,\mu) &\cong 2(d(x,\mu) - \overline{u}(x,\mu)) \ . \end{aligned} \tag{2.9}$$

Perturbative quantum chromodynamic (QCD) corrections modify the equations in 2.9. For example, the gluon distribution function $G(x,\mu)$ appears at next-to-leading order (NLO) in QCD. The functions F_1 and F_2 are related by $2xF_1 = F_2$, known as

Callan-Gross relation. In addition, $F_4 = 0$ and $F_5 = F_2/2x$ according to the Albright and Jarlskog relations [42]. These relations are modified by NLO QCD and non-zero quark mass corrections [43].

In the differential cross section, the kinematics limit of x and y are respectively [42],

$$\frac{m_l^2}{2M_N(E_\nu - m_l)} \;\leq\; x \;\leq\; 1 \;, \tag{2.10}$$

$$a \;-\; b \;\leq\; y \;\leq\; a \;+\; b \;, \tag{2.11}$$

where a and b are

$$a \;=\; \left[1 - m_l^2\left(\frac{1}{2M_N E_\nu x} + \frac{1}{2E_\nu^2}\right)\right]/(2 + M_N x/E_\nu) \;, \tag{2.12}$$

$$b \;=\; \left[\left(1 - \frac{m_l^2}{2M_N E_\nu x}\right)^2 - \frac{m_l^2}{E_\nu^2}\right]^{1/2}/(2 + M_N x/E_\nu) \;. \tag{2.13}$$

Another kinematic factor in the evaluation of the cross section is the hadronic final state invariant mass, W, where

$$W^2 = Q^2\left(\frac{1}{x} - 1\right) + M^2 \;. \tag{2.14}$$

For quasi-elastic scattering, the structure functions are proportional to the delta function $\delta(W^2 - M^2)$. For some energies, the contributions from the quasi-elastic scattering, and few pion production processes co-exist with the DIS contributions (see e.g. [54]). To avoid double counting these exclusive contributions, the DIS evaluation is conducted in the region, $W^2 \geq W_{min}^2$. We set $W_{min} = 1.4$ GeV.

The minimum W^2 comes into the differential cross section through y. We convert equation 2.3 to the expression of $d\sigma/dydQ^2$. By integrating it over Q^2, the differential distribution in y is obtained as below,

$$\frac{d\sigma}{dy} = \int_{Q^2_{\rm min}}^{Q^2_{\rm max}} dQ^2 \, \frac{d\sigma}{dy\, dQ^2} \;, \tag{2.15}$$

where

$$\frac{d\sigma}{dydQ^2} = \frac{1}{2MEy}\frac{d\sigma}{dxdy} \ . \tag{2.16}$$

The integration limits are

$$\begin{aligned} Q^2_{\rm min} &= 2E^2(1-\epsilon)(1-y) - m_\tau^2 \ , \\ Q^2_{\rm max} &= 2MEy + M^2 - W^2_{\rm min} = 2MEy - \delta^2 \ . \end{aligned} \tag{2.17}$$

Here, ϵ and δ are defined as

$$\epsilon = \sqrt{1 - m_\tau^2/\Big((1-y)E\Big)^2} \ , \tag{2.18}$$

$$\delta^2 = W^2_{min} - M^2 \ . \tag{2.19}$$

Also, y has the range between

$$\begin{aligned} y_{\rm min} &= \frac{1}{4ME}\left(2ME + \delta^2 - m_\tau^2 - \sqrt{(2ME-\delta^2)^2 + m_\tau^4 - 2(2ME+\delta^2)m_\tau^2}\right) \ , \\ y_{\rm max} &= 1 - m_\tau/E \ , \end{aligned} \tag{2.20}$$

when $W_{min} \neq M$.

2.2 Neutrino-Neucleon Charged Current Interaction

2.2.1 Quark Mass Correction at Leading Order

In this section, our focus is on the muon neutrino interaction. For the muon neutrino scattering case, the terms dependent on the lepton mass are not shown in the differential cross section because the muon mass is small enough to suppress these terms. Therefore, the differential cross section is reduced to

$$\begin{aligned} \frac{d\sigma}{dx\,dy} &= \frac{G_F^2 M_N E_\nu}{\pi}\left(\frac{M_W^2}{Q^2+M_W^2}\right)^2 \\ &\times \left[xy^2F_1 + (1 - y - \frac{M_N xy}{2E_\nu})F_2 \pm xy(1-\frac{y}{2})F_3\right] \ . \end{aligned} \tag{2.21}$$

The kinematic limits of x and y are also approximated by

$$0 \leq \ x \ \leq \ 1 \ , \text{ and } \ 0 \leq \ y \ \leq \ 1 \ . \tag{2.22}$$

The quark mass corrections appear in two factors; the light-cone momentum fraction in the parton distribution functions, and the pre-factors of the combined quark distribution functions to make structure functions. Firstly, the light-cone momentum fraction is x in the massless limit. But, considering the quark masses, x is changed to [34]

$$\xi \ = \ \eta \frac{Q^2 - m_1^2 + m_2^2 + \Delta(-Q^2, m_1^2, m_2^2)}{2Q^2} \ , \tag{2.23}$$

where the Nachtmann variable η is [60]

$$\eta \ = \ \frac{2x}{1 + \sqrt{1 + 4x^2(M_N)^2/Q^2}} \ , \tag{2.24}$$

and

$$\Delta(a, b, c) \ = \ \sqrt{a^2 + b^2 + c^2 - 2(ab + bc + ac)} \ , \tag{2.25}$$

where m_1 and m_2 are the initial and the final quark masses. The Nachtmann variable accounts for the target nucleon mass correction.

The other correction is shown in the structure functions. The expressions for the quark mass corrected structure functions are [34]

$$\begin{aligned} F_1 &= \sum_{ij} V_{ij}^2 \left(\frac{Q^2 + m_i^2 + m_j^2}{\Delta} \right) \Big(q_i(\xi, \mu) + \bar{q}_j(\xi, \mu) \Big) \\ F_2 &= \sum_{ij} 2x V_{ij}^2 \frac{\Delta}{Q^2} \Big(q_i(\xi, \mu) + \bar{q}_j(\xi, \mu) \Big) \\ F_3 &= \sum_{ij} 2V_{ij}^2 \Big(q_i(\xi, \mu) - \bar{q}_j(\xi, \mu) \Big) \ , \end{aligned} \tag{2.26}$$

where $\Delta \equiv \Delta(-Q^2, m_i^2, m_j^2)$. V_{ij}^2 is the squared element of the Cabibbo-Kobayashi-Maskawa (CKM) mixing matrix [5]. For quark initiated process, i is the index of the initial quark and j is of the final quark ($i \leftrightarrow j$ for anti-quark). Here, the quark constituents in the summation are different according to the flavor number schemes.

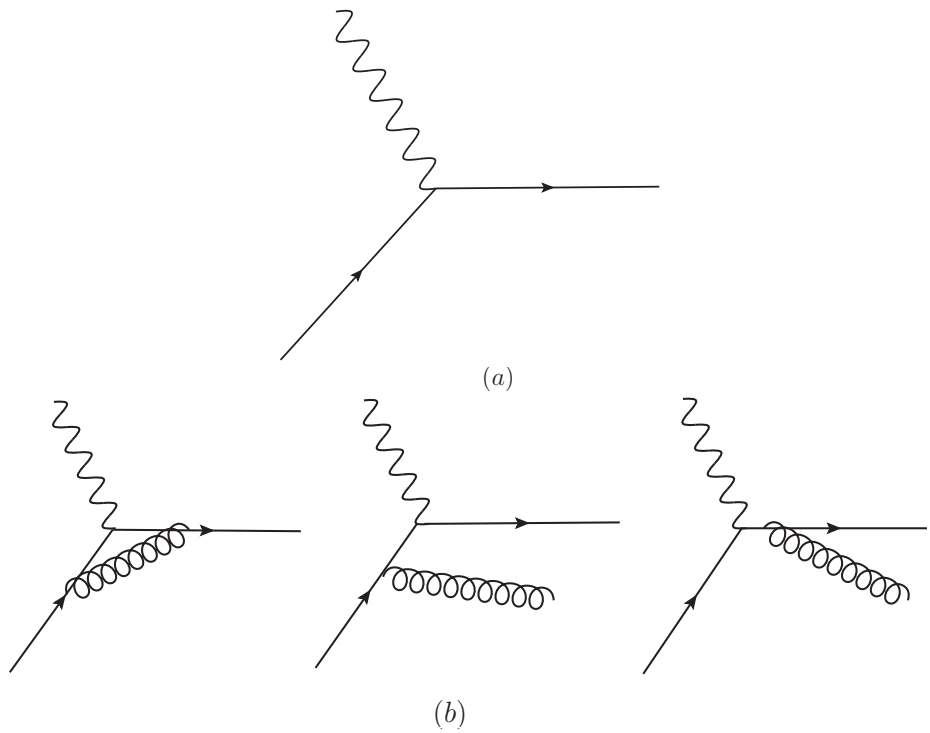

Figure 2.2: The quark initiated process at (a) leading order and (b) next-to-leading order

In the fixed flavor number scheme, $i = d,\ s,\ j = \bar{u}$, while $i = d,\ s,\ b,\ j = \bar{u},\ \bar{c}$ in the variable flavor number scheme. The factorization scale μ is set to Q.

2.2.2 Next-to-leading Order Corrections

The next-to-leading order (NLO) structure functions have contributions from the quark and the anti-quark initiated process and the gluon splitting process [35, 32]. The quark and the anti-quark initiated process includes the gluon emissions and the loop corrections. The diagrams for these processes are shown in fig. 2.2 and in fig. 2.3.

The factorization theorem [55] takes the structure functions as,

$$F_\lambda = \sum_a f^a \otimes \hat{\omega}_{a,\lambda} = \sum_a \int_{\xi_{min}}^1 \frac{d\xi}{\xi} f^a(\xi,\mu)\hat{\omega}_{a,\lambda}\left(\frac{\eta}{\xi}, \frac{Q}{\mu}, \frac{m_i}{\mu}, \alpha_s(\mu)\right) , \tag{2.27}$$

where f^a are the parton distribution functions, and $\hat{\omega}_{a,\lambda}$ are the hard scattering

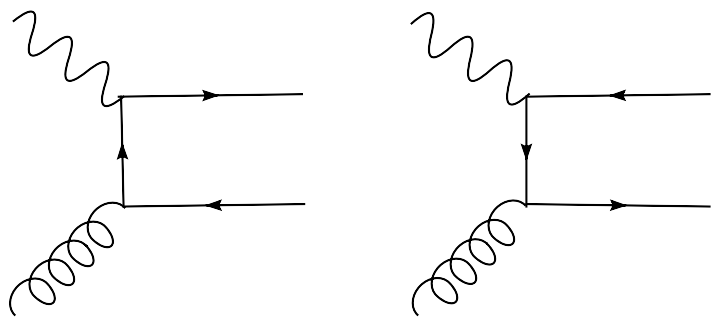

Figure 2.3: The gluon initiated process at next-to-leading order. Gluon splitting produces a quark-antiquark pair.

$P_{q\to q}$	$P_{g\to q}$
$\frac{4}{3}\left(\frac{1+\xi^2}{(1-\xi)_+}+\frac{3}{2}\delta(1-\xi)\right)$	$\frac{1}{2}(\xi^2+(1-\xi)^2)$

Table 2.1: The splitting functions for the quark to quark and the gluon to quark processes in the massless limit.

amplitudes. The hard scattering amplitudes at NLO have the form,

$$\hat{\omega}_{q(\bar{q}),\lambda} = \omega^{(0)}_{q(\bar{q}),\lambda} + \omega^{(1)}_{q(\bar{q}),\lambda} - \frac{\alpha_s}{2\pi} P_{q\to q} \ln \frac{\mu^2}{m^2_{q(\bar{q})}} \omega^{(0)}_{q(\bar{q}),\lambda} \quad \text{for } f^a = q, \bar{q} \ , \tag{2.28}$$

$$\hat{\omega}_{g,\lambda} = \omega^{(1)}_{g,\lambda} - \frac{\alpha_s}{2\pi} P_{g\to q} \ln \frac{\mu^2}{m^2_q} \omega^{(0)}_{q,\lambda} - \frac{\alpha_s}{2\pi} P_{g\to \bar{q}} \ln \frac{\mu^2}{m_{\bar{q}^2}} \omega^{(0)}_{\bar{q},\lambda} \quad \text{for } f^a = g \ . \tag{2.29}$$

The detailed expressions of $\omega^{(0)}_q$, $\omega^{(1)}_q$, and $\omega^{(1)}_g$ are indicated in Ref. [34, 35, 32]

The general splitting functions $P_{q\to q}$, $P_{g\to q,\ \bar{q}}$ appear in the evolution equation for parton distributions, known as the 'DGLAP equations' [56]. The necessary splitting functions in this section are $P_{q\to q}$ for the quark to quark and $P_{g\to q}$ for the gluon to quark. These specific expressions are shown in Table 2.1.

The structure functions F_λ are affected by the produced partons as well as the initiated partons in the nucleons, so $\hat{\omega}_{a,\lambda}$ involves the summation over the quarks and

gluons of the final state, and it can be written as [57],

$$\hat{\omega}_a = \sum_b \hat{\omega}_{ab} \ , \tag{2.30}$$

where a represents the initial state parton flavors in the nucleons, and b indicates the produced flavors in the final state. Thus, b includes all flavors that can be shown in the final state, whereas the constituents of a are the only partons that initiate the interactions, so it depends on the flavor number scheme. In this section, we compare the variable flavor number scheme (VFNS) and the fixed flavor number scheme (FFNS) to investigate the effect of the heavy quark masses.

In the fixed flavor number scheme, only the light quarks, u, d, s and their anti-quarks are considered as the active particles in the nucleon. The heavy quarks participate in the interactions only through the gluon splitting process. On the other hand, in the variable flavor number scheme, the heavy quark is a constituent of the nucleon for interactions at high energies. In the energy range investigated here, in addition to the three light flavors, c and b quarks including their anti-quarks participate in the quark splitting interactions. The top quark is too massive to be considered as a constituent of the nucleon for neutrino interactions.

We take an approach provided by Aivazis, Collins, Olness, and Tung, [34, 35], so called the ACOT scheme, for the VFNS with general quark masses. In the ACOT scheme, the quark masses regulate the collinear divergences. We take the structure function for the For example of the ACOT structure function F_1 is,

$$\begin{aligned} F_1^{\rm ACOT} &= \sum_{ij} q_i \otimes \omega_{ij}^{(0)} + \bar{q}_j \otimes \omega_{\bar{i}\bar{j}}^{(0)} \\ &+ q_i \otimes (\omega_{ij}^{(1)} - \omega_{ij}^{(0)} \frac{\alpha_s}{2\pi} P_{i\to i} \ln \frac{\mu^2}{m_i^2}) + \bar{q}_j \otimes (\omega_{\bar{j}\bar{i}}^{(1)} - \omega_{\bar{j}\bar{i}}^{(0)} \frac{\alpha_s}{2\pi} P_{\bar{j}\to\bar{j}} \ln \frac{\mu^2}{m_j^2}) \\ &+ g \otimes \left(\omega_{g\to i\bar{j}}^{(1)} - \omega_{ij}^{(0)} \frac{\alpha_s}{2\pi} P_{g\to i} \ln \frac{\mu^2}{m_i^2} - \omega_{\bar{j}\bar{i}}^{(0)} \frac{\alpha_s}{2\pi} P_{g\to\bar{j}} \ln \frac{\mu^2}{m_j^2} \right) \ , \end{aligned} \tag{2.31}$$

where i, $j = u$, d, s, c, b, and their anti-quarks. The splitting functions are

$$P_{i\to i} = P_{\bar{j}\to\bar{j}} = P_{q\to q} \ \text{ and } \ P_{g\to i} = P_{g\to\bar{j}} = P_{g\to q} \ , \tag{2.32}$$

and $P_{q\to q}$ and $P_{g\to g}$ are shown in Table 2.1.

For the massless modified minimal subtraction scheme, ($\overline{\mathrm{MS}}$), dimensional regularization is used to regulate the collinear singularities. In $\overline{\mathrm{MS}}$, the factor of $1/\epsilon$ appears instead of the logs of the subtractions terms,

$$\begin{aligned} F_1^{\overline{\mathrm{MS}}} &= \sum_{ij} q_i \otimes \omega_{ij}^{(0)} + \bar{q}_j \otimes \omega_{\bar{i}\bar{j}}^{(0)} \\ &+ q_i \otimes (\omega_{ij}^{(1)} - \omega_{ij}^{(0)} \frac{\alpha_s}{2\pi} P_{i\to i} \frac{1}{\epsilon}) + \bar{q}_j \otimes (\omega_{\bar{j}\bar{i}}^{(1)} - \omega_{\bar{j}\bar{i}}^{(0)} \frac{\alpha_s}{2\pi} P_{\bar{j}\to\bar{j}} \frac{1}{\epsilon}) \\ &+ G \otimes \left(\omega_{g\to i\bar{j}}^{(1)} - \omega_{ij}^{(0)} \frac{\alpha_s}{2\pi} P_{G\to i} \frac{1}{\epsilon} - \omega_{\bar{j}\bar{i}}^{(0)} \frac{\alpha_s}{2\pi} P_{G\to\bar{j}} \frac{1}{\epsilon}\right) . \end{aligned} \tag{2.33}$$

We take the specific process $s \to c$ to show the difference of the structure functions between the FFNS and the VFNS. The respective structure functions for this process are as below;

$$\begin{aligned} F_1^{\mathrm{VFNS}}(s\bar{c}) &= q_s \otimes \omega_{sc}^{(0)} + q_s \otimes (\omega_{sc}^{(1)} - \omega_{sc}^{(0)} \frac{\alpha_s}{2\pi} P_{q\to q} \ln \frac{\mu^2}{m_s^2}) \\ &+ \bar{q}_c \otimes \omega_{\bar{s}\bar{c}}^{(0)} + \bar{q}_c \otimes (\omega_{\bar{c}\bar{s}}^{(1)} - \omega_{\bar{c}\bar{s}}^{(0)} \frac{\alpha_s}{2\pi} P_{\bar{q}\to\bar{q}} \ln \frac{\mu^2}{m_c^2}) , \end{aligned} \tag{2.34}$$

$$F_1^{\mathrm{FFNS}}(s\bar{c}) = q_s \otimes \omega_{sc}^{(0)} + q_s \otimes (\omega_{sc}^{(1)} - \omega_{sc}^{(0)} \frac{\alpha_s}{2\pi} P_{q\to q} \ln \frac{\mu^2}{m_s^2}) . \tag{2.35}$$

Besides ACOT scheme, there are some other possible choices to treat the heavy quark masses [37, 38, 39, 40].

We use the ACOT(χ) and S-ACOT(χ) prescriptions. The S-ACOT scheme [58] is the simplified ACOT prescription. In the S-ACOT scheme, the quark masses are set to zero for LO and NLO quark initiated terms as well as the subtraction terms. But, for the gluon initiated process, the quark masses are retained. The S-ACOT prescription makes the calculations simpler, and this simplicity is expected to have more impact at higher orders. For the incident neutrino energies above $E_\nu \geq 10^6$ GeV, the S-ACOT(χ) scheme is used to avoid numerical errors. For ACOT(χ) and S-ACOT(χ) schemes [36, 58], the lower limit of the convolution integral ξ_{min} depends

on the kind of the flavor. The limits are

$$\begin{aligned} \xi_{min} &= \xi \quad \text{for } f = q_i,\ \bar{q}_j \\ \xi_{min} &= \chi \equiv \eta\left(1 + \frac{(m_i + m_j)^2}{Q^2}\right) \quad \text{for } f = G \end{aligned} \tag{2.36}$$

where ξ is the quark mass corrected light-cone momentum fraction and η is the Nachtmann variable as defined above.

2.2.3 Small x Extrapolation

In evaluating the cross sections, the CTEQ6.6M [25] and Glück, Jimenez-Delgado and Reya (GJR) [26] parton distribution functions are used. These PDF sets are generated for $x_{\min} < x < 1$ and a range of Q^2. The minimum value of x, $x_{\min}$, for the CTEQ6.6M PDF set is 10^{-8}, and for the GJR PDF set, $x_{\min} = 10^{-9}$. We consider the energies up to $E \sim 10^{12}$ GeV. As E increases, Q^2 increases since Q^2 is proportional to E, $Q^2 = (2ME_\nu)xy$. Depending on rising Q^2, the values of parton distribution functions $\bar{q}(x, Q)$ and $g(x, Q)$ also increase. The cross section, however, decreases due to the factor of $\left(\frac{M_W^2}{Q^2+M_W^2}\right)^2$. The propagator suppression dominates the contribution of the increased PDFs, and Q^2 is limited by $Q^2 \sim M_W^2$. Then, at the ultra high energies, x could be less than $x_{\min}$ of each PDF by the relation $x \sim M_W^2/(2ME_\nu)$ with $y = 1$. Thus, PDFs should be extrapolated for the values below $x_{\min}$.

We use a power law to extrapolate the PDF below $x_{\min}$ [19]. For example, for the gluon PDF ,

$$xg(x, Q) = A_g(Q)x^{-\lambda_g(Q)} \ . \tag{2.37}$$

In Fig. 2.4, we show the gluon distribution function for x with $Q = M_W$. The solid line is from the CTEQ6.6M PDF, and the dotted line is from our extrapolation below $x_{\min}$.

With the two points, $(x_0, x_0 g(x_0, Q))$ and $(x_1, x_1 g(x_1, Q))$, we determine $A_g(Q)$,

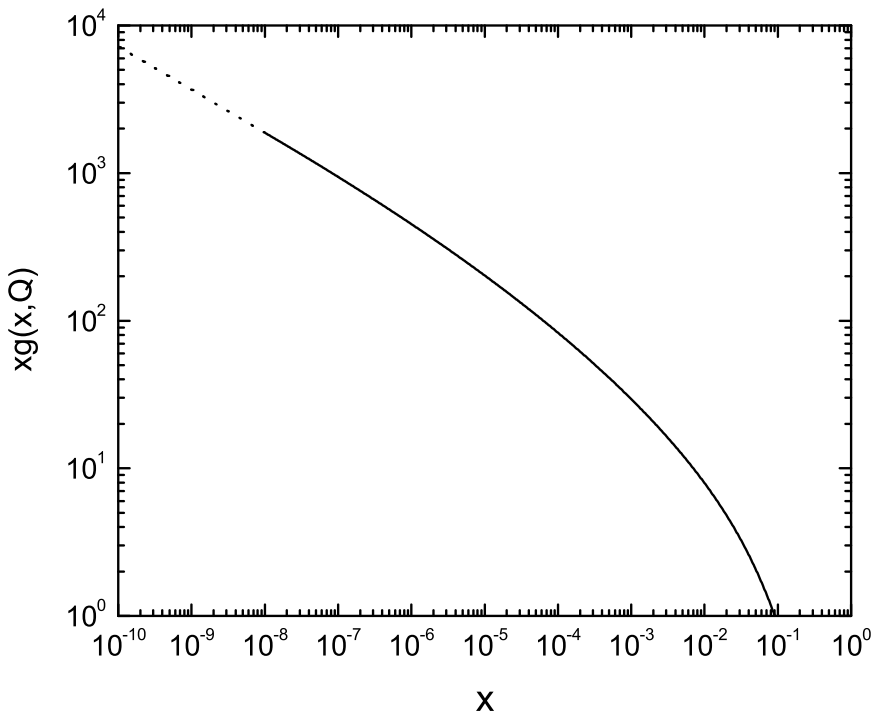

Figure 2.4: The gluon distribution of the CTEQ6.6M PDF set for$x$ with $Q = M_W$.

and $x^{-\lambda_g(Q)}$,

$$A_g(Q) = x_0 g(x_0, Q)/x_0^{-\lambda_g(Q)} \ ,$$

$$\lambda_g(x, Q) = \log\left(\frac{x_1 g(x_1, Q)}{x_0 g(x_0, Q)}\right)/\log\left(\frac{x_1}{x_0}\right) \ . \tag{2.38}$$

For actual evaluation, we choose $x_0 = x_{\min}$, and $x_1 = 2x_{\min}$. For Q, we use the fixed value, $Q = M_W$, for the GJR PDF sets, while we use the range of $50 \leq Q \leq 150$ for the CTEQ6.6M PDFS. So, the λ values for the CTEQ6.6M PDFs are dependent with Q.

The $\lambda_i(Q)$ is obtained as,

$$\lambda_i(Q) \ = \ m_i \log Q + C \ . \tag{2.39}$$

The slope and the coefficient are determined by the equations,

$$m_i = \frac{\lambda_i(x,Q_2) - \lambda_i(x,Q_1)}{\log Q_2 - \log Q_1} ,$$

and

$$\begin{aligned} C &= \lambda_i(x,Q_1) - m_i \log Q_1 \\ &= \lambda_i(x,Q_1) - \frac{\lambda_i(x,Q_2) - \lambda_g(x,Q_1)}{\log Q_2 - \log Q_1} \log Q_1 . \end{aligned} \tag{2.40}$$

The subscript i means the kind of the parton. We show the $\lambda_i(Q)$ values for the CTEQ6.6M PDFs in Fig. 2.5. The $\lambda_i(Q)$ is reduced as Q decreases, but the decrease in $\lambda_i(Q)$ is slight for the change of Q. The slope of gluon $\lambda_g(Q)$ is larger than the quark slopes $\lambda_q(Q)$ for whole range of Q.

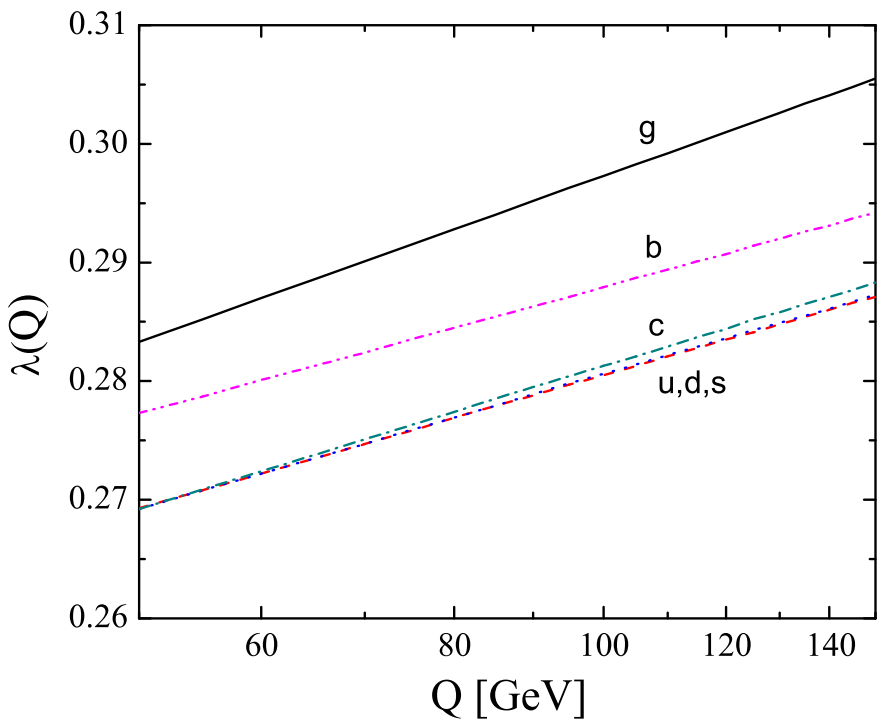

Figure 2.5: The λ values of the sea quarks and the gluon as a function of Q. These values are for the CTEQ6.6M PDF set.

The extrapolated parton distribution functions below $x_{\min}$ can be expressed as

$$xg(x,Q) = x_{\min} g(x_{\min},Q)(x/x_{\min})^{-\lambda_g(Q)} \ ,$$

$$x\overline{q}(x,Q) = x_{\min} \overline{q}(x_{\min},Q)(x/x_{\min})^{-\lambda_{\overline{q}}(Q)} \ .$$

At small x, the contributions of the valence quarks are not important, and the anti-quark distribution equals the sea quark distribution.

Our λ values for each component are shown in Table 2.2. The numbers in this table are for $Q = M_W$. This is important for the ultra high energy cross sections. We note that for $Q \sim M_W$, the parton distribution functions are determined only to x values of $10^{-3} \sim 10^{-2}$ by the HERA and Tevatron Jet experiments [5].

	CTEQ6.6M	GJRV	GJRF
$\lambda_{\overline{u}}$	0.276	0.255	0.260
$\lambda_{\overline{d}}$	0.276	0.255	0.260
$\lambda_{\overline{s}}$	0.276	0.255	0.260
$\lambda_{\overline{c}}$	0.277	0.257	-
$\lambda_{\overline{b}}$	0.284	0.264	-
λ_g	0.292	0.267	0.273
$x_{\min}$	10^{-8}	10^{-9}	10^{-9}

Table 2.2: The λ values for the sea quarks and the gluon in the small x extrapolation equations. These values are for $Q = M_W$. In the fixed flavor number scheme (here for GJRF), there are no charm and bottom quark PDFs.

2.3 Tau Neutrino and Antineutrino Interaction with Nucleons

In this section, we discuss additional corrections for relatively low energy neutrino interactions to study the tau neutrino and anti-neutrino interaction with the nucleons.

$$\nu/\bar{\nu}_\tau(k) \quad + \quad N(p) \rightarrow \tau/\bar{\tau}(k') \ + \ X \ . \tag{2.41}$$

For some of the energies we consider here, tau mass corrections are significant, so we keep the terms related with the lepton mass in the differential cross section, eq. 2.3. In the energy range we consider, 10 GeV to 10 TeV incident neutrino energy, the target mass is also important, so the target mass correction is also considered in the structure functions.

2.3.1 Target Mass Correction in the Structure Functions

The first nucleon target mass correction appears in the Nachtmann variable as shown in eq.(1.10). The nucleon mass also affects the structure functions. We indicates the target mass corrected structure functions as F_i^{TMC}, while the uncorrected structure functions as F_i. By the operator product expansion approach provided by Georgi and Politzer [61], the target mass corrected structure functions, F_i^{TMC}, are obtained as below [62];

$$F_i^{TMC} \ = \ \sum_{i=1,5} A_j^i F_i^{(0)}(\eta, Q) + B_j^i h_i(\eta, Q) + C_j g_2(\eta, Q) \ , \tag{2.42}$$

where

$$F_i^{(0)} \equiv (\lim_{M\rightarrow 0} F_i^{TMC}(x, Q))|_{x=\eta} \ . \tag{2.43}$$

The functions, $h_1(\eta, Q)$ - $h_5(\eta, Q)$, and $g_2(\eta, Q)$ are

$$\begin{aligned}
h_1(\eta, Q) &= \int_\eta^1 du \frac{2F_1^{(0)}(u, Q)}{u^2} \\
h_2(\eta, Q) &= \int_\eta^1 du \frac{F_2^{(0)}(u, Q)}{u^2} \\
h_3(\eta, Q) &= \int_\eta^1 du \frac{F_3^{(0)}(u, Q)}{u} \\
h_4(\eta, Q) &= \int_\eta^1 du \frac{4F_4^{(0)}(u, Q)}{u} \\
h_5(\eta, Q) &= \int_\eta^1 du \frac{2F_5^{(0)}(u, Q)}{u} \\
g_2(\eta, Q) &= \int_\eta^1 du \quad h_2(u, Q) \\
&= \int_\eta^1 du (u - \eta) \frac{F_2^{(0)}(u, Q)}{u^2} \ . \qquad (2.44)
\end{aligned}$$

The coefficient, A_j^i, B_j^i, and C_j, are indicated in Table 2.3 - 2.5 in terms of the x, ρ, η, and μ. Here, $\rho = \sqrt{1 + 4x^2M^2/Q^2}$, and $\mu = M^2/Q^2$.

A_j^i	$i = 1$	$i = 2$	$i = 3$	$i = 4$	$i = 5$
$j = 1$	$\frac{x}{\eta\rho}$	0	0	0	0
$j = 2$	0	$\frac{x^2}{\eta^2\rho^3}$	0	0	0
$j = 3$	0	0	$\frac{x}{\eta\rho^2}$	0	0
$j = 4$	0	$\frac{\mu^2x^3}{\rho^3}$	0	$\frac{1}{1+\mu\eta^2}$	$-\frac{2\mu\chi^2}{\rho^2}$
$j = 5$	0	$-\frac{\mu x^2}{\eta\rho^3}$	0	0	$\frac{x}{\eta\rho^2}$

Table 2.3: The coefficients A_j^i from Ref. [62]

The difference between F_i^{TMC} and F_i is greater as x is larger, so F_i^{TMC} has more important effects on the cross sections at the low energies. Reviews of the target mass

B^i_j	$i=1$	$i=2$	$i=3$	$i=4$	$i=5$
$j=1$	0	$\frac{\mu x^2}{\rho^2}$	0	0	0
$j=2$	0	$\frac{6\mu x^3}{\rho^4}$	0	0	0
$j=3$	0	0	$\frac{2\mu x^2}{\rho^3}$	0	0
$j=4$	0	$\frac{-2\mu^2 x^4}{\rho^4}(2-\mu\eta^2)$	0	0	$\frac{\mu\chi^2}{\rho^3}$
$j=5$	0	$\frac{2\mu x^2(1-\mu\eta x)}{\rho^4}$	0	0	$\frac{\mu x^2}{\rho^3}$

Table 2.4: The coefficients B^i_j from Ref. [62]

C_1	C_2	C_3	C_4	C_5
$\frac{2\mu^2 x^3}{\rho^3}$	$\frac{12\mu^2\chi^4}{\rho^5}$	0	$\frac{2\mu^2 x^3}{\rho^5}(1-2\mu x^2)$	$\frac{6\mu^2 x^3}{\rho^5}$

Table 2.5: The coefficients C_j from Ref. [62]

corrections to the structure functions are summarized in Refs. [61, 62].

2.3.2 Low Q^2 Extrapolations of the Structure Functions

As stated above, each PDF set has the range 1.3 GeV $< Q <$ 10^5 GeV for CTEQ6.6, and 0.5(0.3) GeV^2 $\leq Q^2 \leq$ 10^8 GeV^2 for GJR NLO(LO). Due to eq. 2.10 and eq. 2.14, Q^2 can be lower than the minimum Q^2 for the PDFs, although W^2 is greater than W^2_{min}. In order to extrapolate the structure functions to low Q^2, we use the parameterization formulated by Capella, Kaidalov, Merino, and Tran Thanh Van (CKMT) [63], and extended to neutrino scattering in Ref. [64]. We take the forms of the CKMT structure functions in ref.[64], which adjust the electromagnetic

parameterization to neutrino scattering,

$$
\begin{aligned}
F_1^{\mathrm{CKMT}}(x,Q^2) &= \frac{F_2}{2x}(1+\frac{4M^2x^2}{Q^2})/(1-R)\ , \\
F_2^{\mathrm{CKMT}}(x,Q^2) &= Ax^{-\Omega(Q^2)}(1-x)^{n(Q^2)+4}\left(\frac{Q^2}{Q^2+a}\right)^{1+\Omega(Q^2)} \\
&+ Bx^{1-\alpha_R}(1-x)^{n(Q^2)}\left(\frac{Q^2}{Q^2+b}\right)^{\alpha_R}(1+f(1-x))\ , \qquad (2.45) \\
F_3^{\mathrm{CKMT}}(x,Q^2) &= \left[\frac{A}{15}x^{-\Omega(Q^2)}(1-x)^{n(Q^2)+4}\left(\frac{Q^2}{Q^2+a}\right)^{1+\Omega(Q^2)}\right. \\
&+ \left. Bx^{1-\alpha_R}(1-x)^{n(Q^2)}\left(\frac{Q^2}{Q^2+b}\right)^{\alpha_R}(1+f(1-x))\right]/(1.1x)\ ,
\end{aligned}
$$

where the quantities $n(Q^2)$ and $\Omega(Q^2)$ are

$$n(Q^2) = \frac{3}{2}\left(1+\frac{Q^2}{Q^2+c}\right)\ , \qquad (2.46)$$

$$\Omega(Q^2) = \Omega_0\left(1+\frac{2Q^2}{Q^2+d}\right)\ . \qquad (2.47)$$

The function R is parameterized as

$$R = R(x,Q^2) = \frac{b_1}{ln(Q^2/\Lambda^2)}\Theta(x,Q^2) + \frac{b_2}{Q^2} + \frac{b_3}{Q^4+(0.3)^2}\ , \qquad (2.48)$$

where

$$\Theta(x,Q^2) \equiv 1 + 12\frac{Q^2}{Q^2+1}\frac{0.125^2}{0.125^2+x^2}\ . \qquad (2.49)$$

The parameter values are shown in Table 2.6. The R and Θ functions and the related parameters are given in Ref. [65].

Λ	b_1	b_2	b_3
0.2	0.635	0.5747	-0.3534

Table 2.6: The parameters for R-function from Ref.[65]

We show the parameters for the CKMT structure functions (eqns. 2.45−2.47)

in Table 2.7.

Parameter	Value	Parameter	Value	Parameter	Value
A	0.6	a	0.2631	d	1.1170
B	2.695	b	0.6452	f	0.5948
α_R	0.4150	c	3.5499	Ω_0	0.07684

Table 2.7: The parameter values for CKMT parameterization from Ref.[64]

The CKMT structure functions are parameterized at $Q_c^2 = 2$ GeV^2, and this point is used for our extrapolations as the matching point with the perturbative F_i^{TMC}. The extrapolated structure functions below this momentum transfer Q_c are

$$F_i^{TMC}(x, Q^2 \leq Q_c^2) = F_i^{CKMT}(x, Q^2) \frac{F_i^{TMC}(x, Q_c^2)}{F_i^{CKMT}(x, Q_c^2)} \tag{2.50}$$

For F_4^{TMC} and F_5^{TMC} below Q_c, we use the Albright and Jarlskog relations [42].

CHAPTER 3
QUARK MASS EFFECTS IN MUON NEUTRINO-NUCLEON SCATTERING

We present the result of massless $\overline{\text{MS}}$, VFNS (ACOT), and FFNS. The parton distribution functions (PDF) used are the CTEQ6.6M and GJR PDFs. The heavy quark masses are $m_c = 1.3$ GeV, $m_b = 4.5$ GeV for CTEQ6.6M, and $m_c = 1.3$ GeV, $m_b = 4.2$ GeV for GJR. These masses were used in the fits made by the respective PDF groups. All the figures show the results at NLO in QCD, unless noted otherwise.

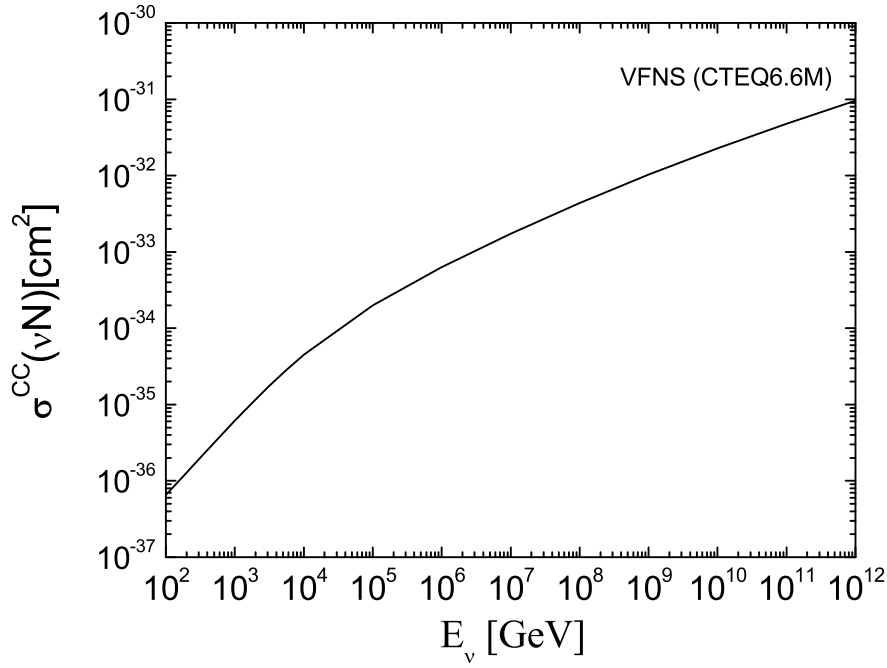

Figure 3.1: The charged current cross section for $\nu_\mu N$ scattering as a function of the incident neutrino energy. The massless $\overline{\text{MS}}$ scheme is used with the CTEQ6.6M PDFs.

Figure 3.1 shows the total DIS charged current cross section of neutrino-nucleon scattering as a function of incident neutrino energy. The cross section grows depending on the E_ν at the low energies, and at the high energies it increases according to the $E_\nu^{0.3}$. On this scale, the difference between the schemes cannot be distinguished.

Thus, we plot the VFNS result obtained with CTEQ6.6M PDF set as representative, and then we compare our evaluation from each schemes with the ratio subsequently.

In figure 3.2, we indicate the F factors, which is the ratio of the cross section of sub-processes to the total cross section. This is from the result of VFNS with the CTEQ6.6M PDF. The F factors include the contributions of both quark and anti-quark labeled on each curve. For instance, the $d\bar{u}$ curve is from

$$F(d\bar{u}) = \frac{\sigma(d\,W^+ \to u) + \sigma(\bar{u}\,W^+ \to \bar{d}) + \sigma(g\,W^+ \to u\bar{d})}{\sigma_{(TOTAL)}} \ . \tag{3.1}$$

This is because these contributions on the gluon splitting process (Fig. 2.3) at NLO cannot be separated.

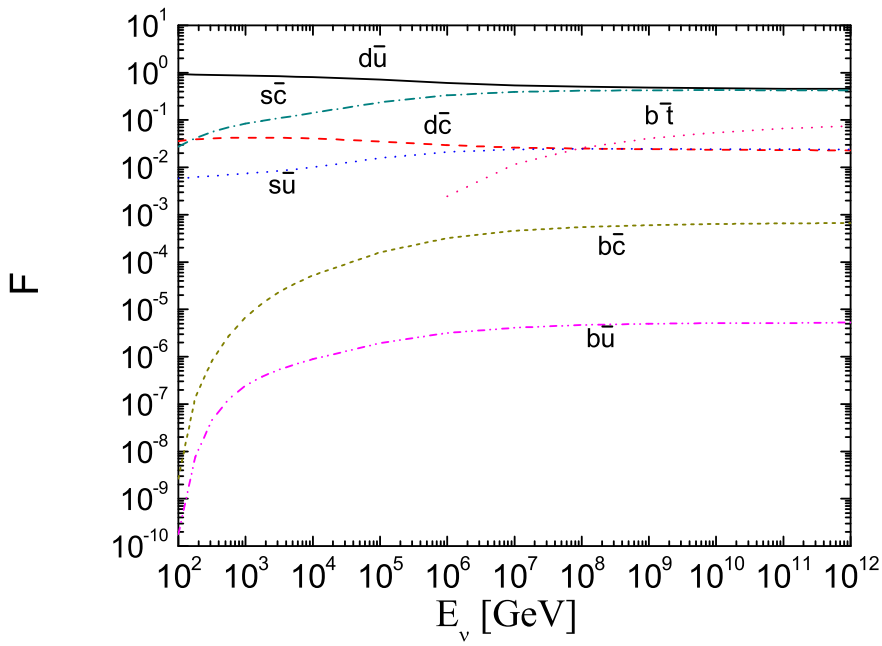

Figure 3.2: The ratio of the flavor contributions to the neutrino-nucleon charged current cross section. The cross section is evaluated using the VFNS with the CTEQ6.6M PDF.

As shown in the graph, the contributions are different according to the flavors and the energy. At low energies, the $d\bar{u}$ contribution dominate since the valence quarks have the most effect. As the energy increases, however, the charm mass

corrections and valence contributions become lower, and the $s\bar{c}$ contribution is raised. Above 10^8 GeV, it is almost equal to the $d\bar{u}$ contribution. In this energy range, $d\bar{c}$ and $s\bar{u}$ contributions are also the same. The sub-processes related with the b quark contributes more at high energies. The contribution of $b\bar{t}$ is the third highest above the energy $E_\nu \sim 10^8$ GeV. Since the PDF sets we use are generated with 3 or 5 constituents, the t quark, with a mass $m_t = 175\, rmGeV$, is not included in the PDF. The $b\bar{t}$ contribution shown in Fig. 3.2 comes from the gluon splitting process at NLO. Other b-related contributions are below 0.1% even at the highest energy because the Cabibbo-Kobayashi-Maskawa (CKM) matrix elements are small.

Now we will show the dependence on the scheme choice. In Fig.3.3, we plot the ratio of the NLO cross section of VFNS to FFNS for CTEQ6.6M and GJR PDFs. The CTEQ6.6M PDF is generated with the five quarks, so the contributions of the heavy quarks, c and b, are omitted when the FFNS is evaluated with CTEQ 6.6M PDF. For the GJR plot, GJRV PDF set is used for the VFNS and the GJRF set for FFNS calculation. In this plot, GJR PDF set is more consistent for comparison since it has PDFs for both VFNS and FFNS.

For the CTEQ6.6M, the VFNS NLO cross section has almost the same value as the FFNS result up to an incident neutrino energy of 10^5 GeV. At higher energies, their ratio varies depending on the energy, and it has the maximum difference at $E_\nu = 10^{12}$ GeV, which is about 3%. For the GJR PDFs, below $E_\nu \sim 10^6$ GeV, the ratio of the VFNS to FFNS cross section is stable, and it decreases as the incident energy increases. The difference is about 13% at the highest energy. This difference is because the heavy quarks are perturbatively generated through gluon splitting in the FFNS, while in the VFNS, they are included in PDFs.

In Fig.3.4, the PDF choice is varied for a given flavor scheme. The ratio of the NLO cross sections with CTEQ6.6 and GJR PDFs are compared for the VFNS and the FFNS. As shown in the figure, the VFNS result is more stable than FFNS result

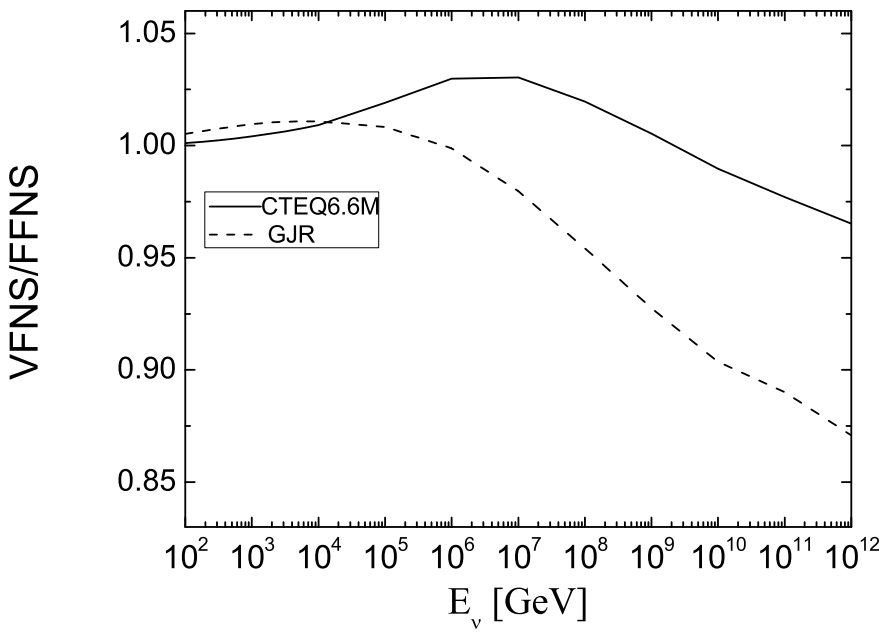

Figure 3.3: The ratio of the NLO charged current σ_{VFNS} to σ_{FFNS} for CTEQ6.6M and GJR PDFs.

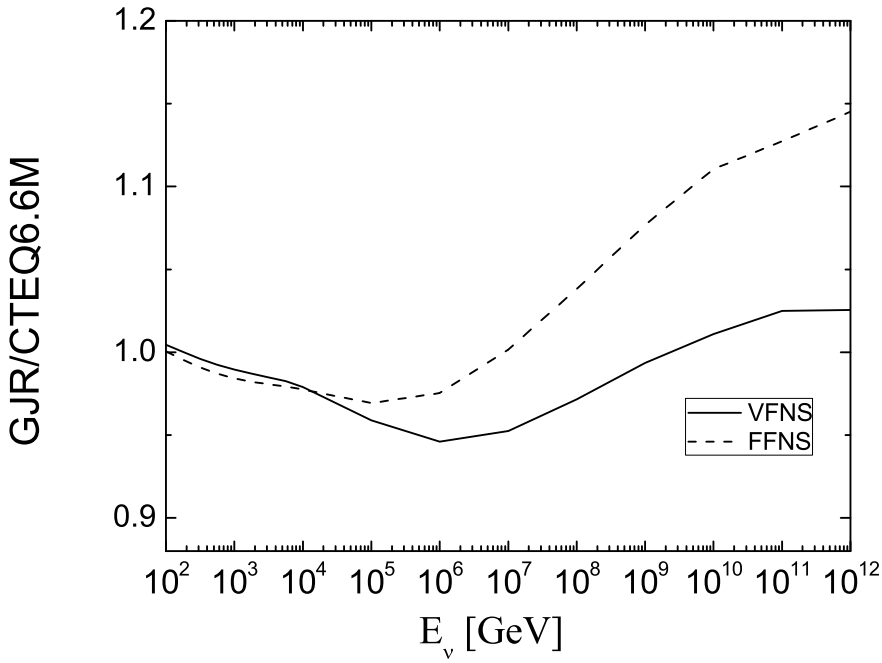

Figure 3.4: Comparison of GJR and CTEQ6.6M PDFs for the NLO charged current σ_{VFNS} and σ_{FFNS}.

for these two PDF choices. The VFNS cross section using GJRV and CTEQ6.6M has the maximum difference at $E_\nu = 10^6$ GeV, about 5%. They differ by about 2.5% at $E_\nu = 10^{12}$ GeV. For the FFNS, the cross sections evaluated using GJRF is close to the results using CTEQ6.6M up to $E_\nu \sim 10^6$ GeV. But, above $E_\nu \sim 10^6$ GeV, their ratio grows depending on the energy and it differs by 15% at the highest energy. This is because the cross sections with CTEQ6.6M PDF in denominator are underestimated due to omitting c and b quarks in evaluation.

For the remaining part, we present the $K_{\rm NLO}$ factor, which is the ratio of NLO cross section to LO cross section. The LO cross section and the NLO cross section are evaluated using the same NLO PDF set for each scheme. So, $K_{\rm NLO}$ factor is

$$K_{NLO} = \frac{\sigma_{NLO}(\text{NLO PDF})}{\sigma_{LO}(\text{NLO PDF})} \ . \tag{3.2}$$

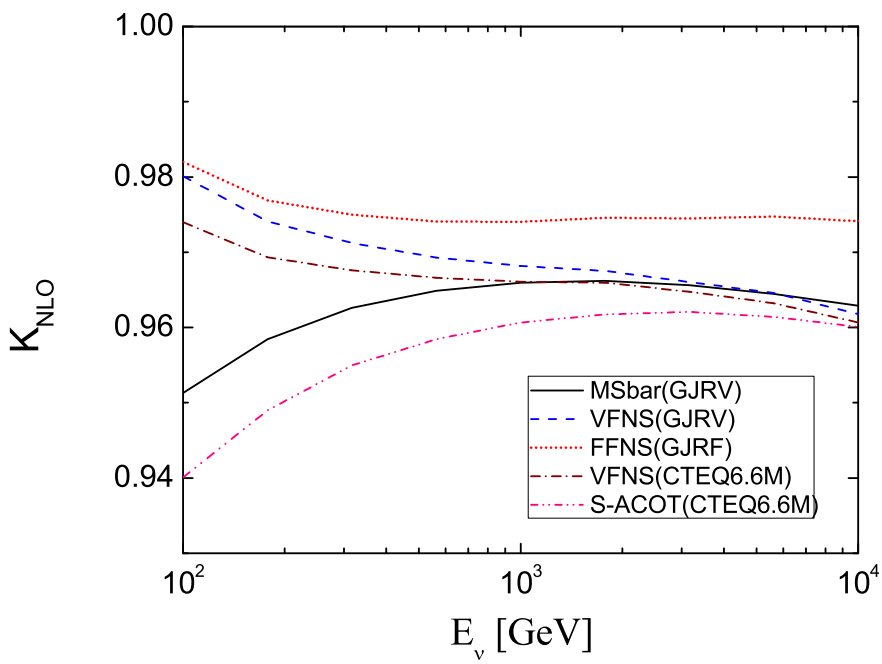

Figure 3.5: $K_{\rm NLO}$-factor, the ratio of the σ_{NLO} to σ_{LO} for the VFNS and FFNS. The LO cross section is evaluated using the same PDFs as the NLO cross section and the scaling variable χ is used.

Figure 3.5 shows the $K_{\rm NLO}$ for each scheme with different PDFs from 10^2 GeV

and 10^4 GeV. In this energy range, the quark masses have a significant effect. The biggest difference between the schemes with the different PDF sets is at 100 GeV, which is about 4%. Above 10^3 GeV, the quark masses have little impact so that the results of the massive VFNS are very close to that of the massless $\overline{\text{MS}}$. The massive VFNS CTEQ6.6M result is between the massless $\overline{\text{MS}}$ and massive VFNS GJRV results below 1 TeV.

The K_{NLO} factor of the FFNS is a close to the VFNS GJRV at $E_\nu = 10^2$ GeV, but the difference increases according to E_ν. The K_{NLO} of the FFNS has about 1.3% higher ratio than that of the VFNS GJRV at 10^4 GeV. Although the K_{NLO} of the FFNS is the highest in the figure 3.5, it does not mean that its actual value is the highest. The NLO charged current cross section of the FFNS with GJRF PDF is about 1% lower than the VFNS GJRV cross section at $E_\nu = 10^4$ GeV. For the LO cross section, FFNS GJRF is lower than VFNS GJRV by 2.5% at the same energy level.

We also compared the results of the ACOT(χ) and the S-ACOT(χ) prescription using CTEQ6.6M PDF in fig. 3.5. At $E_\nu = 100$ GeV, the ACOT(χ) (labeled VFNS (CTEQ6.6M)) result is higher than the S-ACOT(χ) by 3.4%, but their difference decreases as E_ν increases. They differ by less than 1% at 1 TeV, and become nearly identical at 10^4 GeV.

In Fig.3.6, the K_{NLO} factors are shown for the full energy range, $10^2 - 10^{12}$ GeV. The massless $\overline{\text{MS}}$, VFNS and FFNS results are evaluated using the appropriate GJR PDFs. We replace the VFNS results by the massless $\overline{\text{MS}}$ above $E_\nu = 10^9$ GeV to avoid numerical errors related with the subtraction terms. As shown in Fig.3.5, above $E_\nu \sim 10^3$ GeV, K_{NLO} factors of the VFNS and the massless $\overline{\text{MS}}$ is almost equal. The K_{NLO} for the FFNS, however, starts to deviate from the other curves at that energy, and it differs by 25% at 10^{12} GeV.

Fig. 3.7 also shows the K_{NLO} factors for the whole energy range, but the

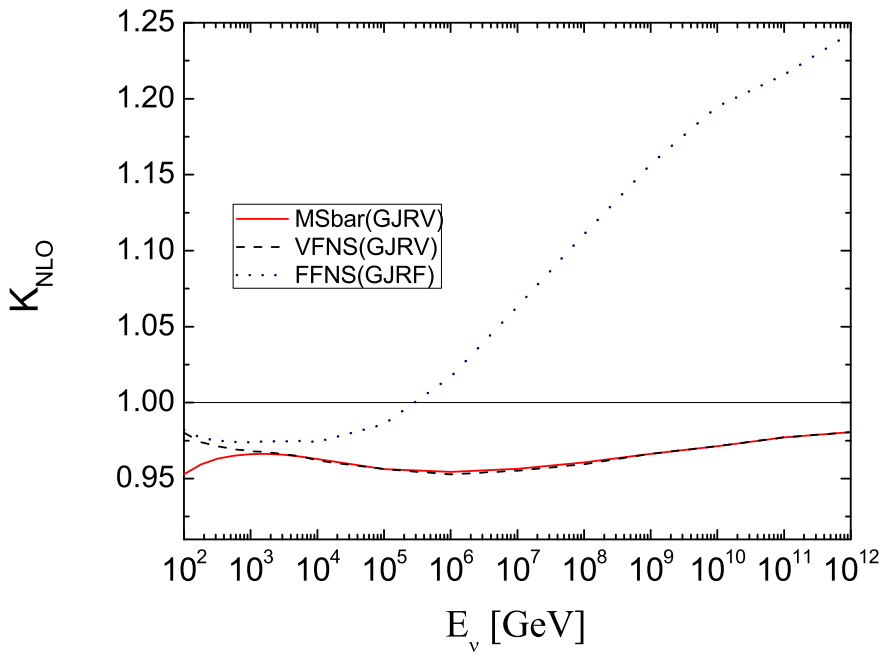

Figure 3.6: $K_{\rm NLO}$-factor: the ratio of the neutrino-nucleon charged current σ_{NLO} to σ_{LO} for $E_\nu = 10^2 - 10^{12}$ GeV. The LO cross section is evaluated using the same PDFs as the NLO cross section. The VFNS cross section is evaluated using the ACOT(χ) or S-ACOT(χ) scheme for $E_\nu \leq 10^9$ GeV.

CTEQ6.6M PDFs are used to calculate the cross sections instead of GJR PDFs. As stated above, the CTEQ6.6M has the five quark constituents, so for the FFNS evaluation, we set the c and b components to zero in the PDF. We also show the impact of an inconsistent scheme choice, labeled as "mixed". The pattern of $K_{\rm NLO}$ factors with CTEQ6.6M PDF is similar to the result with GJR PDF. Above $E_\nu \sim 10^2$ GeV, $K_{\rm NLO}$ of VFNS is nearly equal to the massless $\overline{\rm MS}$ result, and the $K_{\rm NLO}$ of FFNS differs from the result of the other two. In the mixed scheme, the NLO cross section has the contributions of the only light quarks, but the subtraction corrections are affected by the five quarks, including c and b, by the gluon process. A similar K-factor is in Ref. [66], which is evaluated using the three flavor GRV PDF.

Our conclusion from the comparisons of $K_{\rm NLO}$ with different schemes is that the VFNS is most appropriate at high energies. The matrix element corrections to

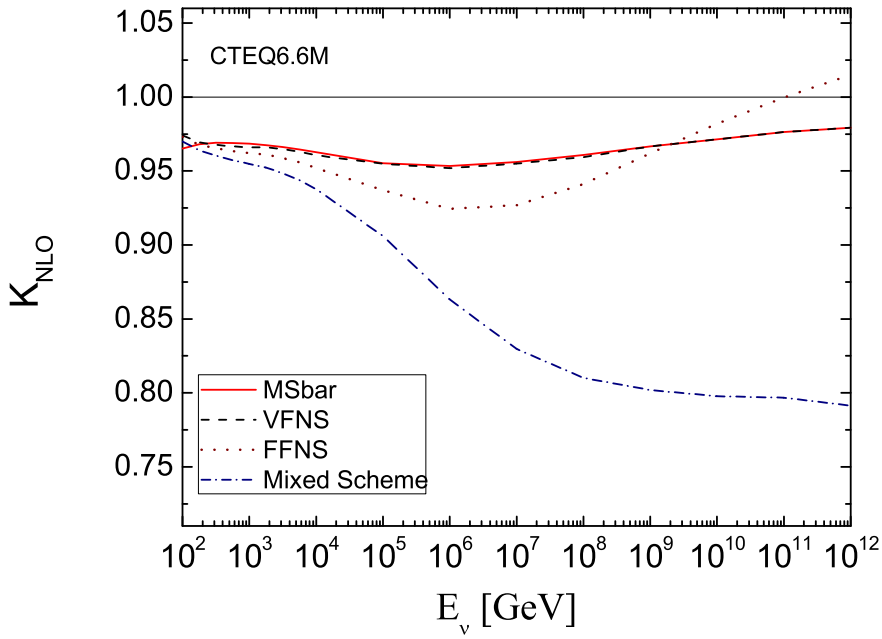

Figure 3.7: K_{NLO}-factor: the ratio of the neutrino-nucleon charged current σ_{NLO} to σ_{LO} for $E_\nu = 10^2 - 10^{12}$ GeV. The CTEQ6.6M PDFs are used. The "mixed scheme" ratio uses 3 flavors of quark PDFs but makes a subtraction for 5 flavors from the gluon fusion term.

the cross sections are stable, and the VFNS matches the massless quark $\overline{\text{MS}}$ cross sections already at $E_\nu = 10^4$ GeV. For the PDFs to evaluate the VFNS, CTEQ6.6M is better choice than GJRV at ultra high energies, because it is fit to five flavor PDFs in energy range where appropriate.

CHAPTER 4
TAU NEUTRINO AND ANTINEUTRINO CROSS SECTIONS

In this section, we discuss the results for tau (anti-)neutrino-nucleon scattering with the tau lepton mass correction. In addition, target mass and quark mass corrections, and low Q extrapolations of the structure functions below $Q^2 = 2$ GeV^2 are included in the evaluation. We set the factorization scale $\mu = Q$, and the hadronic invariant mass $W_{\rm min} = 1.4$ GeV.

Fig.4.1 shows the charged current cross section divided by incident tau (anti-) neutrino for the tau (anti-) neutrino interaction with the nucleon. The upper lines are for the tau neutrino interactions with the nucleons, and the lower lines for the antineutrino-nucleon interactions. These are evaluated with the GJRF PDFs, which

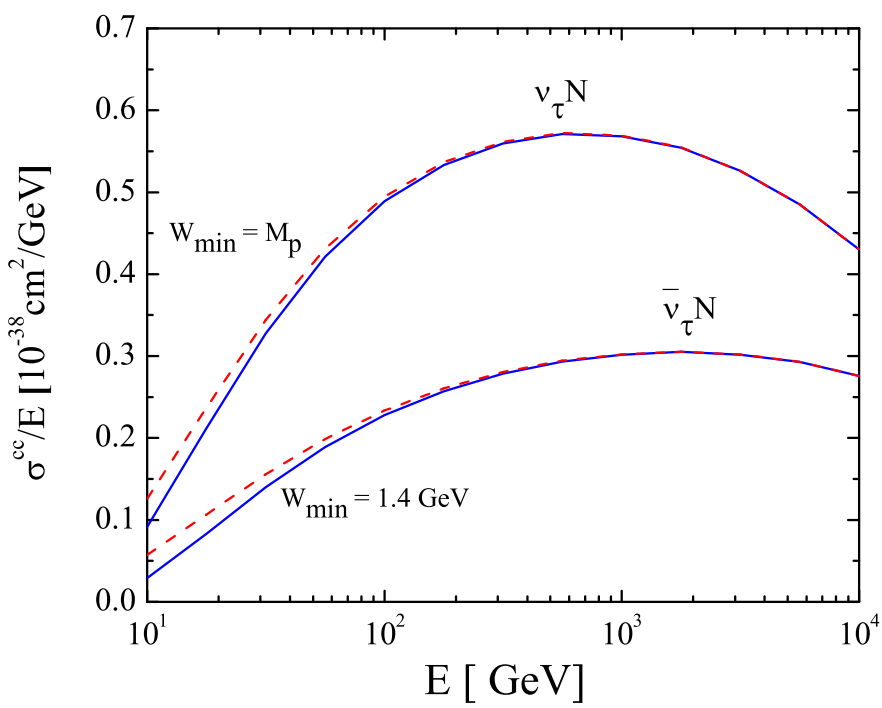

Figure 4.1: The tau neutrino- (upper curves) and antineutrino- (lower curves) isoscalar nucleon charged current cross section, for $W > 1.4$ GeV (blue, solid) and $W > M$ (red, dashed). Target mass corrections, NLO QCD and low Q extrapolations of the structure functions below $Q_c^2 = 2$ GeV^2 are included in the evaluation.

has three flavors. For both cases in the graph, the red-dashed lines indicate the cross section for $W_{\rm min}$ = $\rm M_N$ (0.938 GeV), and the blue-solid lines for $W_{\rm min}$ = 1.4 GeV. The effects on the cross section divided by incident neutrino energy from different $W_{\rm min}$ values are reduced as the incident energy grows, and disappear above $E_\nu \sim 10^2$ GeV. More specific results with additional $W_{\rm min}$ values are indicated in Table 4.1. For reference, we show the cross sections for the tau neutrino and antineutrino interactions with protons in Table 4.2. Both tables include the results with $W_{\rm min}$ = 1.7 GeV as well as $W_{\rm min}$ = 1.4 GeV and $W_{\rm min} = M_N$. Above $E_\nu \sim 10^3$ GeV, σ/E, especially for tau neutrinos, starts to decrease due to the suppression of the W propagator.

Energy [GeV]	$\sigma_{\nu N}$ [10^{-38} cm^2]	$\sigma_{\bar{\nu} N}$ [10^{-38} cm^2]
10	0.916 (1.26, 0.690)	0.291 (0.574, 0.160)
$10^{1.25}$	3.77 (4.22, 3.44)	1.48 (1.90, 1.21)
$10^{1.5}$	10.4 (10.9, 9.97)	4.43 (4.93, 4.05)
$10^{1.75}$	23.7 (24.3, 23.2)	10.6 (11.2, 10.2)
10^2	48.9 (49.5, 48.4)	22.8 (23.4, 22.3)
10^3	5.69×10^2	3.02×10^2
10^4	4.30×10^3	2.76×10^3

Table 4.1: The ν_τ and $\bar{\nu}_\tau N$ charged current cross section using the CKMT parameterization for $Q^2 \leq 2$ GeV^2 in the structure functions. The factorization scale is set to $\mu = Q$, and the minimum hadronic invariant mass is $W_{\rm min}$ = 1.4 GeV (M, 1.7 GeV) in the cross section.

In Fig.4.2, we show the ratio of the tau neutrino(anti-neutrino) nucleon cross section to the muon neutrino(antineutrino) nucleon cross section. The lepton mass

Energy [GeV]	$\sigma_{\nu P}$ [10^{-38} cm^2]	$\sigma_{\bar{\nu} P}$ [10^{-38} cm^2]
10	0.472 (0.646, 0.356)	0.428 (0.840, 0.230)
$10^{1.25}$	2.12 (2.36, 1.94)	2.08 (2.69, 1.69)
$10^{1.5}$	6.21 (6.49, 5.98)	6.04 (6.78, 5.51)
$10^{1.75}$	14.8 (15.1, 14.6)	14.2 (15.0, 13.5)
10^2	31.6 (32.0, 31.4)	29.8 (30.6, 29.1)
10^3	3.99×10^2	3.72×10^2
10^4	3.28×10^3	3.26×10^3

Table 4.2: The ν_τ and $\bar{\nu}_\tau$ -proton charged current cross section using the CKMT parameterization for $Q^2 \leq 2$ GeV^2 in the structure functions. The factorization scale is set to $\mu = Q$, and the minimum hadronic invariant mass is $W_{\rm min} =$ 1.4 GeV (M, 1.7 GeV) in the cross section.

corrected terms in the differential cross section are suppressed in the muon neutrino-nucleon scattering case due to the small mass of the muon, however, they give big corrections to the tau neutrino and anti-neutrino cross sections. As shown in the figure, these corrections make the tau neutrino cross section less than the muon neutrino cross section about 85% at 10 GeV, 25% at 100 GeV and 5% even at 1 TeV. The ratios of the anti-neutrino cross sections are similar to the neutrino results.

Fig.4.3 shows the differential cross section distribution in y, $(1/E)d\sigma/dy$. The results for the tau neutrino, the muon neutrino, and their antineutrino scattering with the nucleon are plotted for (a) $E = 10$ GeV, and (b) $E = 50$ GeV. For muon neutrino interactions, the cross section is almost independent of y above $y \sim 0.1-0.2$, depending on E_ν. This is because at these energies, the valence quarks have main contribution to the cross section, so $d\sigma/dy$ depends on $q(x, Q^2)$. The differential cross section for the antineutrino scattering depends on $(1-y)^2 q(x, Q^2)$ so that it decreases

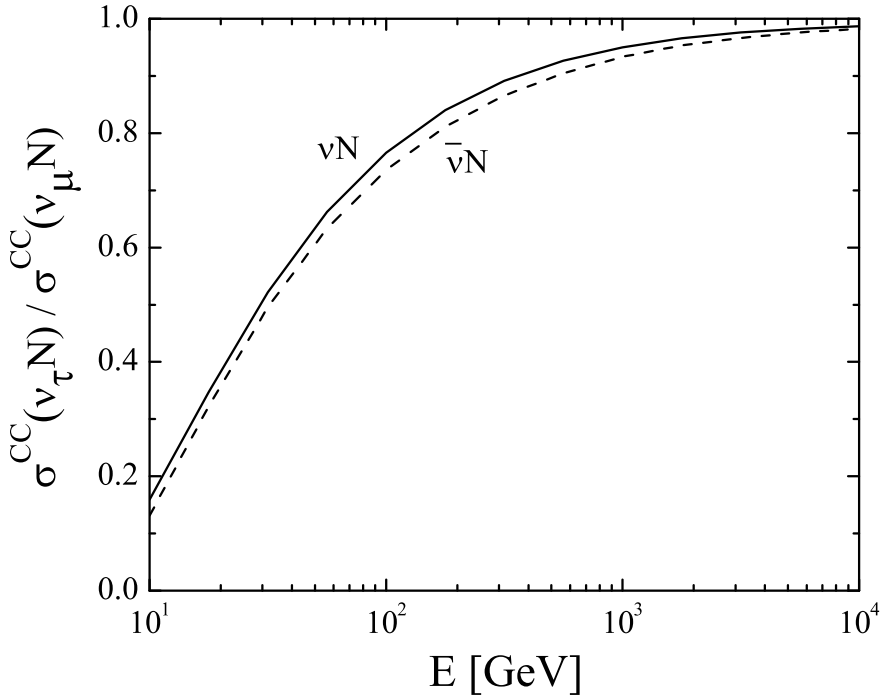

Figure 4.2: The ratio of $\sigma_{CC}(\nu_\tau N)/\sigma_{CC}(\nu_\mu N)$ neutrino- (solid) and antineutrino- (dashed) DIS cross sections.

explicitly as y increases. Both the tau neutrino and anti-neutrino scattering are more affected than the muon results due to the negative F_5 term in the differential cross section (eq. 2.3). In addition, the tau mass in Q^2 (eq. 2.17) and y (eq. 2.20) limit the distribution in y. Comparing (a) and (b), one can see the effects of Q^2 and y become small at the high energies.

The theoretical error on the cross section comes from several components: the low Q^2 extrapolation of CKMT structure functions, the factorization scale μ^2, PDF sets, and the schemes to include the charm quark. We estimate the errors from each component and show the values in Table 4.3, and Table 4.4.

First, we discuss uncertainty from the cut off scale of ${Q_c}^2$. The $Q^2_{\rm min}$ of GJR PDF is set to 0.5 GeV^2, while our standard choice of ${Q_c}^2$ of the CKMT parameterization is 2 GeV^2. So, we compare the cross sections with different $Q^2_{\rm min}$ for PDFs and the CKMT structure functions. For the neutrino interaction, the difference of the cross section

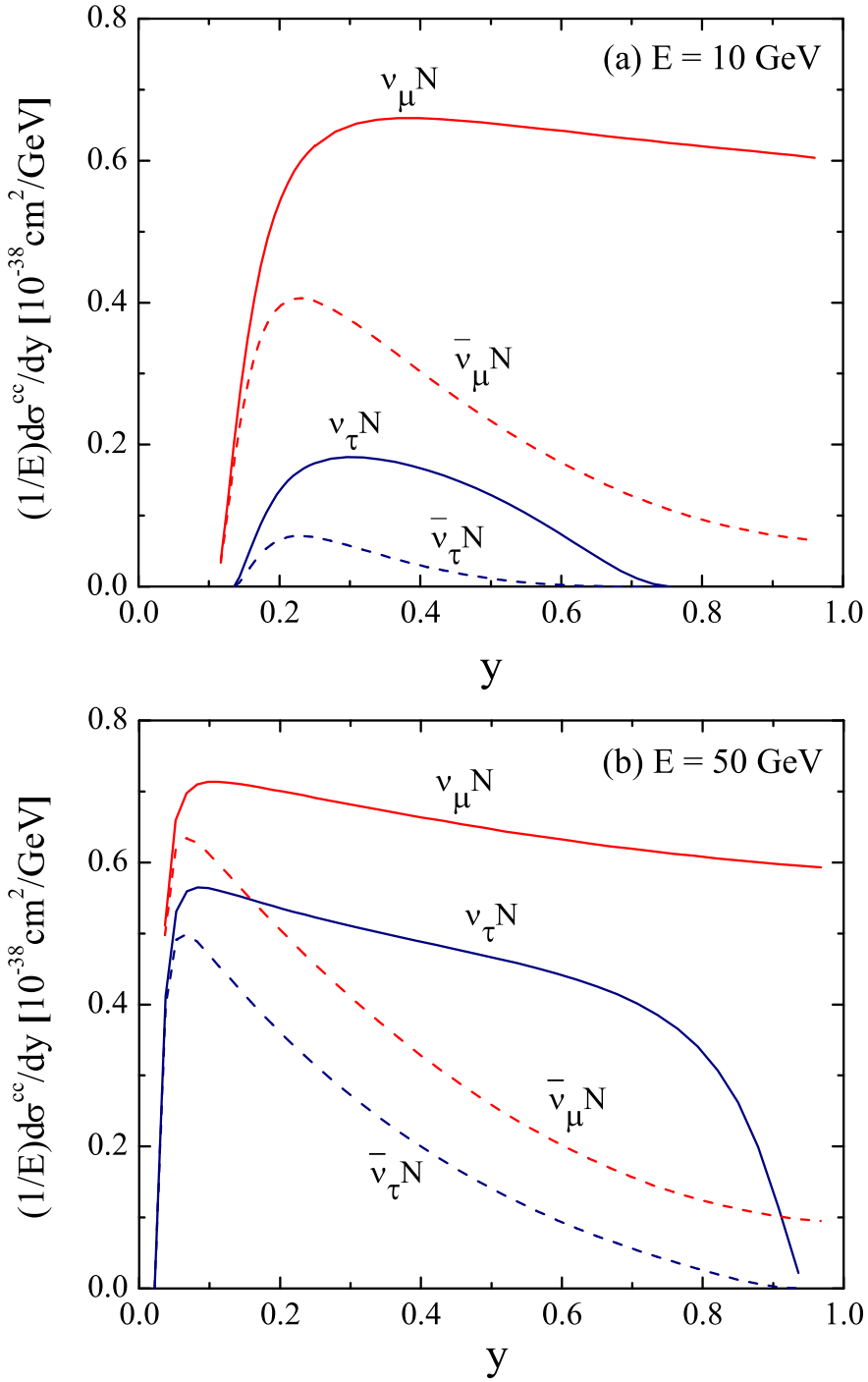

Figure 4.3: The differential cross section $d\sigma/dy/E$ for DIS charged current scattering with an isoscalar nucleon target for (a) 10 GeV and (b) 50 GeV incident energies.

for ${Q_c}^2 = 0.5$ GeV^2 and for ${Q_c}^2 = 2$ GeV^2 is less than 1%. For the antineutrinos, ${Q_c}^2$ has more effect on the cross section. The cross section for ${Q_c}^2 = 0.5$ GeV^2 is about

3% lower than for ${Q_c}^2 = 2$ GeV^2. The difference is reduced to $\sim 1\%$ at 100 GeV, and it is less than 1% at the higher energies.

The cross sections depend more on the factorization scale μ^2. We calculated $\sigma_{\nu_\tau N}$ when μ^2 is $0.5Q^2$ and $2Q^2$, respectively, and compare them with the cross section for $\mu^2 = Q^2$. At 10 GeV, for $\nu_\tau N$ scattering the result for $\mu^2 = 0.5Q^2$ is about 3% higher while it is 4% lower for $\mu^2 = 2Q^2$. For $\overline{\nu}_\tau N$ interaction, the discrepancies are 4.6% and -5.5%, respectively. We took the larger absolute number between the error for $0.5Q^2$ and $2Q^2$ for calculation the total uncertainties, shown in Fig. 4.4.

The evaluation of the cross section using CTEQ6.6M PDF yields the results $0.6-2.7$ % higher than the cross section for GJRF PDF for $\nu_\tau N$ scattering, and $1.0-3.0\%$ higher for $\overline{\nu}_\tau N$ interaction.

The CTEQ6.6M PDF has a set of 44 variations of the best fit parameter values. These 44 sets give the difference in the $\nu_\tau N$ cross section by 2.7% at 10 GeV, and it is reduced to 1.4% at 10^4 GeV. For the $\overline{\nu}_\tau N$ cross section, the error is 3.6% at 10 GeV, and 2.0% at 10^4 GeV.

The final factor considered is the scheme to deal with the quark masses. We used the massless $\overline{\text{MS}}$, ACOT, and SACOT scheme to evaluate the cross section for the CTEQ6.6M PDF, and compare the results to the fixed flavor number scheme (FFNS) cross section including the charm quark mass correction. We counted this error in the energy range from $E = 100$ GeV to $E = 10$ TeV, since the charm contributions are negligible at 10 GeV. Like the factorization scale case, we used the biggest discrepancy to estimate total uncertainties among the results of the three flavor schemes. At $E = 100$ GeV, the SACOT result is lower than the FFNS result by 3.4% for $\nu_\tau N$, and by 5.5% for $\overline{\nu}_\tau N$, which are the biggest errors. At higher energies, the contributions of the SACOT are reduced, and the $\overline{\text{MS}}$ results are used for both $\nu_\tau N$, and $\overline{\nu}_\tau N$.

The estimates of the combined uncertainties for all the contributions discussed

E	44 sets	6.6/GJRF	$\overline{\text{MS}}$/FFS	ACOT/FFS	SACOT/FFS	${Q_c}^2$	μ^2
10	2.74	2.68	-	-	-	-0.62	-4.25
10^2	1.79	0.61	-0.67	0.12	-3.43	0.55	-1.01
10^3	1.57	1.54	0.69	0.43	-0.27	0.13	-0.41
10^4	1.43	2.21	1.13	0.92	0.83	0.02	-0.36

Table 4.3: The estimated errors for ν_τN scattering (%).

E	44 sets	6.6/GJRF	$\overline{\text{MS}}$/FFS	ACOT/FFS	SACOT/FFS	${Q_c}^2$	μ^2
10	3.58	3.03	-	-	-	-3.25	-5.54
10^2	2.45	0.96	-1.2	0.25	-5.37	1.14	-1.83
10^3	2.33	2.41	1.29	0.80	-0.35	0.26	-0.65
10^4	2.04	2.82	1.77	1.43	1.31	0.03	-0.47

Table 4.4: The estimated errors for $\bar{\nu}_\tau$N scattering (%).

above are shown in Fig.4.4. The error estimate is calculated by the quadrature,

$$\text{Error Estimate} = \sqrt{\sum_i \sigma_i^2}\ , \tag{4.1}$$

where σ_i is indicated for each scattering process in Table 4.3 and 4.4. At 10 GeV, the largest error comes from the factorization scale in the structure functions, and at 100 GeV, the flavor scheme has the largest effect on the total theoretical error. In addition, the contributions of the PDF choice are the most important at the highest energy $E = 10$ TeV.

Tau neutrinos are the signal of neutrino oscillations, and they are searched by the DeepCore detector in IceCube and ICARUS T600 detector in the Gran Sasso

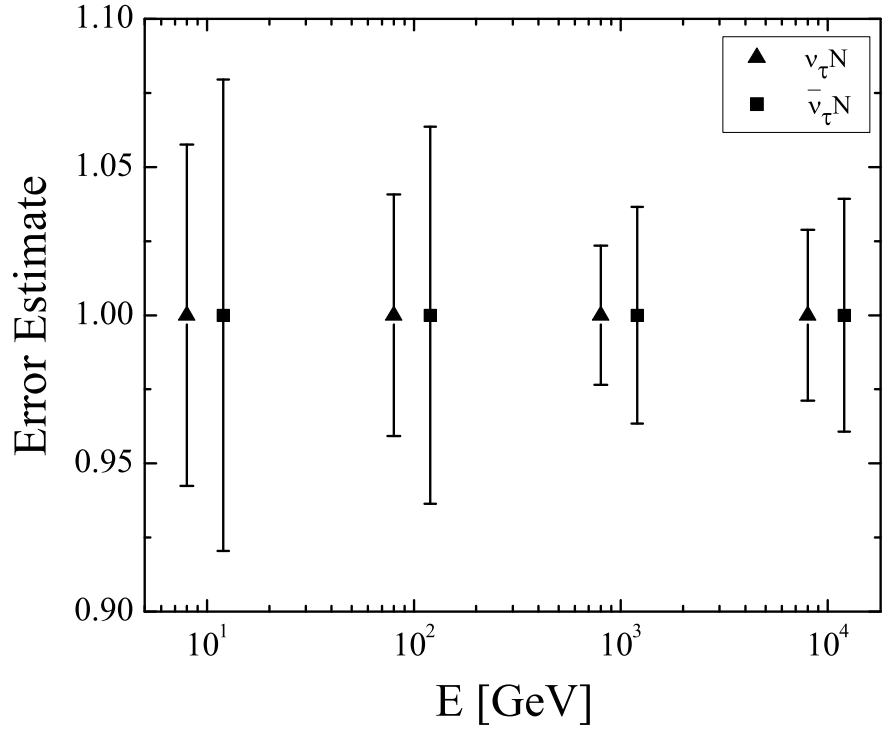

Figure 4.4: An estimate of the theoretical errors for ν_τ (triangles) and $\bar{\nu}_\tau$ (squares) deep-inelastic charged current cross sections.

experiment. We have a new evaluation of the tau and (anti-)neutrino charged current cross sections and the theoretical errors. The theoretical errors have a variety of sources, including PDFs and QCD corrections, depending on the neutrino energy. Our evaluations will play an important role in interpretation of $\nu_\tau N \to \tau X$ events in these experiments.

CHAPTER 5
APPLICATION: RADIO CHERENKOV SIGNALS FROM THE MOON

5.1 Cosmogenic Neutrinos

In the previous chapters, we have investigated the high energy neutrino cross section. The sources of high energy neutrinos are divided into astrophysical accelerator and non-accelerator sources. Astrophysical accelerator sources are subdivided into galactic sources like Supernovae remnants (SNRs), and extragalactic sources such as Gamma Ray Bursts (GRB), and Active Galactic Nuclei (AGN). Non-accelerator sources are, for example, the annihilation of dark matter (DM) particles, and decays of super massive particles. Ultra high energy (UHE) cosmic rays interact with background radiation, producing a guaranteed flux of UHE neutrinos [67, 68].

At very high energies, the cosmic rays, mostly protons, interact with the cosmic microwave background (CMB) photons. Through this interaction, the pions are created, primarily via $\Delta(1232)$ production:

$$p + \gamma \;\rightarrow\; \Delta^+ \;\rightarrow\; n + \pi^+ \;, \text{ and } \quad p + \pi^0 \;. \tag{5.1}$$

In order for the interaction to occur with $T = 2.7$ K photons, the proton must have an energy of at least $E_p \sim 6 \times 10^{19}$ eV $= 6 \times 10^{10}$ GeV [69].

Because cosmic rays of high enough energy are attenuated by this interaction, the cosmic ray spectrum is diminished at ultra high energies. This is called the GZK cutoff, named after Greisen, Zatseptin and Kuzmin [70, 71]. The GZK cutoff is not calculated as the exact value because of the broad distribution of the CMB photons, but this threshold energy is known as the characteristic cutoff for cosmic ray energies.

The pions from Δ-decays subsequently decay, producing the ultra high energy neutrinos.

$$\pi^+ \rightarrow \mu^+ \nu_\mu \rightarrow (e^+ + \nu_e + \overline{\nu}_\mu) + \nu_\mu \;. \tag{5.2}$$

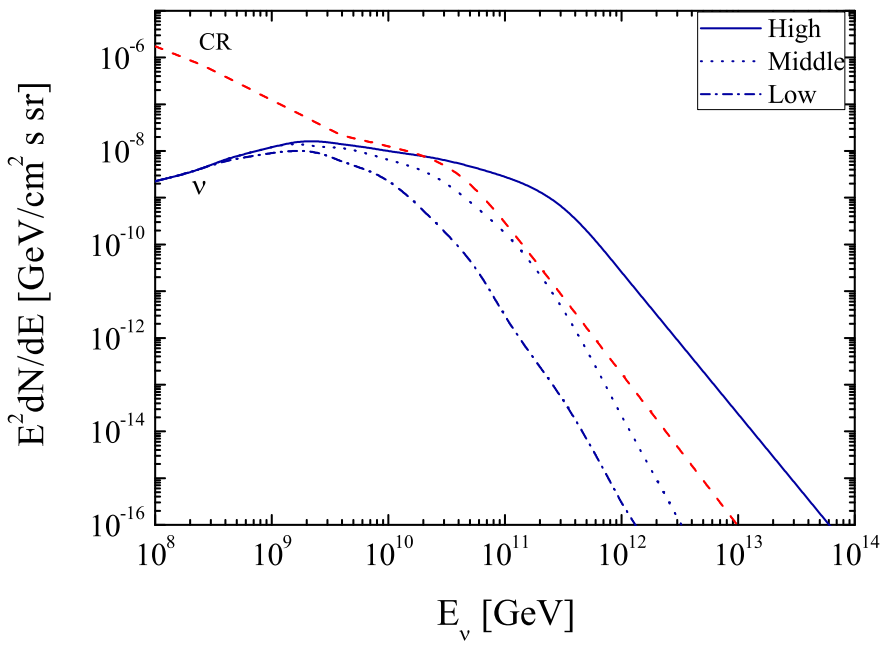

Figure 5.1: The flux of cosmic rays (red, dashed) shown in Ref. [53] and the flux of cosmogenic neutrinos (blue) in Ref. [52]. The neutrino fluxes are estimated with the maximum proton energy in sources of $E_{p,max} = 10^{11}$ GeV (Low, dot-dashed), $10^{11.5}$ GeV (Middle, dotted) and $10^{12.5}$ GeV (High, solid).

Neutrinos are also produced by neutron decays,

$$n \to p + e^- + \overline{\nu}_e \ . \tag{5.3}$$

These neutrinos are called the cosmogenic neutrinos or GZK-neutrinos.

The fluxes of the cosmogenic neutrinos have been estimated by several groups [52, 72, 73, 74]. There are uncertainties in calculating the flux depending on the assumptions on, e.g., the cosmic ray compositions and source evolutions. Most recently, Kotera, Allard, and Olinto calculated the neutrino fluxes for some different models according to source evolutions, various transitions, cosmic ray compositions and the maximum acceleration energy including corresponding spectral index in Ref. [52]. The uncertainties due to other than the maximum acceleration energy have an effect on the neutrino fluxes primarily at relatively low energies. But, the effect of the maximum acceleration energy appears in the fluxes above 10^9 GeV. In this thesis, we

are interested in the energy range of 10^8 GeV or above, so we use the fluxes estimated according to the maximum acceleration energies $E_{p,max}$ for our calculations, which are shown in Fig. 5.1. These fluxes are estimated with the assumption that the primary of cosmic rays is protons. The dot-dashed, dotted and solid lines are for $E_{p,max} = 10^{11}$ eV, $10^{11.5}$ eV and $10^{12.5}$ eV, respectively, which we will call "low", "middle" and "high".

There are several experiments to measure these cosmogenic neutrinos by detecting the radio Cherenkov signals from neutrino interactions. Some experiments such as FORTE [11], RICE [12], and ANITA [13] search for the signals from the Earth's polar ice sheets in Greenland and Antarctica. Some other searches, e.g., GLUE [14], SKA [15], and NuMoon [16] use the moon as the target for the interactions. Recently, RESUN project at the University of Iowa reported a limit from lunar observations [17]. So far, none of these have observed neutrinos. But, non-detection potentially gives the limit of the cross sections if the cosmogenic neutrino flux is given. We concentrate on the evaluation of the radio signals from the lunar target. We investigate the detection parameters that would allow a measurement or a constraint of the neutrino-nucleon cross section.

Since neutrinos are weakly interacting particles, the large area of detector is required to detect neutrinos. The Moon was suggested for such a large detector by Dagkesamanskii and Zheleznykh [75] based on the idea that high energy neutrinos produce showers by interacting with nuclei in the lunar regolith. The showers are divided into the electromagnetic showers and the hadronic showers. While the showers develop in the lunar regolith, electrons come out from the atoms in the regolith by Compton scattering. In the hadronic showers, the short-lived mesons such as pion or kaon are produced, and these mesons soon decay into electron and positron. Positrons in the hadronic shower annihilate via interaction with electrons. Due to these processes, about 20% of electron excess is generated. The group of electrons

moves faster than light in the lunar regolith, so the Cherenkov radiation is emitted with the Cherenkov cone angle, $\theta_c \sim \cos^{-1}(1/n_r) = 55^\circ$ [76]. Here, n_r is the index of refraction of the Moon, which is 1.73.

Cosmic rays also induce hadronic showers, and generate the Cherenkov signal as neutrinos do [77]. The cosmic rays have a larger flux than neutrinos at relatively lower energies, but the cosmic ray flux decreases rapidly with energy. The GZK cutoff further suppresses the UHE cosmic ray flux. The cosmic ray flux is shown in Fig. 5.1 with the cosmogenic neutrino fluxes. The presented cosmic ray flux is obtained using the parameterization of the Pierre Auger Collaboration in Ref. [53].

5.2 Neutrino Cross Sections and Effective Angle

The neutrino cross section appears via the neutrino interaction length, which enters into neutrino flux attenuation in the interaction probability. The neutrino interaction length is inversely proportional to the neutrino cross section, which is defined to be

$$L_\nu \equiv \frac{1}{\sigma_{\nu N}^{tot} N_A} \tag{5.4}$$

with Avogadro's number $N_A = 6.022 \times 10^{23}$. This has the dimension of g/cm^2, or centimeters of water equivalent (cmwe) distance, which is converted to distance by dividing by the density of the material. In water, 1 g/cm^2 converts to 1 cm.

The standard model neutrino interaction length is shown in Fig. 5.2. In order to obtain the total neutrino nucleon cross sections, we use the charged current cross sections used in Fig. 3.1, which includes the top quark contribution, and the ratio of the neutral current cross section to the total cross section in Ref. [87]. The total cross section is obtained by dividing the charged current cross section by $1 - r_{NC}$:

$$\sigma_{\nu N}^{tot} = \frac{\sigma_{CC}}{1 - r_{NC}} \ , \tag{5.5}$$

where the ratio of the neutral current cross section to the total cross section, $r_{NC} = \sigma_{NC}/(\sigma_{NC} + \sigma_{CC})$. The parameterization in Ref. [87] gives approximately a constant

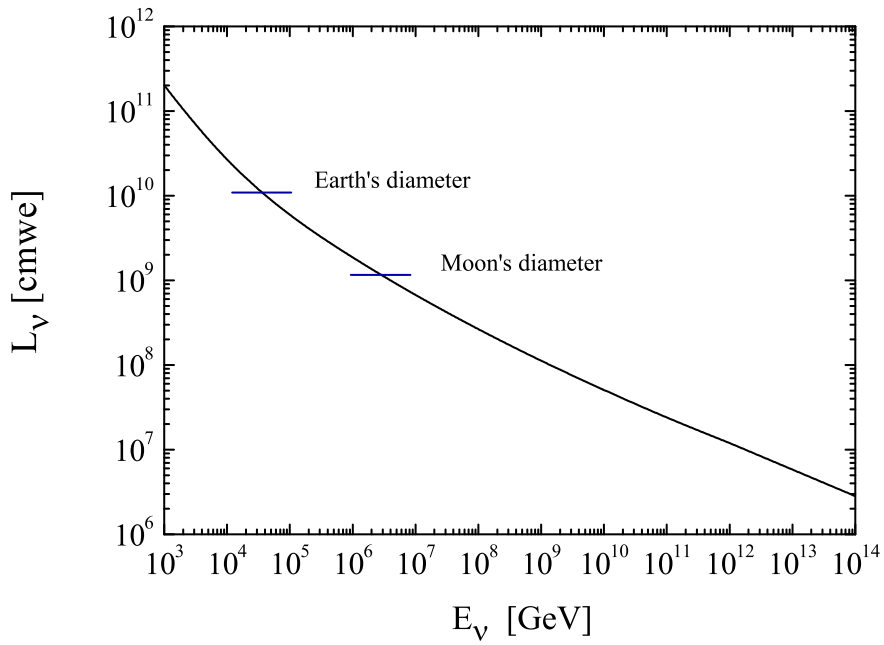

Figure 5.2: The neutrino interaction length (in centimeters water equivalent distance) as a function of energy. The diameters of the Earth and the Moon are also indicated.

of 1.43 as r_{NC}.

The interaction length dependence on the incident neutrino energy is important. The Moon's diameter in cmwe is approximately 1.16×10^9cmwe, which is indicated in Fig. 5.2 along with Earth's diameter. This diameter of the Moon corresponds to the neutrino interaction length for an incident neutrino energy of about 10^6 GeV. Neutrinos with incident energy lower than 10^6 GeV will not be attenuated inside the Moon. However, we consider the cosmogenic neutrinos for the energy of 10^8 GeV or higher, so the effect of attenuation is important in our evaluation of interaction rates.

As indicated in Fig. 5.3, we separate neutrinos as "upward" neutrinos and "downward" neutrinos according to the distance that they move inside the Moon. Upward neutrinos are incident on the backside of the Moon and traverse it until they interact, while downward neutrinos are incident and interact on the surface. The effect of attenuation is primarily in upward neutrinos, although we discuss neutrino attenuation for downward neutrinos with enhanced cross sections later in this chapter.

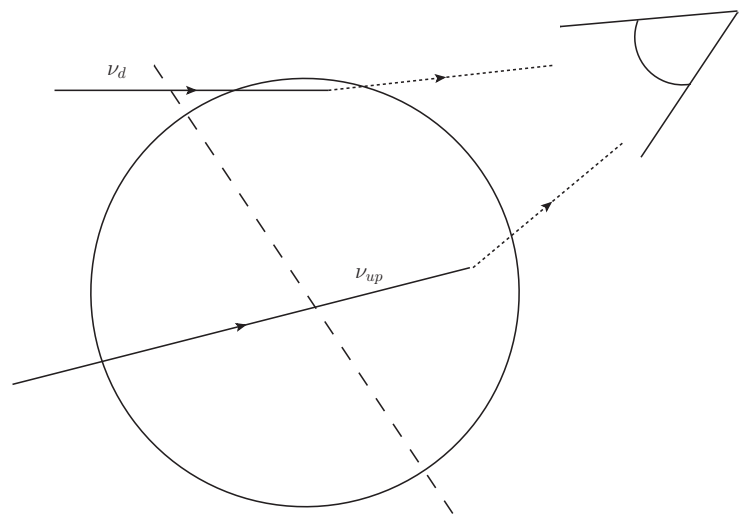

Figure 5.3: upward neutrino and downward neutrino

The upward neutrino event rate is affected by the specific signal and neutrino regeneration. For muon neutrinos, regeneration occurs through neutrino neutral current interactions, and for tau neutrinos through neutrino production and decay [49, 50]. The neutrino regeneration through the neutral current interaction can be included via an effective cross section, and we express it as σ, which scales $\sigma_{\nu N}^{tot}$,

$$\sigma \equiv \sigma_{\nu N}^{eff} = \kappa \sigma_{\nu N}^{tot} \ . \tag{5.6}$$

We can estimate κ using the neutrino flux including regeneration with some approximations. The neutrino flux as a function of column depth X is

$$\frac{d\Phi(E, X(\theta))}{dX} = -\frac{\Phi(E, X(\theta))}{L_\nu} + N_A \int_{E_\nu}^{\infty} dE' \Phi(E', X(\theta)) \frac{d\sigma_{NC}(E', E)}{dE} \ . \tag{5.7}$$

Using

$$\frac{d\sigma_{NC}(E', E)}{dE} \simeq r_{NC} \sigma_{\nu N}^{tot}(E') \delta(E - (1 - \langle y \rangle) E') \ , \tag{5.8}$$

where the neutrino inelasticity is $y = (E' - E)/E'$, and a power law spectrum $\Phi(E, X(\theta)) \sim E^{-\gamma}$ and a neutrino cross section scaled with energy $\sigma_{\nu N}^{tot} \sim E^{\delta}$, we

can rewrite equation 5.7 as

$$\begin{aligned}\frac{d\Phi(E,X(\theta))}{dX} &= -\big(1-r_{NC}(1-\langle y\rangle)^{\gamma-\delta-1}\big)\frac{\Phi(E,X(\theta))}{L_\nu} \\ &= -\kappa\frac{\Phi(E,X(\theta))}{L_\nu}\ ,\end{aligned}$$

where

$$\kappa = -\big(1-r_{NC}(1-\langle y\rangle)^{\gamma-\delta-1}\big)\ . \tag{5.9}$$

Here, we define the effective interaction length for attenuation with λ as

$$\lambda \equiv 1/\sigma N_A = L_\nu/\kappa\ . \tag{5.10}$$

More steps for derivation of attenuation length are presented in Appendix A. See also Ref. [48].

At high energies, the inelasticity $\langle y\rangle \simeq 0.2$ and the fraction of the neutral current cross section to the total cross section r_{NC} is approximately 0.3. In addition, δ for the standard model cross section is 1/3. With these conditions, $\kappa \simeq 0.71$ for $\gamma = 2$. The value of κ varies according to the spectral value of γ, but it is not very sensitive to the exact choice of γ. We use the $\kappa = 0.71$ in our evaluation, and we define the attenuation distance λ to include the regeneration effect as indicated above.

The upward neutrino event rate Γ_u in a detector with a cross sectional area $\mathcal{A}$ and depth d can be approximated by

$$\Gamma_u = \int dE_\nu d\Omega_\nu d\hat{\mathcal{A}}\cdot\hat{n}(\theta_\nu)drP(E_\nu,\theta_\nu,r)\Phi(E_\nu,X(\theta_\nu)). \tag{5.11}$$

This equation includes the attenuation effect for a neutrino passing through a sphere via the neutrino flux,

$$\Phi(E_\nu,X(\theta_\nu)) \simeq e^{-2R\cos\theta_\nu/\lambda}\Phi(E_\nu,0)\ , \tag{5.12}$$

with column depth of the diameter of $2R$. The neutrino flux $\Phi(E_\nu,X)$ is in the unit of neutrinos/(GeV cm^2 s sr), and the angle θ_ν is the incident angle of the neutrino flux with respect to the normal to the surface, as shown in Fig. 5.4. Here, $R = R_M\rho_M$ for

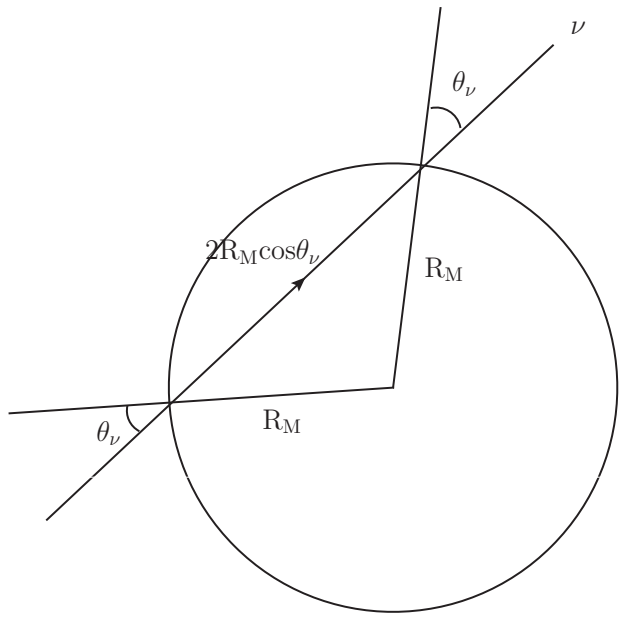

Figure 5.4: Upward neutrino passing through a sphere.

a radius of the Moon $R_M = 1737.1$ km and its density $\rho_M = 3.34$ g/cm^3. We assume that the incident neutrino flux is isotropic.

The quantity $dr\ P(E_\nu, \theta_\nu)$ is the probability the neutrino of incident energy E_ν produces a signal in the interval dr. This probability depends linearly on the neutrino cross section for the specific signal (σ_s), so it can be written as $drP(E_\nu, \theta_\nu) = dr\sigma_s N_A \rho$. The effective volume of the detector is V, where $dV = drd\mathcal{A}$. We consider detection near the surface, where for upward neutrino fluxes, the depth of the detector is negligible.

For a detector near the surface which is approximately isotropic, $\hat{\mathcal{A}} \cdot \hat{n}$ and the path length of the neutrino in the detector are independent of the direction of incident neutrino.

$$P^{iso}(E_\nu, \theta_\nu, L) \simeq P^{iso}(E_\nu, 0, L) \ . \tag{5.13}$$

From Eq. 5.11 and Eq. 5.12, the upward event rate can be expressed with the effective

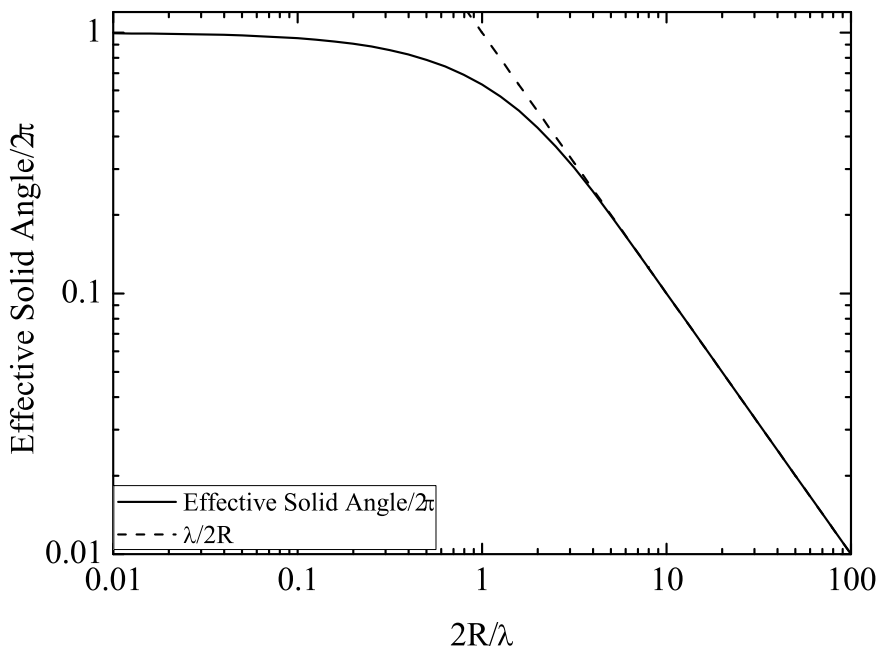

Figure 5.5: The effective solid angle divided by 2π as a function of the ratio of the diameter to the attenuation distance ($2R/\lambda$). The dashed line shows the quantity of $\lambda/2R$. The diameter is in water equivalent distance.

solid angle Ω_{eff}^{iso}, which is

$$\begin{aligned}\Omega_{eff}^{iso} &= 2\pi\int_0^{\pi/2} d\theta_\nu \sin\theta_\nu e^{-2R\cos\theta_\nu/\lambda} \\ &= 2\pi\left(1-e^{-2R/\lambda}\right)\frac{\lambda}{2R}\ . \end{aligned} \tag{5.14}$$

The effective solid angle depends only on the ratio $2R/\lambda$. We show this angle divided by 2π in Fig. 5.5 with the scaling factor which is $\lambda/2R$. The scaling factor is indicated as the dashed line, and shows the pattern of the angular integral according to the ratio of the diameter of the Moon to the interaction length. For small interaction length ($\lambda < R/2$), the effective solid angle can be used as $\Omega_{eff}^{iso} \simeq \pi\lambda/R$ with exponential contribution neglected in Eq. 5.14.

Even if we don't assume that the detector is isotropic, the result is the same. For a detector with the area of $\mathcal{A}$ and the depth of d shown in Fig. 5.6, $\hat{\mathcal{A}}\cdot\hat{n}$ in the integral is $\mathcal{A}\cos\theta_\nu$, and the infinitesimal depth is $dr\cos\theta_\nu$. So, $\int dr P(E_\nu,\theta_\nu,r)$ can be

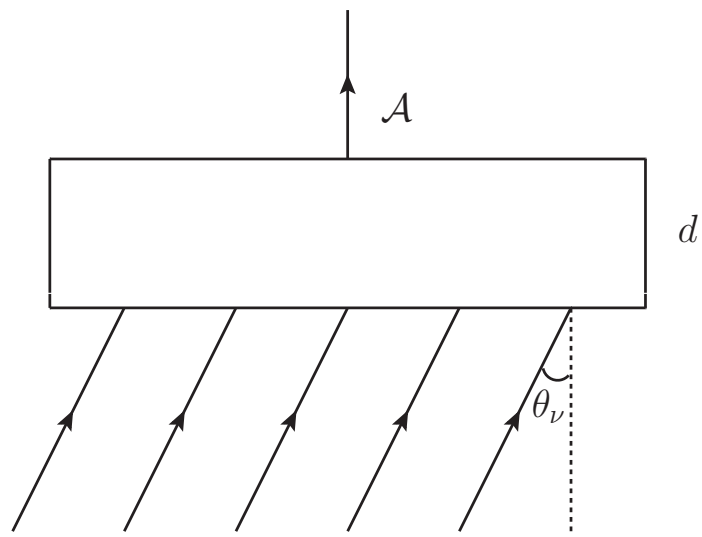

Figure 5.6: The detector with incident neutrinos. The detector has the area of $\mathcal{A}$ and the depth of d. Neutrinos are incident to the surface with an angle of θ_ν from the normal.

expressed as $\sigma_s N_A \rho d/\cos\theta_\nu$ in terms of the detector depth d, assuming that there is no neutrino attenuation through the detector. Then, the terms in the integral of Eq. 5.11, $\hat{\mathcal{A}} \cdot \hat{n}(\theta_\nu) dr P(E_\nu, \theta_\nu, r)$ lose the angular dependence, and the remaining terms are involved in the effective solid angle which are not affected by the detector. So, the results are the same as for an isotropic detector.

Summing up these all pieces, Eq. 5.11 is rewritten as

$$\Gamma_u = \int dE_\nu \Omega_{eff}^{iso} dr P(E_\nu, 0, r) \mathcal{A}_{eff} \tag{5.15}$$

with effective solid angle Ω_{eff}^{iso} and the effective area $\mathcal{A}_{eff}$. For a small interaction length relative to the column depth $2R$, the cross section dependence of the event rate is

$$\Gamma_u \sim \mathcal{A}_{eff} \pi \frac{\sigma_s}{\sigma} \frac{d\rho}{R} \ . \tag{5.16}$$

The similar result is in Ref. [50].

The Fig. 5.6 can be also applied to neutrino induced radio Cherenkov signals with the angle θ_ν and the depth d replaced by θ_ν and L_γ, respectively.

5.3 The Cherenkov Signals from Neutrinos

In order for the neutrino induced radio Cherenkov signals to be evaluated completely, the radio Cherenkov signal production, attenuation and refraction at the lunar surface have to be included in evaluation. These are included via the effective aperture A_ν, which enters into the neutrino detection rate (Γ) is

$$\Gamma = \int_{E_{min}} dE_\nu \Phi(E_\nu, X) A_\nu(E_\nu) \ , \tag{5.17}$$

where $\Phi(E_\nu, X)$ is the neutrino flux. For the effective aperture, we take the analytic expression evaluated by Gayley, Mutel, and Jaeger [48]. The effective aperture $A_\nu(E)$ combines the effective area, the neutrino interaction probability and the effective solid angle, and it is comprised of three terms,

$$A_\nu(E) = A_{ds} + A_{dr} + A_u = A_0 P_\nu(E) \ , \tag{5.18}$$

where

$$P_\nu(E) = \frac{(n_r^2 - 1)}{8n_r} \frac{L_\gamma}{L_\nu} f_0^3 \Delta_0(\Psi_{ds} + \Psi_{dr} + \Psi_u) \ . \tag{5.19}$$

In this equation, the index of refraction $n_r = 1.73$, the maximum geometric lunar aperture $A_0 = 4\pi(\pi R_M^2)$, and the radius of the Moon $R_M = 1{,}737.1$ km. The L_γ and L_ν are the interaction lengths of photons and neutrinos, respectively. For the L_γ, we use the expression in Ref. [48],

$$L_\gamma = 5 \times 10^{-6} R \left(\frac{\nu}{\mathrm{GHz}} \right)^{-1} \ , \tag{5.20}$$

with $R = R_M \times \rho$, and the density of the lunar regolith, $\rho = 1.8$ g/cm^3. The neutrino interaction length L_ν is

$$L_\nu = \frac{1}{\sigma_{\nu N}^{tot} N_A} \ , \tag{5.21}$$

as discussed in the previous section.

The parameter f_0 is the ratio of the thickness of the Cherenkov cone at the $1/e$

full thickness to the thickness at the minimum detectable electric field [48],

$$f_0 = \sqrt{\ln\left(\frac{0.6\varepsilon_0}{\varepsilon_{min}}\right)} \ , \tag{5.22}$$

where ε_{min} is the minimum detectable electric field, and ε_0 is the maximum field, which depends on the distance to the moon $d = 3.8 \times 10^8$ m, the energy of the neutrino induced shower E_s, and the radio frequency of the radiation ν,

$$\varepsilon_0 = 0.0845\left[\frac{d}{\mathrm{m}}\right]^{-1}\left[\frac{E_s}{\mathrm{EeV}}\right]\left[\frac{\nu}{\mathrm{GHz}}\right]\left[1 + (\frac{\nu}{2.32})^{1.23}\right]^{-1} \ . \tag{5.23}$$

The shower energy E_s is approximately,

$$E_s = \langle y \rangle \, E_\nu \ = \ 0.2 E_\nu \ . \tag{5.24}$$

The angular width Δ_0 is the half width of the Cherenkov cone at e^{-1} in the lunar regolith [78],

$$\Delta_0 = 0.05\left[\frac{\mathrm{GHz}}{\nu}\right]\left[1 + 0.075\log\left(\frac{E_s}{10^{19}\mathrm{eV}}\right)\right]^{-1} \ . \tag{5.25}$$

The three terms in the aperture expression Ψ_{ds}, Ψ_{dr}, and Ψ_u denote the angular aperture fractions for downward neutrinos on a smooth surface, downward neutrinos on a rough surface, and upward neutrinos, respectively.

$$\begin{aligned} \Psi_{ds} &= f_0 \Delta_0 \ , \\ \Psi_{dr} &= \frac{16}{3\pi^{3/2}}\sigma_0 \ = \ 0.96\sqrt{2}\tan^{-1}(0.14\nu^{0.22}) \ , \\ \Psi_u &= \frac{16}{3}\left(\frac{\lambda}{2R}\right) \ = \ \frac{16}{3}\left(\frac{L_\nu}{2R\kappa}\right) \ . \end{aligned} \tag{5.26}$$

These expressions were derived in Ref. [48] in the approximation that the neutrino interactions occur near the surface of the Moon and the angle of the Cherenkov cone is small.

For the upward effective aperture, the factor Ψ_u represents the reduced effective solid angle due to neutrino attenuation in the Moon. We rewrite it more generally using the expression derived in the previous section,

$$\Psi_u \ = \ \frac{16}{3}\frac{\Omega_{eff}^{iso}}{2\pi} \ = \ \frac{16}{3}\frac{\lambda}{2R}(1 - e^{-2R/\lambda}) \ . \tag{5.27}$$

So, the effective aperture for upward neutrino is modified according to the neutrino nucleon cross section or incident neutrino energy. If the cross section is small, i.e., the interaction length is large relative to $2R$, the exponential term should be considered. Thus we replace Ψ_u in eq. 5.26 by eq. 5.27 and evaluate the more general event rate.

The downward neutrino aperture has two components according to surface roughness. One component appears even without surface features. The surface roughness effect enhances the amount of the signal come out from the surface. The roughness parameter σ_0 depends on the radio frequency ν with the relation of $\sigma_0 = \sqrt{2}\tan^{-1}(0.14(\frac{\nu}{\mathrm{GHz}})^{0.22})$ [89]. In this thesis, we pick two frequencies, $\nu = 150$ MHz and $\nu = 1.5$ GHz, that span the radio frequency range. For these frequencies, σ_0 is 0.13 rad and 0.21 rad, respectively.

The effective aperture depends on the frequency, ν, and the minimum detectable electric field ε_{min}. In Fig. 5.7, we show the effective aperture for $\varepsilon_{min} = 10^{-8}$ V/m/MHz, with $\nu = 150$ MHz (a) and $\nu = 1.5$ GHz (b). For $\nu = 150$ MHz, downward neutrinos in the smooth surface contributes the most to the total aperture, while for $\nu = 1.5$ GHz, surface roughness effect for downward neutrinos dominates. The similar figures are shown in Ref. [48]. For $\varepsilon_{min} = 10^{-8}$ V/m/MHz, the minimum neutrino energy that can be probed is a few times of 10^{11} GeV. In order to examine the signal for the energy of $E_\nu \sim 10^8 - 10^9$ GeV, we consider the lower ε_{min}, which is $\varepsilon_{min} = 10^{-11}$ V/m/MHz.

In Fig. 5.8, the effective aperture for $\varepsilon_{min} = 10^{-11}$ V/m/MHz is shown for two different frequencies as in Fig. 5.7. The minimum detectable electric field ε_{min} determines the minimum neutrino energy that can be examined. The lower ε_{min} allows a probe of a lower neutrino energy. Like the Fig. 5.7, for the higher frequency, $\nu = 1.5$ GHz, the downward signals that emerge from the smooth surface approximation (ds) are smaller than the downward signals enhanced by surface roughness.

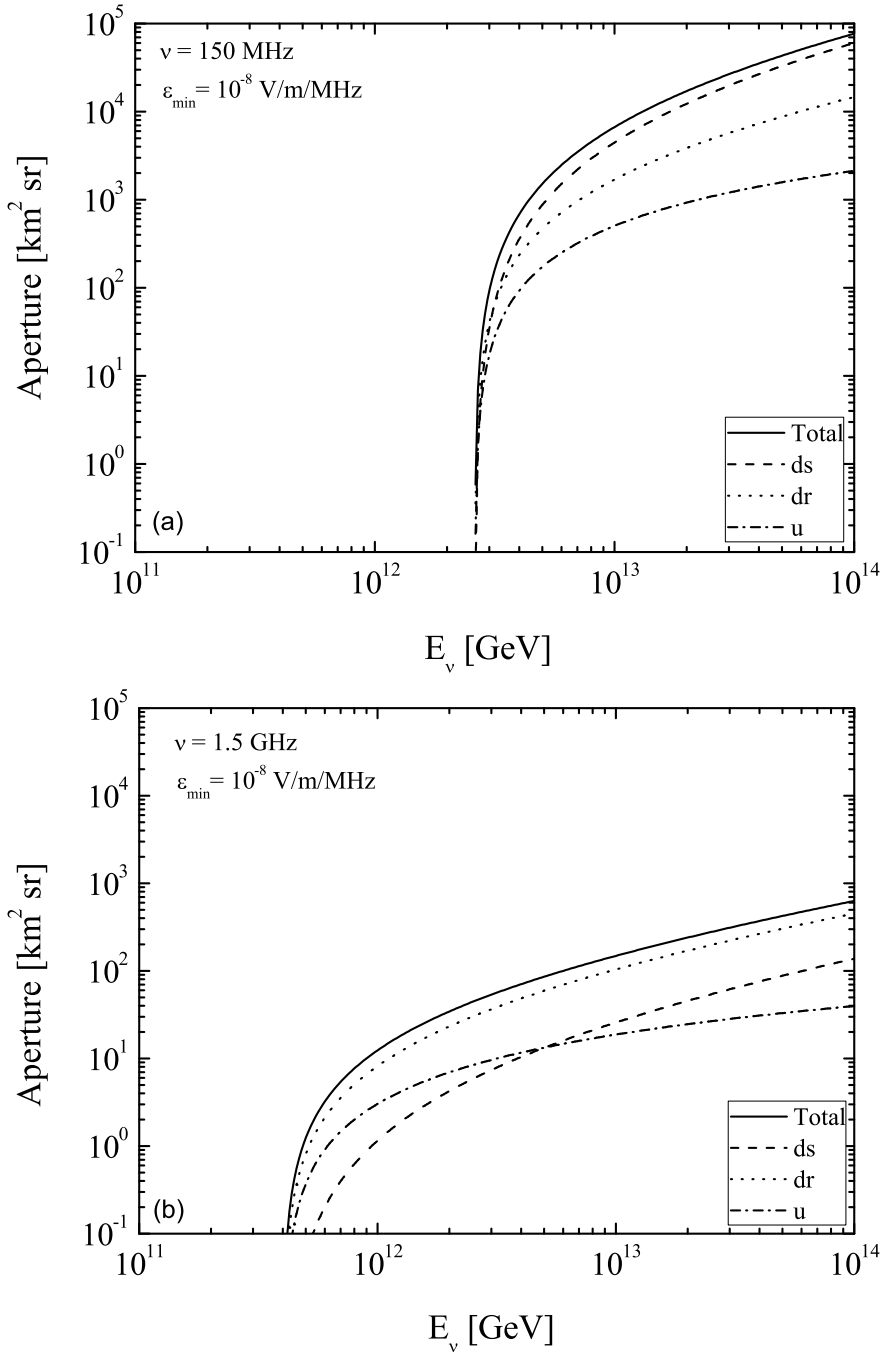

Figure 5.7: The effective aperture for neutrinos as a function of incident neutrino energy for $\varepsilon_{min} = 10^{-8}$ V/m/MHz. The solid lines represent the total of the downward smooth (ds, dashed), the downward rough (dr, dotted) and the upward(u, dot-dashed) contributions. (a) is for $\nu = 150$ MHz and (b) is for $\nu = 1.5$ GHz.

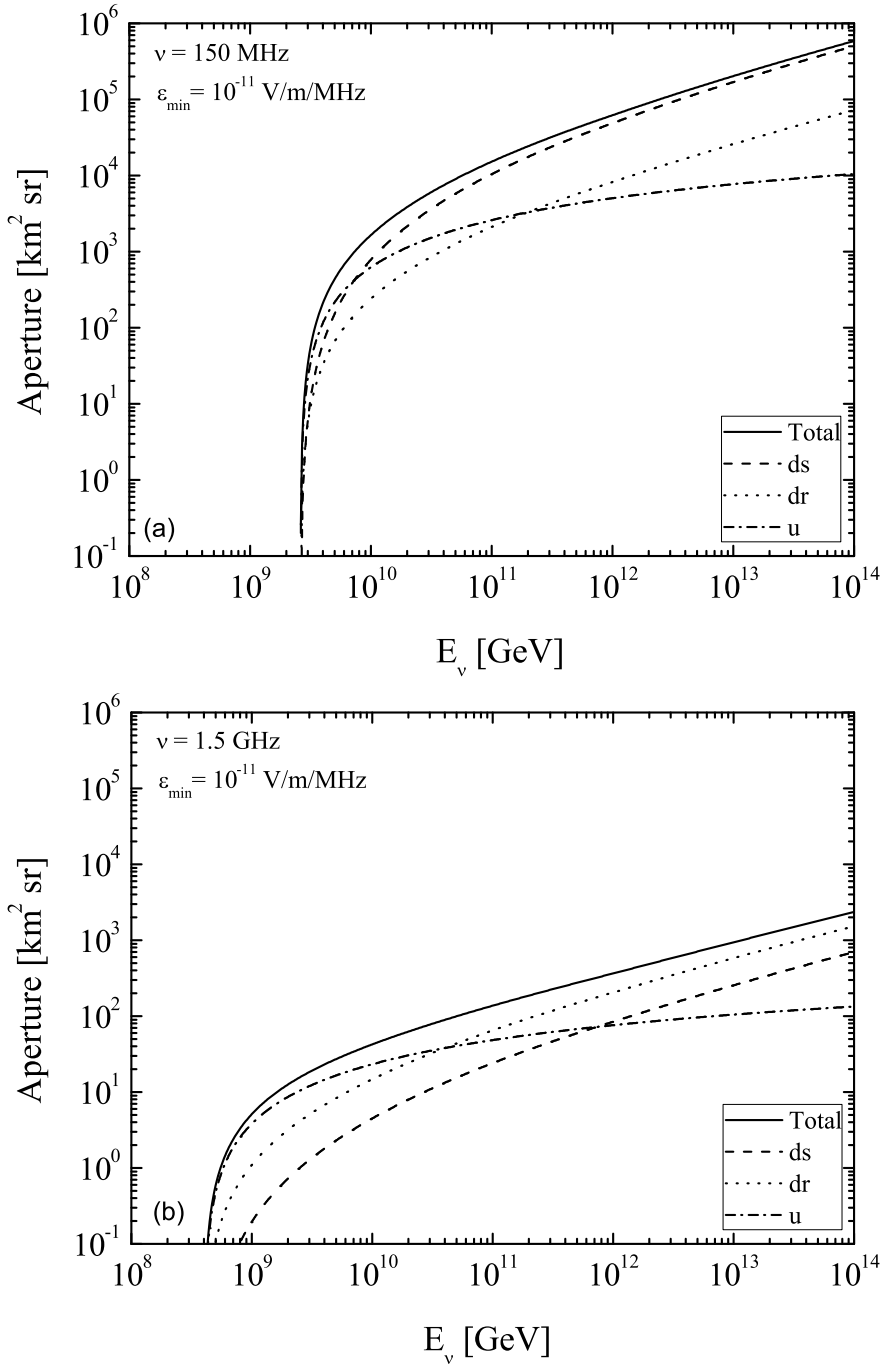

Figure 5.8: The effective aperture for neutrinos as a function of incident neutrino energy for $\varepsilon_{min} = 10^{-11}$ V/m/MHz. The solid lines represent the total of the downward smooth (ds, dashed), the downward rough (dr, dotted) and the upward(u, dot-dashed) contributions. (a) is for $\nu = 150$ MHz and (b) is for $\nu = 1.5$ GHz.

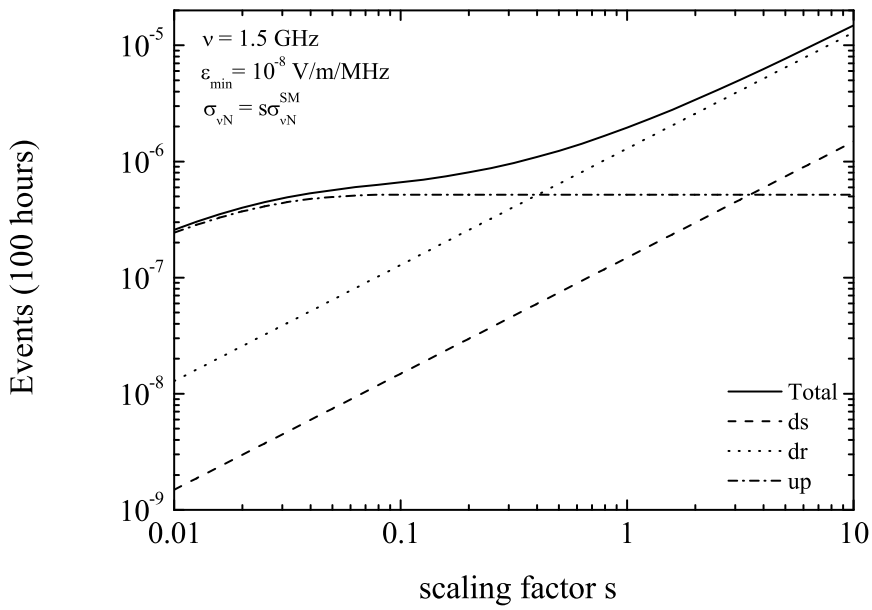

Figure 5.9: The event number of neutrinos as function of scaling factor s for neutrino-nucleon cross section. These are evaluated for $\nu = 1.5$ GHz and $\varepsilon_{min} = 10^{-8}$ V/m/MHz the high cosmogenic neutrino flux from Fig. 5.1. The event number of each piece is indicated with total event number as in previous figures.

To see the cross section dependence of the event rate and the interplay of different contributions, we scaled the standard model cross section, $\sigma_{\nu N}^{SM}$ to $\sigma_{\nu N}$ with scaling factor s,

$$\sigma_{\nu N} = s\sigma_{\nu N}^{SM} \ . \tag{5.28}$$

In Fig. 5.9 and Fig. 5.10, the event numbers are shown with the scaling factor of the standard model neutrino-nucleon cross section for two different electric field thresholds $\varepsilon_{min} = 10^{-8}$ V/m/MHz and $\varepsilon_{min} = 10^{-11}$ V/m/MHz . We use $\nu = 1.5$ GHz for frequency and 100 hours for observing time. For $\varepsilon_{min} = 10^{-8}$ V/m/MHz, we show the results for only high cosmogenic neutrino flux in Fig. 5.1, while for $\varepsilon_{min} = 10^{-11}$ V/m/MHz, the results for two fluxes named 'high' and 'low' are presented with red and blue lines, respectively. We also indicate the contributions from the separate pieces of the effective aperture. As in the previous figures, the contributions of downward neutrinos for the smooth surface (ds) is presented with the dashed

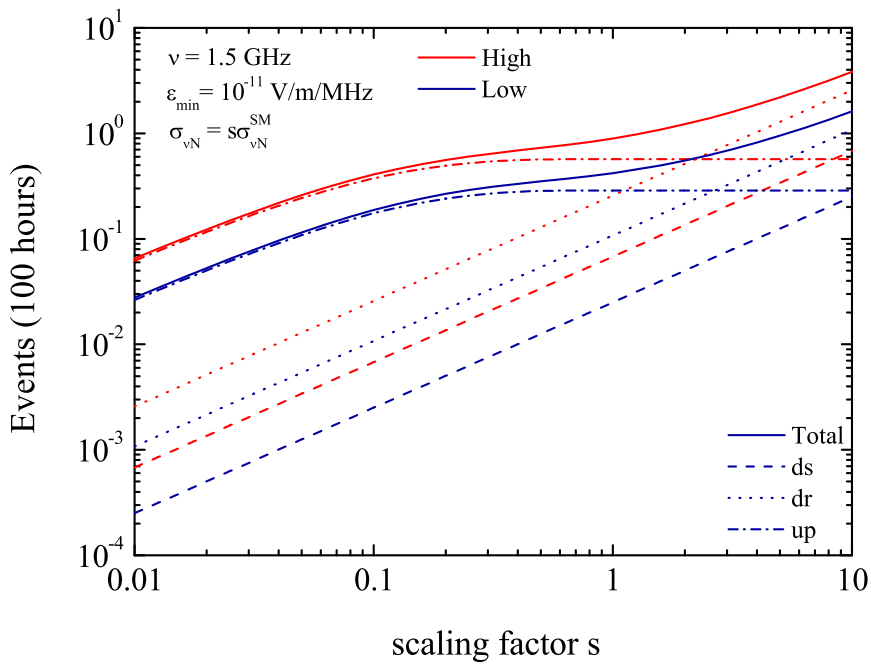

Figure 5.10: The event number of neutrinos as function of scaling factor s as Fig 5.9. These are for $\nu = 1.5$ GHz and $\varepsilon_{min} = 10^{-11}$ V/m/MHz with the high cosmogenic neutrino flux (red) and the low cosmogenic neutrino flux (blue) from Fig. 5.1.

lines, those for the rough surface (dr) with the dotted lines, and the upward neutrino contributions (up) with the dash-dotted lines.

As shown in Eq. 5.26, the upward effective solid angle is proportional to the neutrino interaction length where the cross section is large. Thus, according to Eq. 5.19, the effective aperture of upward neutrino is independent of the neutrino cross section, and eventually the upward event rate also has no cross section dependence as long as the neutrino cross section is large enough. This is shown by the flattened dot-dashed lines in figures 5.9 and 5.10 However, the downward parts are linearly dependent on the cross section. Above a certain value of s, for example, $s \sim 0.4$ for $\varepsilon_{min} = 10^{-8}$ V/m/MHz and $s \sim 2$ for $\varepsilon_{min} = 10^{-11}$ V/m/MHz, downward neutrinos dominate the total event rate. For the low cross sections, the upward event rate is also changed because Ω^{iso}_{eff} depends on the neutrino cross section.

In Fig. 5.11, we show the frequency dependence of the event rate for the several

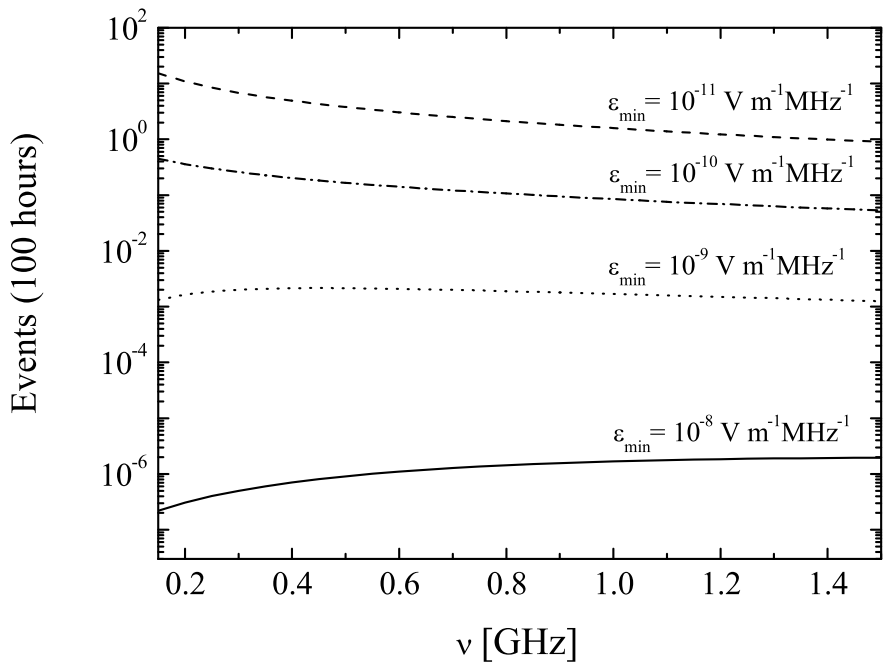

Figure 5.11: The number of events as a function of radio frequency with the high flux of neutrinos for $\varepsilon_{min} = 10^{-11} - 10^{-8}$ V/m/MHz.

different minimum detectable electric fields, $\varepsilon_{min} = 10^{-11} - 10^{-8}$ V/m/MHz. The standard model neutrino cross section and 'high' cosmogenic neutrino flux are used in evaluating the number of events for 100 hours of observation. From the figure, one can see that the electric field threshold for detection should be higher than $\varepsilon_{min} = 10^{-10}$ V/m/MHz in order to detect at least one event in 100 hours.

5.4 The Cherenkov Signals from Cosmic Rays

As shown in the previous section, the high energy neutrino event rate has downward neutrinos as its main contribution. Although upward neutrino contributions dominate for some frequency and energies, at extremely high energies ($E_\nu > 10^{12}$ GeV), downward neutrinos are the most contributing elements. Not only neutrinos but also cosmic rays interact with the lunar regolith and produce radio Cherenkov signals. Here, we assume that cosmic rays consist of mostly protons. The signals detected at Earth are the combined signals induced by downward neutrinos with the

ones induced by downward cosmic rays. Thus, we need to characterize the signals by cosmic rays in order to distinguish the neutrino signals. In this section, we investigate the radio Cherenkov signals from downward cosmic rays.

First of all, the cosmic ray flux used in our calculation is shown in Fig. 5.1 along with the neutrino fluxes. This cosmic ray flux is taken from Ref. [53] and extended up to the energy of 10^{14} GeV. One of the inputs to the effective aperture is the shower energy. For the hadronic shower energy E_s, we use $E_s = 0.2E_{CR}$ as for the neutrino case.

The interaction length of cosmic rays is very short compared to the neutrino interaction length. In the energy range we consider, $10^8 - 10^{14}$ GeV, the smallest neutrino interaction length for standard model interaction is a few tens of 10^6 cmwe. However, the cosmic ray interaction is about 44 cmwe. Due to this short interaction length, attenuation occurs for even the downward cosmic ray flux, and there is no upward flux for cosmic rays. Thus, the effective aperture formula in Ref. [48] needs to be modified for cosmic rays to reflect the attenuation effect for downward particles.

We denote the effective aperture for cosmic rays by

$$A_{CR}(E) = A_{ds} + A_{dr} = A_0 P_{CR}(E) \ , \tag{5.29}$$

where $A_0 = 4\pi^2 R_M^2$ as indicated in the previous section. In order to evaluate $P_{CR}(E)$, we start with the eq. (12) in Ref. [48] ,

$$\begin{aligned} P_{CR}(E) &= \frac{1}{\pi}\frac{L_\gamma}{L_{CR}} \int_{-\infty}^{0} d\alpha \cos\alpha \int_{-\infty}^{\infty} d\Delta \sin(\theta_c + \Delta) \int_0^\infty d\phi \\ &\times \int_0^\infty dz \ e^{-\tau_{CR}} \mathcal{H}_R \mathcal{H}_D \xi \ , \end{aligned} \tag{5.30}$$

with the negative incident angle α and the cosmic ray interaction length L_{CR}. The variable Δ is the polar angle of the interior ray measured relative to the Cherenkov angle θ_c, ϕ is the azimuthal angle. The quantity z is defined as $z \equiv h/L_\gamma$, where h is the depth from the surface to the interaction point in the lunar regolith. The Heaviside step function $\mathcal{H}_R$ is to select the outgoing rays which do not totally internally reflect,

and $\mathcal{H}_D$ is to select the rays bright enough to detect. The factor ξ is the magnification factor related with refraction for the emerging rays. The function τ_{CR} is included by the ratio of the downward attenuation over distance $h/|\sin\alpha|$ to the cosmic ray interaction length,

$$\tau_{CR} = \frac{h}{|\sin\alpha| \; L_{CR}} \; . \tag{5.31}$$

The result of the evaluation of the probability for cosmic rays is obtained as

$$P_{CR}(E) = \frac{\sqrt{n_r^2 - 1}}{8} f_0 \Delta_0 \left(\frac{2}{3} f_0^2 \Delta_0^2 + \frac{1}{2} \sigma_0 \right) \; . \tag{5.32}$$

The first term in parenthesis is from the contribution of the smooth surface and the second term from the contribution of surface roughness. As one can see from eq. 5.32, the probability for cosmic rays to produce a signal is independent of the cosmic ray cross section. More details of the derivation of eq. 5.32 are presented in Appendix B.

In Fig. 5.12, we show the effective aperture for cosmic rays for $\varepsilon_{\rm min} = 10^{-8}$ V/m/MHz with $\nu = 0.15$ and 1.5 GHz. The effective aperture for cosmic rays for $\varepsilon_{\rm min} = 10^{-11}$ V/m/MHz is shown for two frequencies in Fig. 5.13. As for the neutrino effective aperture, at lower frequency, the smooth surface contribution dominates, and at higher frequency, the largest contribution is from the rough surface effect. In addition, the combination of the detection parameters, frequency and electric field sensitivity, determines the minimum energy that can be probed.

In Fig. 5.14, the event numbers evaluated with the effective aperture in Fig. 5.12 and Fig. 5.13 are presented as a function of frequency. These are plotted for $\varepsilon_{\rm min} = 10^{-8} - 10^{-11}$ V/m/MHz with blue-dashed lines. We also show the event rate of neutrinos with red-solid lines for comparison. For all frequencies and electric field thresholds, the event rates due to the cosmic ray signal surpass the ones due to neutrino signal with the standard model cross sections and the high cosmogenic neutrino flux in Fig. 5.1.

The event rate can be raised by either the increased flux or the increased cross

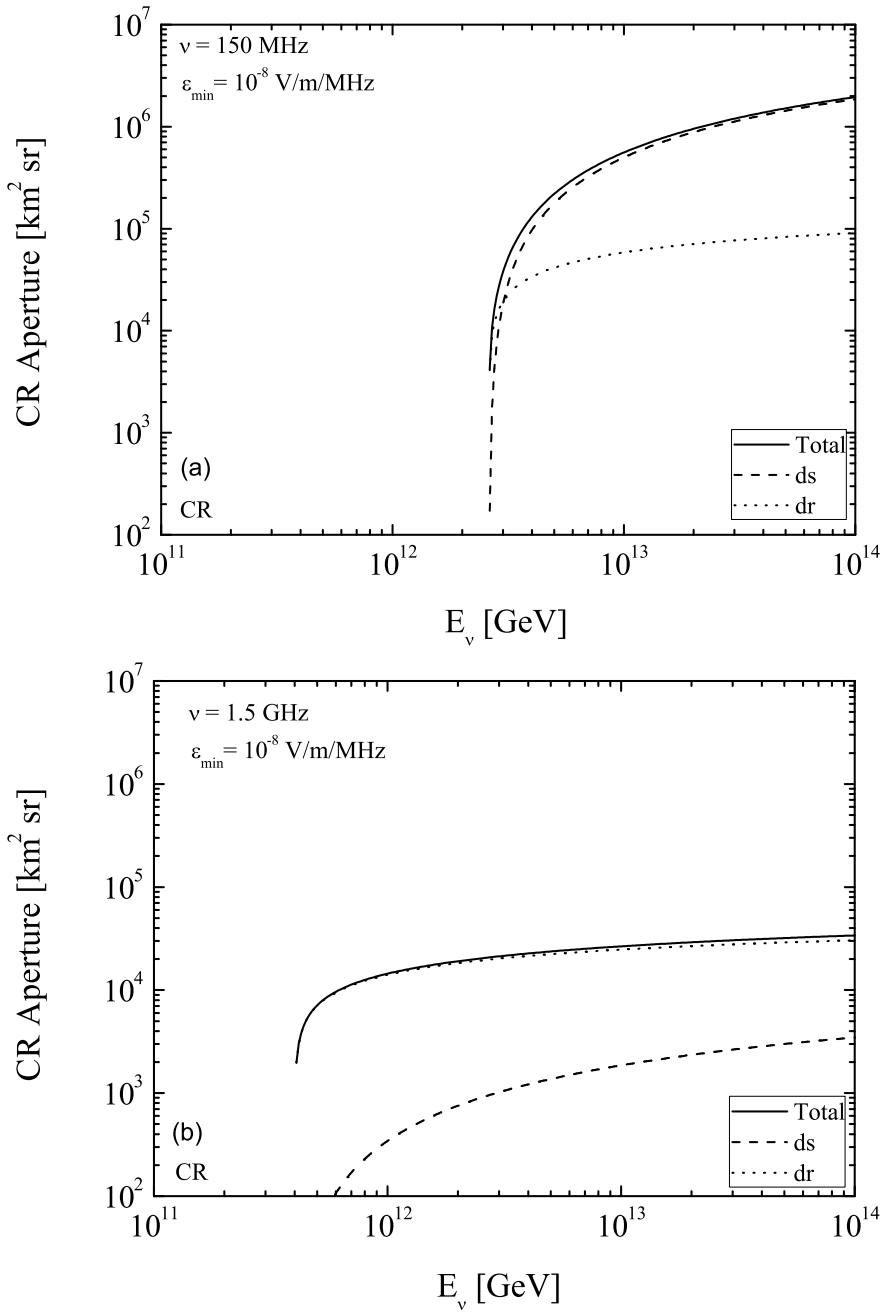

Figure 5.12: The effective aperture for cosmic rays as a function of cosmic ray energy for $\varepsilon_{min} = 10^{-8}$ V/m/MHz. The solid lines represent the total of the downward smooth (ds, dashed) and the downward rough (dr, dotted). (a) is for $\nu = 150$ MHz and (b) is for $\nu = 1.5$ GHz.

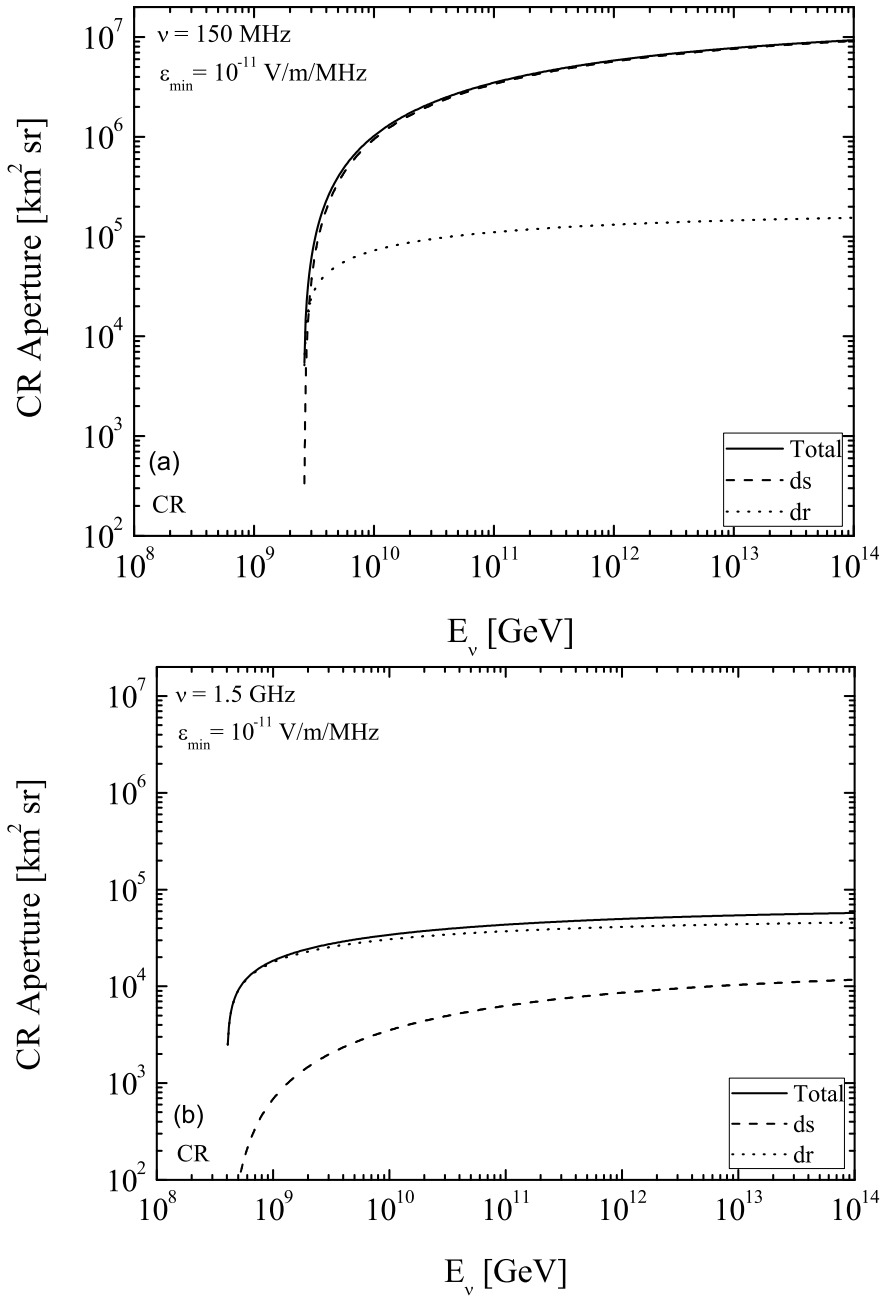

Figure 5.13: The effective aperture for cosmic rays as a function of cosmic ray energy for $\varepsilon_{min} = 10^{-11}$ V/m/MHz. The solid lines represent the total of the downward smooth (ds, dashed) and the downward rough (dr, dotted). (a) is for $\nu = 150$ MHz and (b) is for $\nu = 1.5$ GHz.

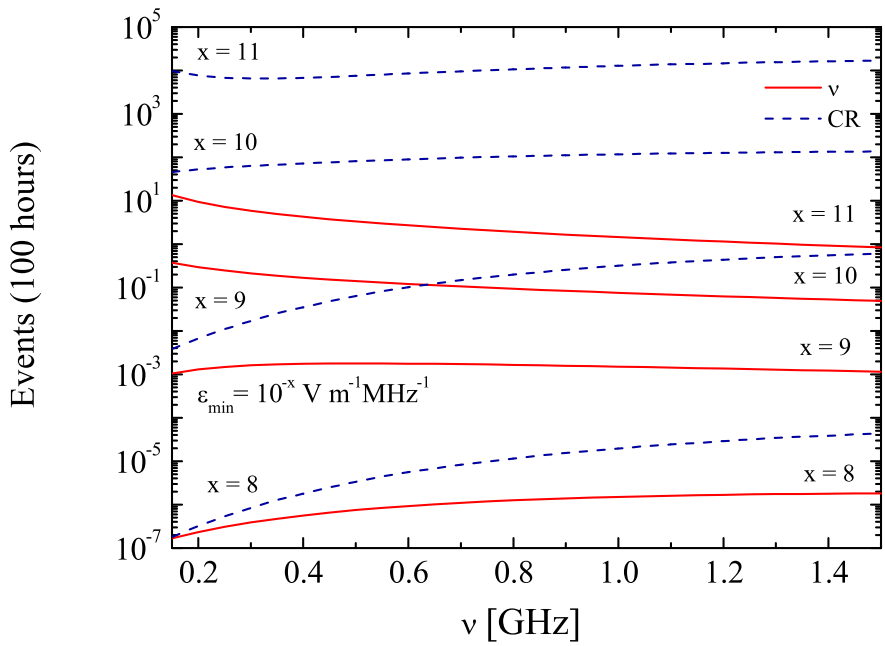

Figure 5.14: The number of events as a function of radio frequency with the high neutrino flux (red, solid) and with cosmic rays (blue, dashed) for $\varepsilon_{min} = 10^{-11} - 10^{-8}$ V/m/MHz.

section. At lower energies than we explored here, the neutrino flux is larger, but cosmic ray flux is even larger than the neutrino flux at the corresponding energy. Thus, we conclude the neutrino induced Cherenkov signals by the standard model interaction cannot exceed the cosmic ray induced signals. In the next section, we examine the consequences of neutrino-nucleon cross sections enhanced by non-standard model interactions.

5.5 Radio Cherenkov Signals with Enhanced Neutrino Cross Sections

As mentioned in the previous section, the neutrino event rates could be higher than the cosmic ray event rates by assuming a higher neutrino flux or a larger cross section. In this section, we explore the possibility for the neutrino induced signals to overcome the cosmic ray induced signals with the enhanced neutrino-nucleon cross sections by the non-standard model interaction. For the enhanced cross sections, we

take the neutrino-nucleon cross sections for mini-black hole production.

Black holes could be produced at the collider when D-dimensional Planck scale in the extra-dimensional models (EDMs) M_D is low enough to be a few TeV. The EDMs [79, 80, 81, 82, 83] are motivated to solve the hierarchy problem, which is the large difference in energy scale between the electroweak force and the quantum gravity. In four dimensions, fundamental Planck scale M_P is about 1.22×10^{19} GeV, while the electroweak scale m_{EW} is a few hundred GeV [84, 87]. In the extra dimensional models, M_P is reduced to M_D of order of TeV. The fundamental Planck scale M_P is related to the D-dimensional Planck scale M_D as [79]

$$M_P^2 \sim M_D^{2+n} R^n \ , \tag{5.33}$$

where the radius of n extra dimensions is

$$R \sim 10^{\frac{30}{n}-17} \text{ cm} \times \left(\frac{1 \text{ TeV}}{m_{\text{EW}}}\right)^{1+\frac{2}{n}} \ . \tag{5.34}$$

If the center of mass energy in the particle collision is higher than the Planck scale, $\hat{s} \gg M_D^2$, and impact parameter is smaller than the Schwarzschild radius, a mini-black hole is created from neutrino interactions with partons [85, 86].

The cross section for the neutrino interaction with parton is given by

$$\sigma^{BH}(\nu i \to \text{BH}) = \pi r_s^2(\sqrt{\hat{s}}) \ , \tag{5.35}$$

where the center of mass energy $\sqrt{\hat{s}} = M_{\text{BH}}$, and the Schwarzschild radius for a $(4+n)$-dimensions is

$$r_s = \frac{1}{M_D}\left[\frac{M_{\text{BH}}}{M_D}\left(\frac{2^n \pi^{\frac{n-3}{2}} \Gamma(\frac{3+n}{2})}{2+n}\right)\right]^{\frac{1}{1+n}} \ . \tag{5.36}$$

Then, the neutrino-nucleon cross section for black hole production is given by

$$\sigma(\nu N \to \text{BH}) = \sum_i \int_{(M_{\text{BH}}^{\text{min}})^2/s}^{1} dx \ \hat{\sigma}_i^{\text{BH}}(xs) f_i(x, Q^2) \ , \tag{5.37}$$

where $M_{\text{BH}}^{\text{min}}$ is the minimum black hole mass,

$$M_{\text{BH}}^{\text{min}} = x_{\text{min}} M_D \ . \tag{5.38}$$

The quantity s is the center of mass energy squared $s = 2m_N E_\nu$ and $f_i(x, Q^2)$ is the parton distribution function for parton flavor i. For our calculations, we use the black hole cross sections evaluated by Connolly, Thorne, and Waters [87] and Feng [88].

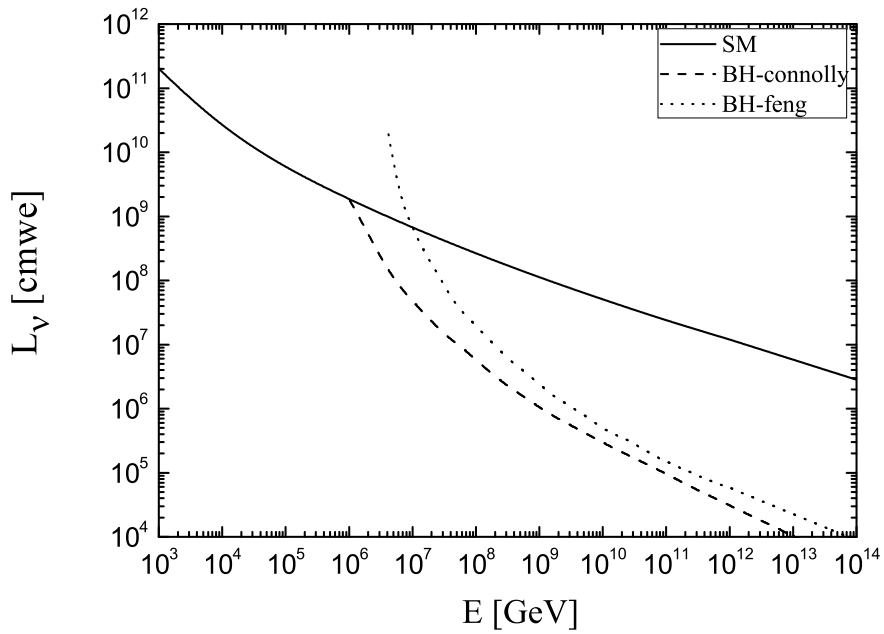

Figure 5.15: The neutrino interaction length (in centimeters water equivalent distance) as a function of energy with the non-standard model neutrino-nucleon cross section for mini-black hole production for $n = 7$ and $M_D = 1$ TeV. The cross sections for black hole are taken from Connolly, Thorne, and Waters [87] (dashed) and Feng [88] (dotted), respectively. The interaction length with the standard model cross section is indicated with the solid line.

First of all, the interaction lengths calculated with the non-standard model cross sections are shown in Fig. 5.15. We also show the interaction length with the standard model cross section for reference. The dashed line indicates the interaction length calulated by Connolly et al. [87], and the dotted line is by Feng [88]. Both values are calculated for $n = 7$ and $M_D = 1$ TeV. As shown in the figure, the mini-black hole contributed cross sections lower the neutrino interaction length.

The black hole contributed neutrino interaction lengths are decreased to less than 10^4 cmwe at some extremely high energies. With this scale of interaction length,

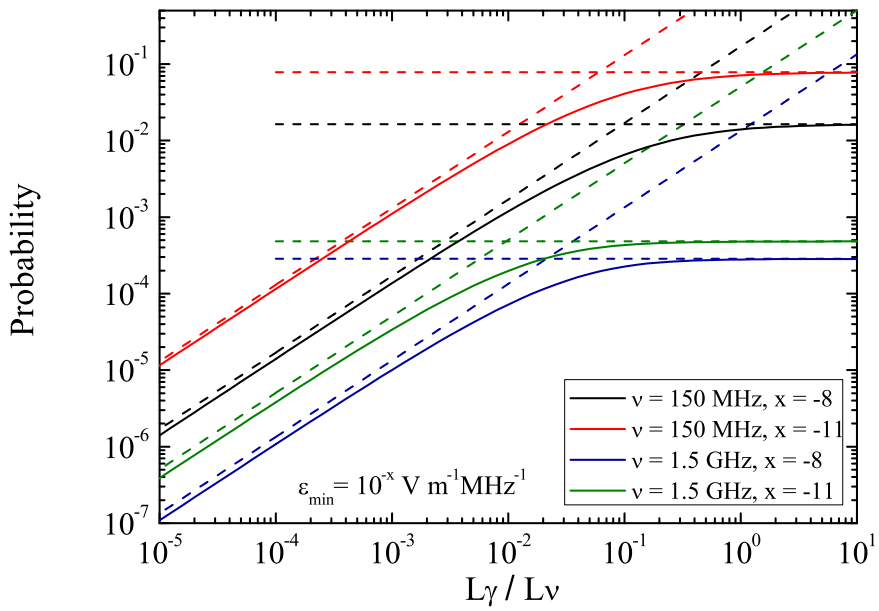

Figure 5.16: The probability as a function of the ratio of the photon interaction length to the neutrino interaction length. It is evaluated numerically for a minimum detectable field of $\varepsilon_{min} = 10^{-8}$ V/m/MHz and $\varepsilon_{min} = 10^{-11}$ V/m/MHz, and for the frequency of $\nu = 150$ MHz and $\nu = 1.5$ GHz. Numerical result is shown as the solid lines and analytical ones are indicated with the dashed lines for neutrinos and cosmic rays.

we cannot approximate L_γ/L_ν as either the neutrino limit (no attenuation over scale L_γ) or the cosmic ray limit (large attenuation over scale L_γ) in evaluating the effective aperture. We calculated the probability in the small angle limit without the approximations of the "cosmic ray" or "neutrino" limit, using the equation as below,

$$\begin{aligned} P_{\rm num}(E) &= \frac{\sqrt{n_r^2-1}}{\pi^{3/2}} f_0 \Delta_0 \int_0^{\pi/2} d\phi' \left[\int_{\omega_0}^{\infty} d\omega e^{-\omega^2} \int_{-1}^{1} du \right. \\ &+ \left. \int_{-\omega_0}^{\omega_0} d\omega e^{-\omega^2} \int_{-\frac{\omega}{\omega_0}}^{1} du \right] \int_{\alpha_{min}}^{0} d\alpha \, |\alpha| \left(1 - e^{-\frac{L_\gamma \; z_{max}}{L_\nu |\alpha|}} \right) , \end{aligned} \tag{5.39}$$

where

$$z_{\rm max} = \frac{\sqrt{n_r^2-1}}{n_r} f_0^2 \left(1 - u^2 \right) , \tag{5.40}$$

$$\alpha_{\rm min} = -f_0 \Delta_0 (u + \omega x \cos\phi') , \tag{5.41}$$

$$u = \frac{\Delta}{f_0 \Delta_0} . \tag{5.42}$$

Here, ω is the scale factor of surface tilt polar angle $\sigma = \sigma_0\omega$, and ϕ' is the azimuthal angle of tilt.

In Fig. 5.16, we show the numerically evaluated probability. We use this numerical probability in evaluating the event rate with the mini-black hole produced neutrino cross sections. We show this as a function of ratio between the interaction lengths, L_γ/L_ν, with the solid lines. The dashed lines indicate the analytic probabilities for the "neutrino limit" where $L_\nu \gg L_\gamma$ (Eq. B.22), and for the "cosmic limit" where $L_\nu \ll L_\gamma$ (Eq. 5.32). In the neutrino limit, the differences between the numerical and the analytic probabilities for each combination of detection parameters have the range from 12% to 25%. These values agree with Ref. [48].

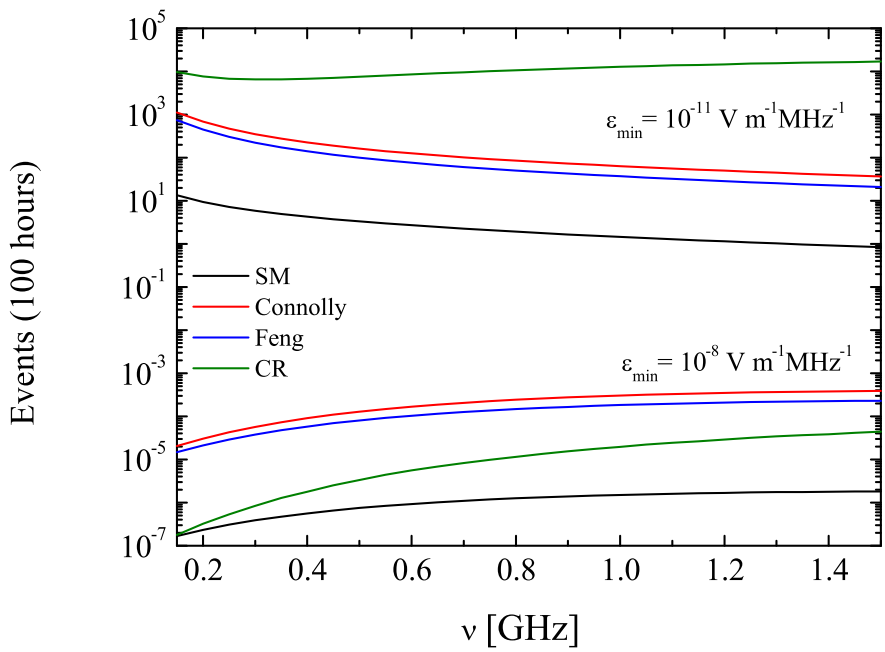

Figure 5.17: The event number as a function of radio frequency for $\varepsilon_{min} = 10^{-11}$ and $\varepsilon_{min} = 10^{-8}$ V/m/MHz. The results with the neutrino cross section for black hole production are shown as the red (Connolly [87]) and blue (Feng [88]) lines, while the one with the standard model cross section is shown as black line. Green line indicates the event number from cosmic ray flux.

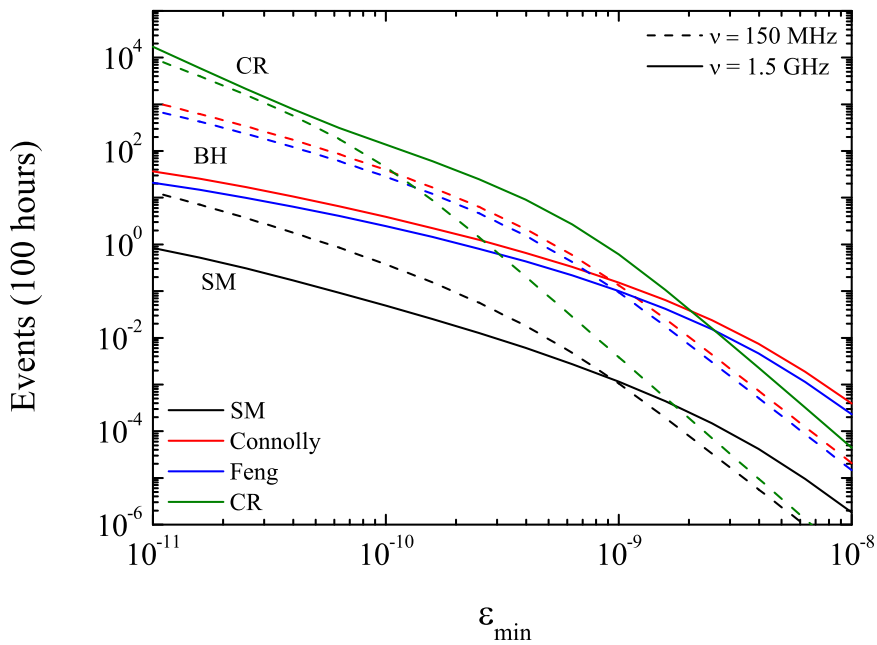

Figure 5.18: The event number as a minimum detectable field ε_{min} for $\nu = 150$ MHz (dashed) and $\nu = 1.5$ GHz (solid). The color of each line indicates the same as Fig. 5.17.

With the numerically evaluated probability as a part of the aperture, we evaluate event rates with the enhanced neutrino-nucleon cross section for mini-black hole production with 100 hours of observing time. Fig. 5.17 shows the frequency dependence of the event rates for the two minimum electric field $\varepsilon_{\rm min} = 10^{-8}$ V/m/MHz, and $\varepsilon_{\rm min} = 10^{-8}$ V/m/MHz. The results with the black hole neutrino cross section are shown as the red (CTW [87]) and blue (Feng [88]) lines, while the results with the standard model cross section are shown as black lines. Green lines indicate the event number from the cosmic ray flux. The event rates do not change very much according to the frequency. For the electric field threshold, the events with the enhanced neutrino cross section exceed the cosmic ray events at $\varepsilon_{\rm min} = 10^{-8}$ V/m/MHz. But for $\varepsilon_{\rm min} = 10^{-11}$ V/m/MHz, the event rate for cosmic rays still overwhelm the neutrino event rates, so this $\varepsilon_{\rm min}$ is not favorable to detect neutrinos.

Finally, in the figure 5.18, we show the event rates for two frequencies, $\nu = 150$

MHz (dashed) and $\nu = 1.5$ GHz (solid), as a function of the minimum electric field, $\varepsilon_{\rm min}$. The color labels indicate the same as in Fig. 5.17. For $\nu = 1.5$ GHz, the neutrino induced signals by black hole contributions exceed the cosmic ray induced signals for $\varepsilon_{\rm min} > 2 \times 10^{-9}$ V/m/MHz. For $\nu = 150$ MHz, the neutrino induced BH signals are larger than the cosmic ray induced Cherenkov signal for $\epsilon_{\rm min} > 10^{-10}$ V/m/MHz.

It appears that $\nu = 150\,$MHz is better choice than 1.5 GHz to see the signals with the enhanced cross sections, as long as the detection threshold $\varepsilon_{\rm min} \sim 10^{-10}\,$V/m/MHz. The enhanced cross section for the mini-black hole production compensates for the neutrino flux lower than cosmic ray flux at lower energies, and enable to obtain more than one event. However, the current RESUN capability of the detection threshold is $\varepsilon_{\rm min} \sim 10^{-8}\,$V/m/MHz [17]. The threshold of LUNASKA [15], another experiment for UHE neutrino search, is also a few of $10^{-8}\,$V/m/MHz.

CHAPTER 6
CONCLUSION

We have studied the neutrino charged current interaction with isoscalar nucleons at high energies for muon neutrinos and at low energies for tau neutrinos. In the considered energy ranges, the total cross sections are dominated by deep inelastic scattering (DIS). Therefore, we evaluated the neutrino nucleon DIS charged current cross sections with heavy quark and lepton masses including the quantum chromodynamics (QCD) corrections at next-to-leading order (NLO).

With the case of muon neutrino-nucleon interactions, we investigated the effect of the heavy quarks in the cross sections for two different flavor number schemes to include the heavy quarks, VFNS and FFNS. The muon mass is very small relative to the energy of 100 GeV or higher, so the muon mass corrections are not considered. The cross sections are evaluated with the PDF sets of CTEQ6.6M and GJR which is divided into GJRV and GJRF.

For both CTEQ6.6M and GJR PDFs, the ratio of the NLO cross section to the LO cross section with the VFNS matches with the $\overline{\text{MS}}$ result, while the ratio with the FFNS has some deviation. At the energies below $E_\nu \sim 10^6$ GeV, the cross sections with the VFNS and FFNS evaluated using the GJR PDFs are almost the same, so their ratio is close to 1. But,the ratio of the two cross sections is reduced at higher energies, and has about 13 % discrepancy at 10^{12} GeV. This indicate the cross sections with the FFNS for three flavors are overestimated at the high energies. Thus we conclude that the VFNS is more appropriate to evaluate the cross section at high energies.

For the VFNS, we need to use the VFNS version of PDF as well. The CTEQ6.6M set is fit including heavy quarks and their mass effects, while the GJRV PDF is not. The heavy quark constituents in the GJRV PDF are generated radiatively from the

three flavor fit. So, the CTEQ6.6M PDF is more reliable at high energies, where there are the heavy quark contributions.

For tau neutrino interactions, we evaluated the tau neutrino and antineutrino charged current cross sections for DIS interaction with isoscalar nucleon to update the earlier work [43]. The energy range considered is 10 GeV to 10 TeV. At some low energies, tau mass corrections on the cross sections are significant. But as the energy increases, the tau mass effect is reduced, and at the very high energies the tau neutrino cross sections are almost the same as the ones for muon neutrinos.

We have evaluated the uncertainties of factorization scale, cutoff scales for the low-Q extrapolated structure functions, and PDF choices are considered. The uncertainty of flavor schemes to include the charm quark contribution is also examined. Considering all of these uncertainties, we estimated the theoretical errors of DIS charged current cross sections shown in Fig. 4.4. At 10 GeV, the errors from the factorization scale in the structure functions are largest, while at 10 TeV, the PDF choice have the largest effect in the cross section. The flavor schemes for charm quark is the most important element at 100 GeV.

The tau neutrino and antineutrino cross sections have measured by the DONuT Collaboration [90]. The average cross sections at 115 GeV is

$$\sigma^{avg}/E = 0.39 \pm 0.13 \pm 0.13 \times 10^{-38}\ \mathrm{cm}^2/\mathrm{GeV}\ .$$

The first error is statistical, and the second error is systematic. Our evaluation at 115 GeV with $W_{min} = 1.4$ GeV is

$$\sigma^{avg}/E = 0.37 \times 10^{-38}\ \mathrm{cm}^2/\mathrm{GeV}\ ,$$

which agrees well with the DONuT measurement.

With the cross sections evaluated above, we investigated the radio Cherenkov signals of neutrinos from the Moon. We considered the energy range of $10^8 - 10^{14}$ GeV. In these energies, the cross sections are almost the same for all flavors.

We evaluated the neutrino induced event rate for 100 hour observation time. Ingredients for calculating the event rates are the flux of the particles and the effective aperture. We used the cosmogenic neutrino flux predicted by Olinto et al. [52]. For the effective aperture, we calculated it using the analytic formula evaluated by Gayley et al. [48] with our standard model neutrino nucleon cross sections.

The calculated event rates are investigated for the frequency and the minimum detectable electric field. For the minimum detectable electric field $\varepsilon_{min} = 10^{-8}$ V/m/MHz, the neutrino event rates are too low to be detected. For at least 1 neutrino event, ε_{min} should be less than $10^{-10} - 10^{-11}$ V/m/MHz with the standard model neutrino nucleon cross sections and the fluxes given by Olinto et al.

Lower ε_{min} allows to detect more particles with low incident energies. But, the cosmic ray particles are also detected as well as neutrinos. We calculated the effective aperture for cosmic rays including the attenuation of the downward particles and evaluate the cosmic ray event rate. The cosmic ray flux is evaluated using the parameterization in Ref. [53]. The signals of cosmic rays are independent of the cross sections. With standard model neutrino nucleon cross sections, the cosmic ray induced signals overwhelm the neutrino induced signals for all detectable electric field thresholds and the frequencies.

Higher neutrino event rates can be obtained than the cosmic ray event rate with the enhanced neutrino-nucleon cross sections. We employed the cross section for mini-black hole production for example in the extension of the standard model. With enhanced non-standard model cross sections, the neutrino event rate exceeds the cosmic ray event rate for $\varepsilon_{min} > 10^{-9}$ V/m/MHz, but it is still less than 1 for $\nu = 1.5\,\mathrm{GHz}$, which is undetectable. For $\nu = 150\,\mathrm{MHz}$, the neutrino events which surpass the cosmic ray event rate require $\varepsilon_{min} \sim 10^{-10}$ V/m/MHz, which is not currently attainable.

Neutrino induced radio Cherenkov event rates depend on neutrino flux and cross section. We have looked at enhanced neutrino cross sections with the cosmogenic incident flux. There may be other astrophysical sources of UHE neutrinos. For further research, we will look at the event rates with new flux $\Phi = \mathcal{N}/E^2$ where $\mathcal{N} = N/E^2$, and compare with the results evaluated with non-standard model cross sections to determine the sensitivity of lunar radio Cherenkov observations.

APPENDIX A
EFFECTIVE INTERACTION LENGTH

In this section, we derive the effective interaction length to include the attenuation and regeneration effect. This shows in more detail the procedure outlined in Ref. [48]. We start with the neutrino flux as a function of column depth X,

$$\frac{d\Phi(E,X(\theta))}{dX} = -\frac{\Phi(E,X(\theta))}{L_\nu} + N_A \int_{E_\nu}^{\infty} dE' \Phi(E',X(\theta)) \frac{d\sigma_{NC}(E',E)}{dE} \ , \quad \text{(A.1)}$$

where

$$\frac{d\sigma_{NC}(E',E)}{dE} \simeq r_{NC}\sigma_{\nu N}^{tot}(E')\delta(E-(1-\langle y\rangle)E') \ . \quad \text{(A.2)}$$

The neutrino inelasticity y is $y = (E'-E)/E'$, and its average value $\langle y\rangle$ is approximately 0.2 at high energies. The quantity r_{NC} means the ratio of the neutral current cross section to the total cross section. Inserting Eq. A.2 into Eq. A.1, we can rewrite the flux as

$$\begin{aligned} \frac{d\Phi(E,X(\theta))}{dX} &= -\frac{\Phi(E,X(\theta))}{L_\nu} \\ &+ N_A \int_{E_\nu}^{\infty} dE' \Phi(E',X(\theta)) r_{NC}\sigma_{\nu N}^{tot}(E')\delta(E-(1-\langle y\rangle)E') \quad \text{(A.3)} \\ &= -\frac{\Phi(E,X(\theta))}{L_\nu} \\ &+ \frac{N_A}{1-\langle y\rangle}\Phi\left(\frac{E}{1-\langle y\rangle}, X(\theta)\right) r_{NC}\sigma_{\nu N}^{tot}\left(\frac{E}{1-\langle y\rangle}\right) \ . \quad \text{(A.4)} \end{aligned}$$

The power law of the flux and the total neutrino cross section is given in terms of the incident neutrino energy as $\Phi(E,X(\theta)) \sim E^{-\gamma}$ and $\sigma_{\nu N}^{tot} \sim E^{\delta}$, respectively. So, $\Phi\big(E/(1-\langle y\rangle), X(\theta)\big)$ and $\sigma_{\nu N}^{tot}\big(E/(1-\langle y\rangle)\big)$ in Eq. A.4 is as below:

$$\begin{aligned} \Phi\left(\frac{E}{1-\langle y\rangle}, X(\theta)\right) &= \left(\frac{E}{1-\langle y\rangle}\right)^{-\gamma} = (1-\langle y\rangle)^{\gamma} E^{-\gamma} \\ &= (1-\langle y\rangle)^{\gamma}\Phi(E,X(\theta)) \ , \quad \text{(A.5)} \end{aligned}$$

$$\sigma_{\nu N}^{tot}\left(\frac{E}{1-\langle y\rangle}\right) = \left(\frac{E}{1-\langle y\rangle}\right)^{\delta} = (1-\langle y\rangle)^{-\delta}E^{\delta}$$
$$= (1-\langle y\rangle)^{-\delta}\sigma_{\nu N}^{tot}(E) \ . \tag{A.6}$$

Then, equation A.4 can be written as

$$\frac{d\Phi(E,X(\theta))}{dX} = -\frac{\Phi(E,X(\theta))}{L_\nu} + N_A(1-\langle y\rangle)^{\gamma-\delta-1}\Phi(E,X(\theta))\sigma_{\nu N}^{tot}(E)r_{NC}$$
$$= -\frac{\Phi(E,X(\theta))}{L_\nu}\big(1-r_{NC}(1-\langle y\rangle)^{\gamma-\delta-1}\big) \ ,$$

where the interaction length $L_\nu = (\sigma_{\nu N}^{tot}(E)r_{NC})^{-1}$.

Defining the κ as $\kappa \equiv -\big(1-r_{NC}(1-\langle y\rangle)^{\gamma-\delta-1}\big)$, the flux in Eq. A.1 is finally reduced to

$$\frac{d\Phi(E,X(\theta))}{dX} = -\kappa\frac{\Phi(E,X(\theta))}{L_\nu} \ . = -\frac{\Phi(E,X(\theta))}{\lambda} \ ,$$

Here, λ is the effective interaction length, defined as

$$\lambda \equiv \frac{L_\nu}{\kappa} = \frac{1}{\sigma_{\nu N}^{eff}N_A} \ , \tag{A.7}$$

where

$$\sigma_{\nu N}^{eff} \equiv \kappa\sigma_{\nu N}^{tot} \ . \tag{A.8}$$

as shown in Eq. 5.10 in section 5.2.

APPENDIX B
EFFECTIVE PROBABILITY FOR COSMIC RAYS AND DOWNWARD NEUTRINOS

The cosmic rays are attenuated by the interaction in the lunar regolith, while there's no attenuation for downward neutrinos. The effective aperture for the downward particles is

$$A_N(E) = A_{ds} + A_{dr} = A_0 P_N(E) \ , \tag{B.9}$$

where $A_0 = 4\pi^2 R_M^2$ and the index N is ν for neutrino, and CR for cosmic rays. Thus, we need to reevaluate the probability for cosmic ray particles. We start with eq. (12) in Ref. [48],

$$\begin{aligned} P_N(E) &= \frac{1}{\pi}\frac{L_\gamma}{L_N}\int_{-\infty}^{0} d\alpha \cos\alpha \int_{-\infty}^{\infty} d\Delta \sin(\theta_c + \Delta) \int_0^\infty d\phi \\ &\times \int_0^\infty dz \ e^{-\tau_N} \mathcal{H}_R \mathcal{H}_D \xi \ , \end{aligned} \tag{B.10}$$

where the incident angle $\alpha < 0$, and τ_N in the attenuation factor is

$$\tau_N = \frac{d}{L_N} = \frac{h}{|\sin\alpha| \ L_N} \ . \tag{B.11}$$

Here, d is the path length of downward incident particles, and h is the depth from the surface to the interaction point. The quantity Δ is the polar angle of the interior ray relative to the Cherenkov angle θ_c. These are indicated in figure B.1.

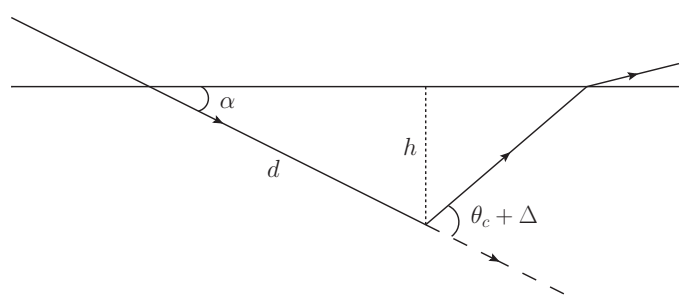

Figure B.1: The passage of the downward particle and the induced signal in the lunar regolith.

Still following Ref. [48], we write the function $\mathcal{H}_R$, the Heaviside step function that accounts for surface roughness, as

$$\mathcal{H}_R = \frac{2}{\pi^{3/2}} \int_0^{\pi/2} d\phi' \int_{-\infty}^{\infty} d\omega e^{-\omega^2} \mathcal{H}_{\omega,\phi'} \tag{B.12}$$

With the definition of $z \equiv h/L_\gamma$ and z_{max},

$$z_{max} \simeq \sin\theta_c f_0^2 \left(1 - \frac{\Delta^2}{f_0^2 \Delta_0^2}\right) , \tag{B.13}$$

the z-integration is,

$$\begin{aligned} \int_0^{\infty} dz\ e^{-\tau_N} &\simeq \int_0^{z_{max}} dz\ e^{-\frac{L_\gamma\ z}{L_N |\sin\alpha|}} \\ &= \frac{L_N\,|\sin\alpha|}{L_\gamma} \left(1 - e^{-\frac{L_\gamma\ z_{max}}{L_N |\sin\alpha|}}\right) \end{aligned} \tag{B.14}$$

Following the notation in Ref. [48],

$$u \equiv \frac{\Delta}{f_0 \Delta_0} , \tag{B.15}$$

$$x \equiv \frac{\sigma_0}{f_0 \Delta_0} . \tag{B.16}$$

After a few steps with the small angle approximation of α and Δ, $P_N(E)$ becomes

$$\begin{aligned} P_N(E) &= \frac{n_r}{\pi^{3/2}} \sin\theta_c f_0 \Delta_0 \int_0^{\pi/2} d\phi' \int_{-\infty}^{\infty} d\omega e^{-\omega^2} \int_{-1}^{1} du \\ &\times \int_{\alpha_{min}}^{0} d\alpha\,|\alpha| \left(1 - e^{-\frac{L_\gamma\ z_{max}}{L_N |\alpha|}}\right) , \end{aligned} \tag{B.17}$$

$$\begin{aligned} &= \frac{n_r}{\pi^{3/2}} \sin\theta_c f_0 \Delta_0 \int_0^{\pi/2} d\phi' \left[\int_{\omega_0}^{\infty} d\omega e^{-\omega^2} \int_{-1}^{1} du \right. \\ &+ \left. \int_{-\omega_0}^{\omega_0} d\omega e^{-\omega^2} \int_{-\frac{\omega}{\omega_0}}^{1} du\right] \int_{\alpha_{min}}^{0} d\alpha\,|\alpha| \left(1 - e^{-\frac{L_\gamma\ z_{max}}{L_N |\alpha|}}\right) , \end{aligned} \tag{B.18}$$

where

$$\alpha_{min} = -f_0 \Delta_0 (u + \omega x \cos\phi') < 0 . \tag{B.19}$$

The limits on the u and w integrals in eq. B.18 enforce the requirement that $\alpha_{min} < 0$ for downward incident particles ($\alpha < 0$).

The probabilities of two limits are determined according to the value of L_γ/L_N. In the "neutrino limit", where L_γ/L_ν is very small, the parenthesis in eq. B.18 is

$$\left(1 - e^{-\frac{L_\gamma\ z_{max}}{L_N|\alpha|}}\right) \simeq \frac{L_\gamma\ z_{max}}{L_N\,|\alpha|}\ . \tag{B.20}$$

Then, Eq. B.18 becomes

$$\begin{aligned} P_\nu(E) &= \frac{n_r}{\pi^{3/2}}\frac{L_\gamma}{L_\nu}\sin^2\theta_c f_0^3\Delta_0\int_0^{\pi/2}d\phi'\left[\int_{\omega_0}^{\infty}d\omega e^{-\omega^2}\int_{-1}^{1}du\right. \\ &+ \left.\int_{-\omega_0}^{\omega_0}d\omega e^{-\omega^2}\int_{-\frac{\omega}{\omega_0}}^{1}du\right]\int_{\alpha_{min}}^{0}d\alpha(1-u^2)\ , \end{aligned} \tag{B.21}$$

and it gives as a result

$$P_\nu(E) = \frac{n_r^2-1}{8n_r}\frac{L_\gamma}{L_\nu}f_0^3\Delta_0\left(f_0\Delta_0 + \frac{16}{3\pi^{3/2}}\sigma_0\right)\ , \tag{B.22}$$

with $\sin^2\theta_c = (n_r^2-1)/n_r^2$. This is the "ds" and "dr" contributions to Eq. 5.19 in section 5.3.

In the cosmic ray limit, where L_γ/L_{CR} is large, the exponential term in parenthesis in eq. B.18 goes to 0. Thus, $P_N(E)$ becomes

$$\begin{aligned} P_{CR}(E) &= \frac{n_r}{\pi^{3/2}}\sin\theta_c f_0\Delta_0\int_0^{\pi/2}d\phi'\left[\int_{\omega_0}^{\infty}d\omega e^{-\omega^2}\int_{-1}^{1}du\right. \\ &+ \left.\int_{-\omega_0}^{\omega_0}d\omega e^{-\omega^2}\int_{-\frac{\omega}{\omega_0}}^{1}du\right]\int_{\alpha_{min}}^{0}d\alpha\,|\alpha|\ . \end{aligned} \tag{B.23}$$

This integral yields

$$P_{CR}(E) = \frac{\sqrt{n_r^2-1}}{8}f_0\Delta_0\left(\frac{2}{3}f_0^2\Delta_0^2 + \frac{1}{2}\sigma_0\right)\ , \tag{B.24}$$

as shown in Eq. 5.32 in section 5.4. The numerical evaluation of Eq. B.18 is shown in Fig. 5.16 in section 5.5, and used in evaluating the mini-black hole applications.

BIBLIOGRAPHY

[1] For a review, see, e.g., F. Halzen and S. R. Klein, Rev. Sci. Instrum. D **81**, 081101 (2010).

[2] Y. Ashie *et al.* Super-Kamiokande Collaboration, Phys. Rev. D **71**, 112005 (2005).

[3] J. P. Cravens *et al.* Super-Kamiokande Collaboration, Phys. Rev. D **78**, 032002 (2008).

[4] J. Boger *et al.* SNO Collaboration, Nucl. Instrum. Methods Phys. Res. A **449**, 172 (2000).

[5] C. Amsler *et al.* [Particle Data Group], Phys. Lett. B **667**, 1 (2008).

[6] C. Wiebusch, for the IceCube Collaboration, in the Proceedings of teh 31st ICRC, Lodz 2009, arXiv:0907.2263 [astro-ph.IM].

[7] M. De. Serio, for the OPERA Collaboration, in *the proceedings of the DPF-2009 Conference*, July. 27 - 31, 2009, Detroit, MI [arXiv:0910.0337].

[8] IceCube Collaboration, arXiv:1010.3980.

[9] A. Karle, for the IceCube Collaboration, in the Proceedings of the 31st ICRC, Lodz 2009, arXiv:1003.5715.

[10] A. Etchegoyen *et al.*, for the Pierre Auger Collaboration , arXiv:1004.2537.

[11] K. G. Lehtinen, P. W. Gorham, A. R. Jacobson, and R. A. Russel-Dupre, Phys. Rev. D **69**, 013008 (2004).

[12] I. Kravchenko *et al.*, Phys. Rev. D **73**, 082002 (2006).

[13] P. W. Gorham *et al.*, Phys. Rev. D **82**, 022004 (2010).

[14] P. W. Gorham *et al.*, Phys. Rev. Lett **93**, 041101 (2004).

[15] C. W. James *et al.*, Phys. Rev. D **81**, 042003 (2010).

[16] O. Scholten *et al.*, Phys. Rev. Lett **103**, 191301 (2009).

[17] T. R. Jaeger, R. L. Mutel, and K. G. Gayley arXiv:0910.5949.

[18] J. P. Ralston, D. W. McKay, and G. M. Frichter, in *Conf. Proc. of Seventh International Symposium on Neutrino Telescopes*, Feb. 27 - Mar, 1996, Venice, Italy [arXiv:hep-ph/0110235].

[19] R. Gandhi, C. Quigg, M. H. Reno, and I. Sarcevic, Astropart. Phys. **5**, 81 (1996); R. Gandhi, C. Quigg, M. H. Reno and I. Sarcevic, Phys. Rev. D **58**, 093009 (1998).

[20] M. Gluck, S. Kretzer, and E. Reya, Astropart. Phys. **11**, 327 (1999).

[21] A. Cooper-Sarkar and S. Sarkar, JHEP **0801**, 075 (2008).

[22] A. Cooper-Sarkar and S. Sarkar, Phys. Rev. D **77**, 053007 (2008).

[23] Yu Seon Jeong and Mary Hall Reno, Phys. Rev. D **81**, 114012 (2010).

[24] Yu Seon Jeong and Mary Hall Reno, Phys. Rev. D **82**, 033010 (2010).

[25] P. M. Nadolsky *et al.*, Phys. Rev. D **78**, 013004 (2008).

[26] M. Gluck, P. Jimenez-Delgado and E. Reya, Eur. Phys. J. C **53**, 355 (2008).

[27] T. Gottschalk, Phys. Rev. D **23**, 56 (1981).

[28] J. J. van der Bij and G. J. van Oldenborgh, Z. Phys. C **51**, 477 (1991).

[29] J. Smith and W. L. van Neerven, Nucl. Phys. B **374**, 36 (1992); E. Laenen, S. Riemersma, J. Smith and W. L. van Neerven, Nucl. Phys. B **392**, 162 (1993).

[30] G. Kramer and B. Lampe, Z. Phys. C **54**, 139 (1992) [Eur. Phys. J. C **17**, 371 (2000)].

[31] M. Gluck, E. Reya and M. Stratmann, Nucl. Phys. B **422**, 37 (1994).

[32] S. Kretzer and I. Schienbein, Phys. Rev. D **58**, 094035 (1998).

[33] F.I. Olness and W. Tung, Nucl. Phys. B308, 934 (1988); M. A. Aivazis, F.I. Olness and W.K. Tung, Phys. Rev. Lett. 65, 2339 (1990).

[34] M. A. G. Aivazis, F. I. Olness and W. K. Tung, Phys. Rev. D **50**, 3085 (1994).

[35] M. A. G. Aivazis, J. C. Collins, F. I. Olness and W. K. Tung, Phys. Rev. D **50**, 3102 (1994).

[36] J. Amundson, C. Schmidt, W. K. Tung and X. Wang, JHEP **0010**, 031 (2000); W. K. Tung, S. Kretzer and C. Schmidt, J. Phys. G **28**, 983 (2002). For a review, see, e.g., F. Olness and I. Schienbein, Nucl. Phys. Proc. Suppl. **191**, 44 (2009).

[37] R. S. Thorne and R. G. Roberts, Phys. Lett. **B 421**, 303 (1998); R. S. Thorne and R. G. Roberts, Phys. Rev. D **57**, 6871 (1998) R. S. Thorne and R. G. Roberts, Eur. Phys. J. C **19**, 339 (2001); R. S. Thorne, Phys. Rev. D **73**, 054019 (2006).

[38] M. Cacciari, M. Greco and P. Nason, JHEP **9805**, 007 (1998); S. Forte, E. Laenen, P. Nason and J. Roho, eprint arXiv:1001.2312.

[39] P. Nadolsky and W.-K. Tung, Phys. Rev. D **79**, 113014 (2009).

[40] J. R. Andersen *et al.* [SM and NLO Multileg Working Group], arXiv:1003.1241 [hep-ph].

[41] G. 'tHooft, Nucl. Phys. B **61**, 455 (1973); S. Weinberg, Phys. Rev. D **8**, 3497 (1973).

[42] C. H. Albright and C. Jarlskog, Nucl. Phys. B **84**, 467 (1975).

[43] S. Kretzer and M. H. Reno, Phys. Rev. D **66**, 113007 (2002).

[44] L. Pasquali and M. H. Reno, Phys. Rev. D **59**, 093003 (1999).

[45] J. I. Illana, P. Lipari, M. Masip, and D. Meloni, [arXiv:1010.5084].

[46] A. Menegolli, on behalf of the ICARUS Collaboration, J. Phys. Conf. Ser. **203**, 012107 (2010).

[47] M. Dracos, J. Phys. Conf. Ser. **203**, 012013 (2010).

[48] K. G. Gayley, R. L. Mutel, and T. R. Jaeger Astropart. Phys. **706**, 1556 (2009).

[49] A. Kusenko, and T. J. Weiler, Phys. Rev. Lett. **88**, 161101 (2002).

[50] S. Hussain, D. Marfatia, D. W. McKay, and D. Seckel, Phys. Rev. Lett. **97**, 161101 (2006).

[51] S. Palomares-Ruiz, A. Irimia, and T. J. Weiler, Phys. Rev. D **73**, 083003 (2006).

[52] K. Kotera, D. Allard, and A. V. Olinto, JCAP **1010**, 013 (2010).

[53] J. Abraham *et al.* The Pierre Auger Collaboration, Phys. Lett. B **685**, 239 (2010).

[54] P. Lipari, M. Lusignoli, and F. Sartogo, Phys. Rev. Lett. **74**, 4383 (1995).

[55] J. Collins, Phys. Rev. D **58**, 094002 (1998).

[56] G. Altarelli and G. Parisi, Nucl. Phys. B **126** 298 (1977); V. N. Gribov, L. N. Lipatov, Sov. J. Nucl. Phys. **15** 438 (1972); Yu. L. Dokshitzer, Sov. Phys. JETP **46** 641 (1977).

[57] W. K. Tung, H. L. Lai *et al.*, JHEP 0702:053 (2007).

[58] M. Kramer, F. Olness, and D. E. Soper, Phys. Rev. D **62**, 096007 (2000).

[59] See also, S. Kretzer and M. H. Reno, Nucl. Phys. Proc. Suppl. **139**, 134 (2005).

[60] O. Nachtmann, Nucl. Phys. B **78**, 455 (1974).

[61] H. Georgi and H. D. Politzer, Phys. Rev. D **14**, 1829 (1976); A. De Rujula, H. Georgi and H. D. Politzer, Annals Phys. **103**, 315 (1977)

[62] S. Kretzer and M. H. Reno, Phys. Rev. D **69**, 034002 (2004); I. Schienbein *et al.*, J. Phys. G **35**, 053101 (2008).

[63] A. Capella, A. Kaidalov, C. Merino and J. Tran Thanh Van, Phys. Lett. B **337**, 358 (1994) and *Proceedings of 29th Rencontres de Moriond: QCD and high energy hadronic interactions, Meribel les Allues, France, 19-26 March 1994*, pp. 271-282.

[64] Mary Hall Reno, PRD **74**, 033001 (2006).

[65] L. W. Whitlow, Stephen Rock, A. Bodek, E. M. Riordan, and S. Dasu Phys. Lett. B **250**, 193 (1990).

[66] R. Basu, D. Choudhury, and S. Majhi, JHEP **0210**, 012 (2002).

[67] V. Berezinsky, Nucl. Phys. B Proc. Suppl. **00**, 1-8 (2011).

[68] B. Baret and V. Van Elewyck Rep. Prog. Phys. **74**, 046902 (2011).

[69] R. U. Abbasi, *et al.*, Phys. Rev. Lett. **100**, 101101 (2008).

[70] K. Greisen, Phys. Rev. Lett. **16**, 748-750 (1966).

[71] G. T. Zatsepin, V. A. Kuz'min JETP Letters **4**, 78-80 (1966).

[72] R. Engel, D. Seckel, and T. Stanev, Phys. Rev. D **64**, 093010 (2001).

[73] A. M. Taylor, *Proceedings of Cosmology, Galaxy Formation and Astroparticle Physics on the Pathway to the SKA, oxford, United Kingdom, 10-12 April 2006.*

[74] L. A. Anchordoqui, H. Goldberg, D. Hooper, S. Sarkar, and A. Taylor, Phys. Rev. D **76**, 093010 (2007).

[75] R. D. Dagkesamanskii and I. M. Zheleznykh, JETP Lett. **50**, 233 (1989).

[76] G. A. Askaryan, JETP **14**, 441 (1962).

[77] S. ter Veen, *et al.*, Phys. Rev. D **82**, 103014 (2010).

[78] C. W. James and R. J. Protheroe, Astropart. Phys. **30**, 318 (2009).

[79] N. Arkani-Hamed, S. Dimopoulos, and G. R. Dvali, Phys. Lett. B **429**, 263-272 (1998).

[80] I. Antoniadis, N. Arkani-Hamed, S. Dimopoulos, and G. R. Dvali, Phys. Lett. B **436**, 257-263 (1998).

[81] N. Arkani-Hamed, S. Dimopoulos, and G. R. Dvali, Phys. Rev. D **59**, 086004 (1999).

[82] L. Randall, and R. Sundrum, Phys. Rev. Lett. **83**, 3370-3373 (1999).

[83] L. Randall, and R. Sundrum, Phys. Rev. Lett. **83**, 4690-4693 (1999).

[84] The ATLAS Collaboration ATL-PHYS-PUB-2009-074.

[85] S. I. Dutta, M. H. Reno and I. Sarcevic, Phys. Rev. D **66**, 033002 (2002).

[86] J. Alvarez-Muniz, J. L. Feng, F. Halzen, T. Han and D. Hooper, Phys. Rev. D **65**, 124015 (2002).

[87] A. Connolly, R. S. Thorne, and D. Waters, arXiv:1102.0691 [hep-ph].

[88] L. A. Anchordoqui, J. L. Feng, H. Goldberg, and A. D. Shapere, arXiv:1102.0691 [hep-ph]. Phys. Rev. D **68**, 104025 (2003).

[89] M. K. Shepard, R. A. Brackett, and R. E. Arvidson, J. Geophys. Res. D **100**, 11709 (1995).

[90] K. Kodama *et. al*, (DONuT Collaboration), Phys. Rev. D **78**, 052002 (2008).